EFFECTS OF STRAIN PATH CHANGES ON DAMAGE EVOLUTION AND SHEET METAL FORMABILITY

EFFECTS OF STRAIN PATH CHANGES ON DAMAGE EVOLUTION AND SHEET METAL FORMABILITY

BY

TASNEEM NEHRIN ZAMAN, B. Sc.

A Thesis

Submitted to the School of Graduate Studies

in Partial Fulfillment of the Requirements

For the Degree of

Master of Applied Science

McMaster University

2008

MASTER OF APPLIED SCIENCE — McMASTER UNIVERSITY

MECHANICAL ENGINEERING — HAMILTON, ONTARIO

TITLE:	EFFECTS OF STRAIN PATH CHANGES ON DAMAGE EVOLUTION AND SHEET METAL FORMABILITY
AUTHOR:	TASNEEM NEHRIN ZAMAN (B.Sc.- BANGLADESH UNIVERSITY OF ENGINEERING AND TECHNOLOGY)
SUPERVISOR:	DR. PEIDONG WU
NUMBER OF PAGES:	XIV, 97

ABSTRACT

The concept of the Forming Limit Diagram (FLD) has proved to be useful for representing conditions for the onset of sheet necking, and is now a standard tool for characterizing materials in terms of their overall forming behavior. In this study, the M-K approach, in conjunction with Gurson model, is used to calculate FLDs. The influences of mechanical properties, including strain hardening, strain rate sensitivity, as well as the void nucleation, growth and coalescence, on the FLDs are examined.

Most sheet metals undergo multiple deformation modes (strain paths) when being formed into complex manufacturing parts. When the strain path is changed in the deformation processing of metal, it's work-hardening and flow strength differs from the monotonic deformation characteristics. As a consequence, sheet metal formability is very sensitive to strain path changes. In this study, the hardening behavior and damage evolution under non-proportional loading paths are investigated. The effect of strain path change on FLDs is studied in detail.

FLDs are conventionally constructed in strain space and are very sensitive to strain path changes. Alternatively, many researchers represented formability based on the state of stress rather than the state of strain. They constructed a Forming Limit Stress Diagram (FLSD) by plotting the calculated principal stresses at necking. It was concluded that FLSDs were almost path-independent. In this work, the FLSD has been constructed under non-proportional loading conditions to assess its path dependency when damage effect is included.

ACKNOWLEDGEMENTS

I would like to express my sincere appreciation to my supervisor Dr Peidong Wu for giving me this opportunity and providing me with the necessary guidance and support throughout my project. Without his help and directions this thesis would not be possible.

I wish to express my special thanks to Huamiao Wang for helping me in all the stages of my research. Also thanks go to Nicholas Trutwin for proof reading my thesis.

Finally, I would like to take the opportunity to thank my parents and husband for their unwavering support throughout my study period.

Funding for the work carried out at McMaster University was provided by Novelis Inc., National Science and Engineering Research Council of Canada (NSERC) and McMaster University

TABLE OF CONTENTS

LIST OF FIGURES

LIST OF TABLES

NOMENCLATURE

ϕ	Yield function
σ	Macroscopic Cauchy stress
σ_H, σ_m,	Mean stress
σ_e	Effective stress
σ'	Deviatric Cauchy stress
σ_0	Reference stress
$\overline{\sigma}$	Flow stress of matrix material
$\overset{\nabla}{\sigma}$	Jaumann derivative of Cauchy stress
$\dot{\overline{\sigma}}$	Visco-plastic stress rate
f	Void volume fraction
$\dot{f}$	Increase of void volume fraction
q_1, q_2, q_3	Parametrs of Gurson-Tvergaard [1982] yield function
ε	True normal strain
$\dot{\overline{\varepsilon}}$	Visco-plastic strain rate
$\overline{\varepsilon}$	Equivalent visco-plastic strain
$\Delta\overline{\varepsilon}$	Increment of effective visco-plastic strain
ε_0	Reference strain
$\dot{\varepsilon}_0$	Reference strain rate
N	Strain hardening exponent
m	Strain rate hardening exponent
E	Young's modulus
D	Rate of deformation
L	Elastic compliance
ν	Poisson's ratio
W	Rate of spin
$\dot{E}$	Proportionality factor
p	Viscoplastic strain rate direction
f_n	Void volume fraction of nucleating particles
ε_n	Strain at which void nucleation reaches its maximum value
s_n	Standard deviation
ε^p	Effective plastic strain
σ_n	Stress at which void nucleation reaches its maximum value
f_c	Critical value of void volume fraction
f^*	Void volume fraction where void coalescence initiates
f_u^*	Ultimate value of void volume fraction
f_f	Void volume fraction of fracture
θ	Rate forwarding parameter
Ψ_0 and Ψ	Initial and current angle of inhomogeneous band with respect to

	minor axis
t	Time
ρ	Strain rate ratio
α	Stress rate ratio
h^B and h	Thickness of the groove and the parent sheet
n,t	Co-ordinate system with n normal and t parallel to inhomogeneous band
$1,2,3$	Principal directions in homogenous region
$()^B$	Inhomogeneous region (inside the band)
δ_{ij}	Kronecker delta-a second order tensor
I	Second order identity tensor

CHAPTER 1

INTRODUCTION

Ductile materials typically attain large plastic deformations during industrial forming operations. Often engineering materials contain second phase particles or inclusions which may debond from the surrounding material matrix due to the influence of plastic deformations. As a result, voids and micro-cracks are initiated. When further straining is applied, growth and coalescence of the voids occurs. This may lead to considerable degradation of the overall material strength, and thus the micro-structural damage evolution and its influence on the material behavior are very important in predicting material formability and the causes of failures in production.

Over the years fracture of ductile materials has been the subject of much research. Several damage models have been developed to describe damage evolution and fracture. Among these, the Gurson model (1977) has been the most popular one because of its simplicity and reasonable agreement with experimental results. Gurson studied ductile porous materials (aggregate of voids and ductile matrix) and assumed matrix material as rigid-plastic. The original Gurson model considered only the growth of pre-existed voids. Significant improvements on Gurson model have been made. Among them, a void nucleation model was developed by Chu and Needleman (1980), and void coalescence was described by Tvergaard (1982). Most of these works were reviewed by Tvergaard (1990).

In sheet metal forming operations the failure mode usually involves formation of localized necking [Keeler, 1965; Goodwin, 1968; Azrin and Backofen, 1970]. Localized necking can be described as a locally thinned region within which strain is concentrated. The maximum strains which can be attained in sheet materials prior to the onset of localized necking are

generally referred to as forming limit strains. A plot of major and minor limit strains, denoted by ε_{11}^{*} and ε_{22}^{*} in the principal strain space of a two dimensional Cartesian coordinate system, constitutes a Forming Limit Diagram (FLD) which was first developed by Keeler and Backofen (1964). They used a sheet metal etched with circles and then deformed it until failure. After deformation the circles became ellipses and by measuring the major and minor diameters, the limit strains in the principal directions were determined. The FLD is now a standard tool for characterizing materials in terms of their formability.

Experimental determination of FLDs following the methods proposed by Nakazima *et al* (1968) and Marciniak (1967) are frequently used [see e.g. Janssens *et.al,* 2001] and are briefly described in chapter 2. To diagnose the cause of material failure, surface strain and geometry analysis is necessary. For the measurement of strain, circular grid analysis (CGA), and square grid analysis are widely used. CGA is the most common method where a circular grid pattern is electrochemically etched onto the blank sheet. The deformed grid is compared to the original grid to determine the strains. Earlier the measurement of deformed grid patterns was done by using conventional Mylar tape. Recently, optical tensor and image processing technologies are used to obtain this data (Chan *et.al,* 2007).

Conventionally, FLD are constructed based on the assumption of a linear deformation path. However, Most sheet metals undergo multiple deformation modes (strain paths) when being formed into complex manufacturing parts. Many researchers [see e.g. Wagoner and Laukonis, 1983; Zandrahimi *et al.*, 1989; Graf and Hosford, 1993] have found that FLDs are very sensitive to strain path changes. Therefore, a linear strain path can no longer be assumed in any theoretical model [Barata Da Rocha *et al,* 1984]. Tracking the multiple modes of deformation can only be done with a detailed knowledge of the deformation history and analysis

of each case. This makes the experimental method expensive and necessitates the development of analytical models which can predict formability efficiently and cheaply.

Most theoretical and numerical investigations of FLDs are based on the M-K approach developed by Marciniak and Kuczynski (1967). In the M-K approach a thickness variation in the form of a groove is introduced as a pre-existing defect in the sheet material. They showed that this slight intrinsic inhomogeneity in load bearing capacity throughout a deforming sheet can lead to unstable growth of strain in the region of the imperfection, and subsequently cause localized necking and failure. In this study, numerical simulations of FLDs are performed based on Gurson model together with the M-K approach. The Gurson damage model accounts for the void growth, nucleation, and coalescence, while the M-K approach will predict the onset of necking. As stated earlier, necking will be initiated from a narrow band and deformation will be homogenous inside and outside the band. Due to non-proportional loading, the flow strength and hardening behavior, as well as the limit strain of the material, differs from the monotonic loading condition. The transient changes of strain path can alter the initial flow stress and hardening rate. Thus, the main objective of this work is to predict more accurately the forming limits under nonlinear strain paths by incorporating the Gurson model, and to show the evolution of damage for each case of path change. Also, the effect of material properties is investigated in order to determine their influence on the formability of the material.

As mentioned previously, FLDs are very sensitive to the strain path change. Therefore, there is no single curve in strain space that represents the forming limit, and this limits the use of conventional FLDs for assessing forming severity because the straining path of material elements in a real sheet metal forming process is usually not known with any certainty. Therefore, finding a single path-independent curve to characterize forming limits is of considerable practical

interest. Knowing the drawback of conventional FLDs, many researchers have represented formability based on the state of stress rather than the state of strain. They constructed a Forming Limit Stress Diagram (FLSD) by plotting the calculated principal stresses at necking. It was concluded that FLSDs were less path dependence than a strain based FLD [Arrieux R., 1995; Zhao *et.al,* 1996; Stoughton, 2000; Wu *et.al,* 2005].

In Chapter 2 a brief description of metal formability is given and the concept of the FLD is introduced. Various experimental and analytical methods for constructing FLDs are reviewed. Furthermore, the importance of strain path change in forming operations is discussed. The Forming Limit Stress Diagram is also described.

In Chapter 3, Gurson constitutive model is formulated and the M-K approach is described. A detailed description of the development of a numerical code for predicting FLDs, based on the M-K approach and Gurson damage model, is also given in this chapter.

Sheet metal forming processes are a combination of different forming modes which have different strain paths. When the strain path is changed, the work-hardening and flow strength differ from the monotonic deformation characteristics. Chapter 4 studies plastic behavior of material under these non-proportional loading conditions.

Chapter 5 starts with examining the effects of material properties and initial imperfections on FLDs. The effect of strain path changes is then assessed. In this study, the non-proportional loading histories are developed using combinations of two linear strain paths. The first strain path, the pre-strain operation, is common to all loading histories. Subsequent linear deformation paths are imposed by varying the strain-rate ratio for the development of an FLD applicable to that given pre-strain path and amount. Finally, Chapter 5 gives a brief account of the Forming Limit Stress Diagram (FLSD) and its path dependency.

Chapter 6 lists the conclusions of the current research and discusses future work directions for the improvement and development of analytical models for assessing sheet metal formability.

CHAPTER 2

LITERATURE REVIEW

2.1 Introduction

The studies conducted on the analysis of sheet metal formability are too broad to be reviewed in its entirety, so the main objective is to cover the analysis from the perspective of damage evolution using Gurson model. For ease of understanding the scope of this work, a literature review has been conducted on the following sections: general formability and damage evolution, and the perception, experimental determination, theoretical modeling and application of FLDs. For theoretically determining limit strains, this review limits to those based on the M-K approach. Also included is a discussion of the effect of changing the strain path on the FLD. Furthermore, the determination of forming limits in stress space is briefly described.

2.2 Formability of metal

By definition, forming is the shaping of metals in the solid state and the degree to which a material can be formed depends largely on its inherent ductility or its ability to plasticity deform. Metal forming is divided into two primary commercial fields: processing, and fabricating. In the first case simple products such as plates and sheets are made from bulk materials. In the second type more complicated shapes are developed which may start to resemble parts of products [Sachs, G., 1954].

For a successful procedure the flow stress, or resistance to deformation, of the material plays a vital role and the equipment and tools used for producing parts need to be strong but it is still not fully understood by researchers which material properties will determine the limit of

forming. The common properties defining a material such as its yield strength, hardness, modulus of elasticity etc. are not sufficient to predict the performance of a material behavior under different forming processes [Avitzur, 1980].

From years of extensive experimental research it has been concluded that material failure during forming operations can occur due to a variety of reasons including: fracture, buckling/wrinkling, and flow instability/necking [Marciniak *et al.,* 1992]. Failure by fracture occurs mainly as a result of extensive tensile stress. When stress is applied to increase the length of a metal fiber beyond its limit, the metal fibers will completely separate resulting in cracking. Buckling tends to occur in slender objects under compression and can occur when making heads of bolts and rivets. Between necking or flow instability the first one is diffuse necking and it is named so because its extent is much greater than the sample thickness. Diffuse necking starts when the tensile load reaches its maximum. It may terminate in fracture but is often followed by a second instability process called localized necking of material. Once localized necking started the width of the sample contracts little, but the thickness along the necking band shrinks rapidly. Fracture occurs soon after .Localized necking occurs in sheet metal forming operations such as stretch drawing, hydro-forming, bulging, tube-bulging etc. [Marciniak, 1974]. This phenomenon of necking determines the limit of forming for different types of metal. In the next section the concept of damage is introduced followed by different damage models.

2.3 Damage Evolution on Formability

A variety of micro-structural changes are developed during deformation processes which eventually cause degradation in material properties, known as material damage. Damage is defined as micro-void formation and growth [Coffin and Rogers, 1967]. Voids can nucleate at a

comparatively small strain but eventually grow due to ductile deformation processes. Void coalescence also occurs which elongates the amount of void formation. This whole process is called ductile damage and because of its significant effect on the behavior of the material, it is important to introduce it into any model of a sheet metal forming process.

Experimental studies have shown that micro-voids play a vital role in the ductile fracture of materials [Puttick, 1960]. Goods and Brown (1979) reported that the central role played by inclusion cracking or/and deboning in void nucleating in structural metals which then grow by plastic deformation of the surrounding matrix material. The weakening of material due to the formation of void growth and nucleation causes the localization of necking which eventually leads to ductile failure. The most widely known damage model is that developed by Gurson (1977) based on averaging techniques. The characteristic volume element considered by Gurson is an aggregate of voids and rigid plastic matrix material, and approximate upper-bound solutions on the micro-level have been used to derive a macroscopic yield condition for the material. The yield criterion of Gurson depends not only on the effective stress, σ_e (as in classical plasticity), but also the hydrostatic stress, σ_H, and void volume fraction, f. Based on Gurson model, Needleman and Triandafyllidis (1978) investigated localized necking for biaxially stretched sheet. They found that this model predicted material forming limits qualitatively agreed with experimental results.

The original Gurson model considered only the growth of pre-existed voids. Significant improvements on Gurson model have been made. Among them, a void nucleation model was developed by Chu and Needleman (1980), and the effect of void coalescence was incorporated into the Gurson model by Tvergaard (1982). Most of these progresses were reviewed by Tvergaard (1990). In the present study, the modified Gurson model called Gurson-Tvergaard-

Needleman (GTN) model, is used to determine sheet metal failure. The parameters involved in the GTN model are usually determined by empirical methods [see e.g. Brocks and Bernaur, 1995]. Recently, Springmann and Kuna [2005] identified the parameters by a non-linear optimization method using finite element analysis. They concluded that the quantity of information from a force–displacement curve is relatively small contrary to the number of unknown material parameters of the GTN model. In another recent study [Benseddiq and Imad, 2008], the GTN model was used to investigate ductile tearing to assess the sensitivity of the model parameters.

In application of the GTN model to predict sheet metal formability, localized necking process is accelerated by the void growth, nucleation, and coalescence. In some cases, a sheet metal is fractured due to damage before localized necking occurs [see e.g. Needleman and Triandafyllidis, 1978]. In the next section the concept of a Forming Limit Diagram and how to use it assess sheet metal formability will be discussed.

2.4 Perception of Forming Limit Diagram

The forming limit diagram (FLD) is a very useful tool for characterizing the formability of sheet metal. The FLD was first introduced by Keeler and Beckhofen (1964), and later Goodwin (1968) developed an empirical relation on the rudimentary FLD. The main purpose of FLD is to distinguish the safe regions for material processing by defining the regions where failure occurs. In Figure 2.1 a typical forming limit diagram is shown. From the figure it can be observed that an FLD of a sheet material is developed by plotting the major strain the minor strain in a 2D strain space. The safe region for material forming is below the FLD curve, above it, the material tends to lose its strength and fail. A series of linear straining paths are proposed ranging from uniaxial

compression to equibiaxial stretching as depicted in Figure 2.1 [Marciniak *et al.*, 1992]. These linear strain paths are described by the ratio of minor strain to major strain.

$$\rho = \frac{\varepsilon_2}{\varepsilon_1} \tag{2.1}$$

where ε_1 and ε_2 are the major and minor strain, respectively The possible strain paths in sheet forming operations lie in the range $-2 \leq \rho \leq 1$ When $\rho=1$ the deformation mode achieved is equibiaxial stretching as when a sheet is stretched over a hemispherical punch. In this condition the circular grid expands as a circle because strains are equal in all directions. In the in-plane

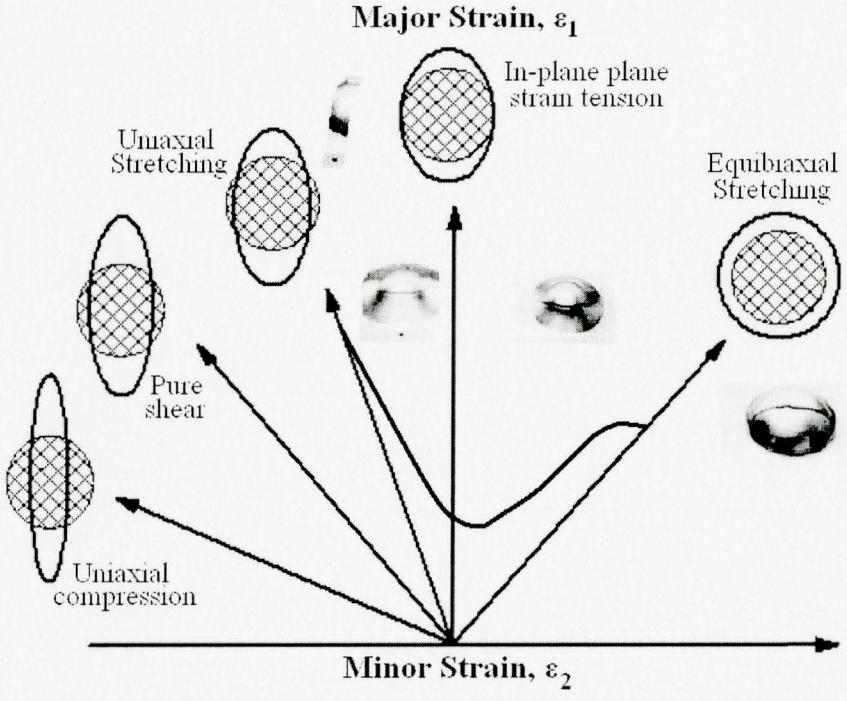

Figure 2.1 A typical FLD showing various linear strain paths from uniaxial compression to equi-biaxial tension [Marciniak *et al.*, 1992]

strain condition, the strain ratio is equal to zero ($\rho=0$) and the sheet as well as the grid circle extends in one direction while the other direction is unchanged. As a result the grid circle

becomes an ellipse. When the minor stress in a sheet is zero and it stretches only in one direction while other direction contracts, the condition attained is called uniaxial stretching where ρ=*-0.5*.

A strain ratio less than -1 does not reduce the sheet thickness so beyond this point the sheet metal is assumed to be thickened. When ρ=*-1*, a drawing or pure shear condition is observed. Here, stresses and strains are equal and opposite and the sheet deforms without changing its shape. Finally, at the extreme end of Figure 2.1 when ρ=*-2* the minor stress is in opposite direction and the sheet thickens as well as often wrinkling occurs. Thus an FLD curve can efficiently describe sheet forming processes and can also indicate the safe region for forming operations which subsequently reduces the chance of failure. In the current study strain ratios from uniaxial stretching to equi-biaxial stretching, where thinning of sheet metal occurs, have been considered.

2.5 Experimental Determination of a Forming Limit Diagram

A forming limit diagram for various forming operations and materials can be obtained either experimentally or numerically. A brief description of the experimental determination of an FLD is necessary to understand the process. The first step towards obtaining experimental data for an FLD is done by electrochemically etching or photographically printing a grid pattern on the undeformed sheet metal [Keeler, 1969; Schedin and Melander, 1986; Lee *et al.,* 1994; Lee, 1996; Wang *et al.,* 2000]. After deformation the deformed grids are measured and compared to the original grid pattern to determine the principal strain levels. The most established experimental methods used for determining FLDs are the Nakazima test [Nakazima *et al.*, 1968] and Marciniak's cup test [Marciniak and Kuczynski, 1967].

For Nakazıma's method [Nakazima *et al.,* 1968] a hemispherical punch and a special lubrication system were developed. In thıs test, which is also known as an out-of-plane forming test, a 4-inch diameter hemispherical punch is used to form a dome in metal sheets which are fixed around their circumference as shown in Figure 2.2. In Figure 2.3 samples are produced for strain ratios ranging from uniaxial tension to equibiaxial tension. The sample having smallest wıdth is the uniaxial tension specimen and the thickest one is the equi-biaxıal tension specimen. Between these two conditions all other strain paths are observed.

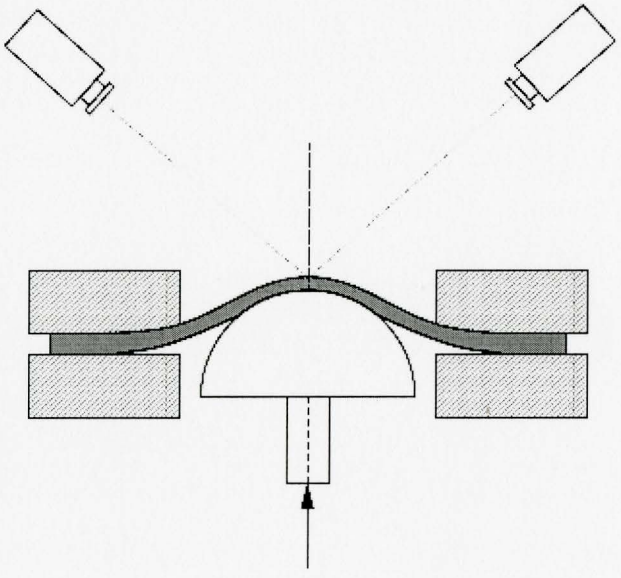

Figure 2.2. Schematic set-up of Nakazima test method [GOM, 2001]

In the Marciniak's test [Marciniak and Kuczynski, 1967], the sheet metal is deformed in ıts plane. A drawing die, blank holder, and flat punch are needed. During the forming process, the flat and even forehead of the punch causes an in-plane deformation condition in the sheet metal specimen area. Figure 2.4 shows the in-plane test setup used by Marciniak and Kuczynski

[1967] Lewison and Lee [1999] have done similar in-plane test (See Figure 2.5) and compared to out-of plane test.

For constructing the Forming Limit Diagram, the circular grid system has been widely used [Keeler, 1969; Lee *et al.,* 1994, Lee, 1996; Wang *et al.,* 2000] It can measure directly the principal strains at any location in the sheet. Conventionally, the grids in the deformed sheet metal were measured with the help of transparent (Mylar) tape and a magnifier However, this process is very time consuming and inaccurate. Wick *et al.* [1984] and Harvey [1984] developed

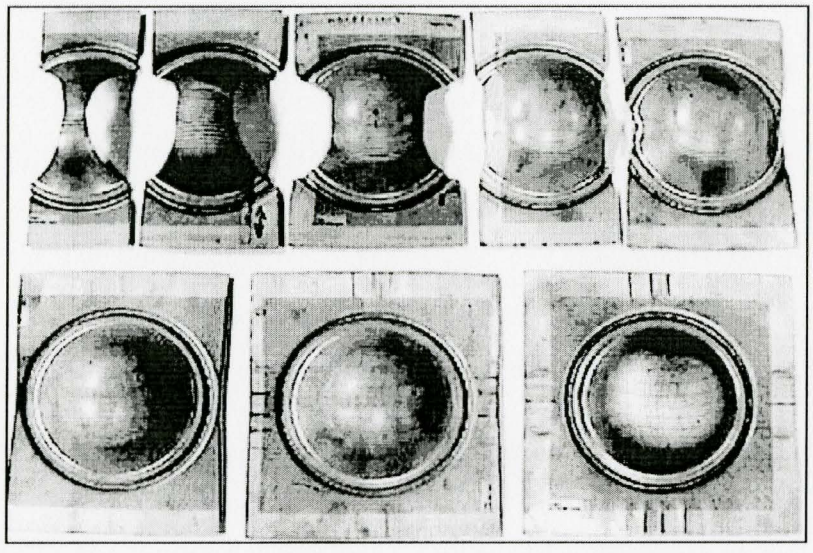

Figure 2.3 Sample geometries from a Nakazima or out-of-plane forming test. Strain paths are described from uniaxial tension (top left) to equibiaxial tension (bottom right) [Lewison and Lee; 1999]

an optical strain measurement system to acquire the principal strains of deformed grids automatically with an image processing technology Some other researchers [see e.g. Lee and Hsu, 1994; Wang *et al.* 1997, Hsu, 2002] have also used optical image processing systems for analysis of deformed circular grids (CGA) in their studies. The measuring of grids in Nazakima

test may become

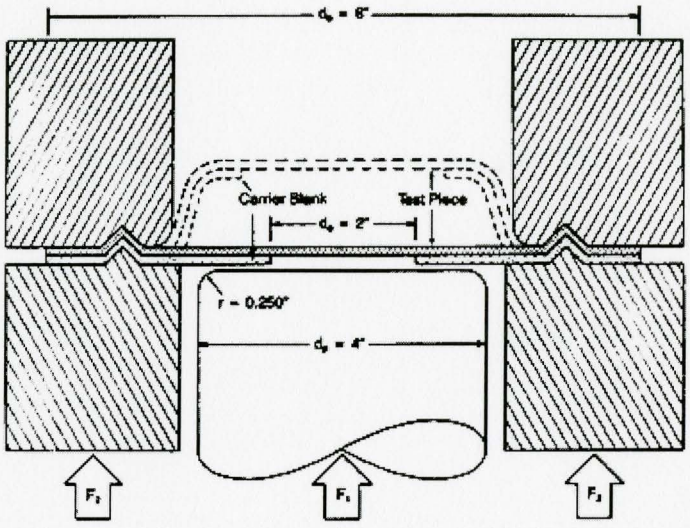

Figure 2.4. Schematic of Marciniak's Cup test. Specimen after an increment of deformation is shown as dotted line [website: *www.a-sp.org/database/viewsec.asp?sec=246*]

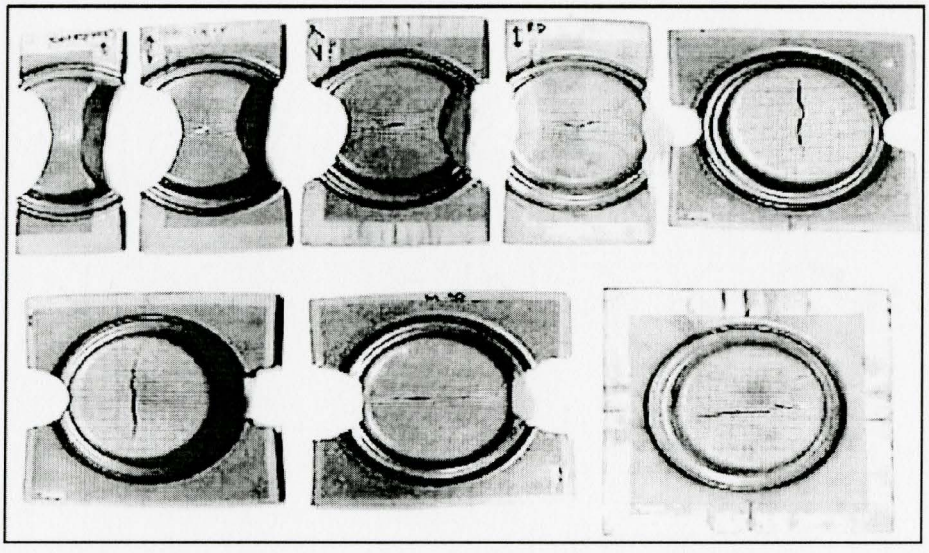

Figure 2.5: Sample geometries from Marciniak's in-plane forming test. Strain paths are described from uniaxial tension (top left) to equibiaxial tension (bottom right). [Lewison and Lee, 1999]

difficult due to interpreting the deformed curved surface because of the strain gradient present in the specimen. Marciniak's test avoids this difficulty [Marciniak and Kuczynski, 1967]. The CGA technique cannot be used for non-proportional deformation due to its non-unique character of the ellipse to ellipse transformation [Sklad, 2004]. Sklad [2004] also concluded that for measurement of non-proportional deformation a grid that consists of at least three non-collinear points or polygon vertices, triangle, quadrilaterals etc. are required. Schedin and Melander [1986] used a square grid for the analysis of principal strains from a deformed industrial sheet metal stamping process. Recently, Chan *et al* [2007] used a high accuracy co-ordinate measuring machine mounted to a laser digitizer for the sheet metal strain and surface analysis. First, the flat sheet metal blank is electrochemically etched with a hollow centre circular grid pattern. As the blank is pressed into the desired shape, the resulting strain deforms the circles into approximately elliptical shapes. The sheet metal is then laser digitized every 0.1mm and the surface coordinates plus reflected light intensity is simultaneously recorded. Parallel computer-based image processing separates the darker ellipse grid points from the lighter background, and orthogonal least-squares data fitting estimates the major and minor surfaces strains. They have concluded that this method has a much lower percentage of uncertainty compared to other existing methods for strain measurement.

Jansseens *et al* [2001] applied a statistical method to evaluate the intrinsic precision of the experimental procedures of Marciniak and Nakazima. They concluded that uncertainty of forming limit in sheet metal is not due to the experimental procedure.

2.6 Theoretical Models for Determining a Forming Limit Diagram

Since the concept of FLD was invented by Keeler and Beckofen [1964] and then Goodwin [1968] it has been a very important tool for determining the safe deformation zone for materials subjected to different forming operations. Although the concept of the FLD is simple, the experimental implementation is not. For this reason many researchers have developed simple analytical and numerical models to predict FLDs. There are two main analytical/numerical approaches in constructing FLDs: the Hill's bifurcation analysis, and the M-K approach.

Hill [1952] was the first researcher who proposed a bifurcation criterion for localized necking in thin sheets. His analysis predicts that localized necking occurs in the direction of zero extension on the surface of the sheet. This implies that one of the principal strains must be negative. Therefore, Hill's method can only predict the left hand side of an FLD. After the bifurcation analysis of Hill, Storen and Rice [1975] proposed that localized necking originates from the vertex developed on the subsequent yield surface. They combined the bifurcation and J_2 flow theory for different proportional loading conditions. Later other researchers like Hill and Hutchinson [1975], and Hutchinson and Neale [1978] also worked on this method.

Most theoretical and numerical FLD analyses have been based on the so-called M-K approach, developed by Marciniak and Kuczynski (1967). The basic assumption of this approach is the existence of a material imperfection, in the form of a groove on the surface of the sheet. They showed that a slight intrinsic inhomogeneity in load bearing capacity throughout a deforming sheet can lead to unstable growth of strain in the region of the imperfection, and subsequently cause localized necking and failure. Within the M-K framework, the influence of various constitutive features on FLDs has been explored using phenomenological plasticity models (see e.g. Neale and Chater 1980). Especially, the effect of material anisotropy on FLDs

has been extensively studied using various analytical anisotropic functions [see e.g. Kuroda and Tvergaard, 2000; Wu *et al.*, 2003] and crystal plasticity (see e.g. Zhou and Neale, 1995; Wu *et al.*, 1997).

Effects of damage evolution have also been incorporated into the M-K approach to calculate FLDs. Based on various damage models, Yamamoto [1978], Needleman and Triantafyllidis [1978], Jalinier [1983], Saje *et al.* [1982], Tvergaard [1982], Kim and Kim [1983], Rao and Chaturvedi [1986], Huang *et al.* [2000] and Brunet and Morestin [2001] studied the role of void initiation, growth and coalescence on localized necking in sheet metals. Varma *et al.* [2006] studied localized necking in aluminum alloy tubes subjected to hydro-forming by a combination of the M-K approach and an anisotropic version of the Gurson model.

2.7 Effect of Strain Path Change on the Forming Limit Diagram

The limiting strains reported in FLDs were initially based on the assumption of a proportional strain path (monotonic loading) prior to the occurrence of plastic flow localization. However, a number of investigations [see e.g. Gronostajski, 1984] showed that more complex deformations were governed by multiple types of straining. During an actual forming operation, a material element may undergo considerably large changes in strain path, and these changes may significantly alter the forming limits [Laukonis and Ghosh, 1978; Graf and Hosford, 1993, 1994]. For example, the stamping of sheet metal components often involves multiple operations. During stamping of sheet metal, certain material locations in a part may experience a change from one type of deformation to another. Such strain path changes may be gradual, as in a single operation, or abrupt, as in multiple operations. Stamping engineers have noted that occasionally some parts will have regions strained well above the accepted strain limits without evidence of

localized necking, or that necking failures sometimes occur in regions where the strains are well below the FLD.

It has been generally accepted that for non-proportional loading conditions, if the pre-strain ratio is less than the final strain ratio, then the forming limit is increased. Alternatively, for a higher pre-strain ratio, the forming limit curve decreases [Lee and Kobayashi, 1975; Laukonis and Ghosh, 1978]. Laukonis and Ghosh [1978] studied the effects of a change in strain path on the deformation characteristics of aluminum killed steel and 2036-T4 aluminum sheets. The sheets were prestrained various amounts in balanced biaxial tension and the resulting uniaxial properties and forming limits for other loading paths were determined. The forming limit diagram of steel was found to decrease with prestrain at a much faster rate than that of aluminum. Laukonis and Ghosh [1978] explained such effects in terms of the transition flow behavior of the metals occurring upon the path change. More specifically, the path change produced strain softening and premature failure in steel, while causing additional strain hardening and consequent flow stabilization in aluminum. Graf and Hosford [1993] showed that varying the strain path for Al 2008-T4 can have tremendous effects on the FLD which is depicted in Figure 2.6. They applied various levels of uniaxial, in-plane plane strain, and biaxial pre-strains parallel and perpendicular to the rolling direction. They concluded that uniaxial pre-strain increases the left side of the FLD without causing much effect on right side where biaxial pre-stain lowers the entire FLD. For the in-plane plane strain pre-strain condition, the FLD increased slightly on both sides. Similar observations were made by Graf and Hosford [1994] for AA6111-T4.

The ability to include path changes in FLD calculations is important as number of potentially significant changes is too great to be thoroughly covered by experiments, and because

calculations allow general trends to be explored over a large range of variables. Within the M-K framework, the influence of strain path change has been intensively investigated [see e.g. Graf and Hosford, 1994; Wu *et al.*, 1998; Hiwatashi *et al.,* 1998; Kuroda and Tvergaard, 1999]. In these studies, non-proportional loading histories were developed using combinations of two linear strain paths. The first strain path, the pre-strain operation, was common to all loading

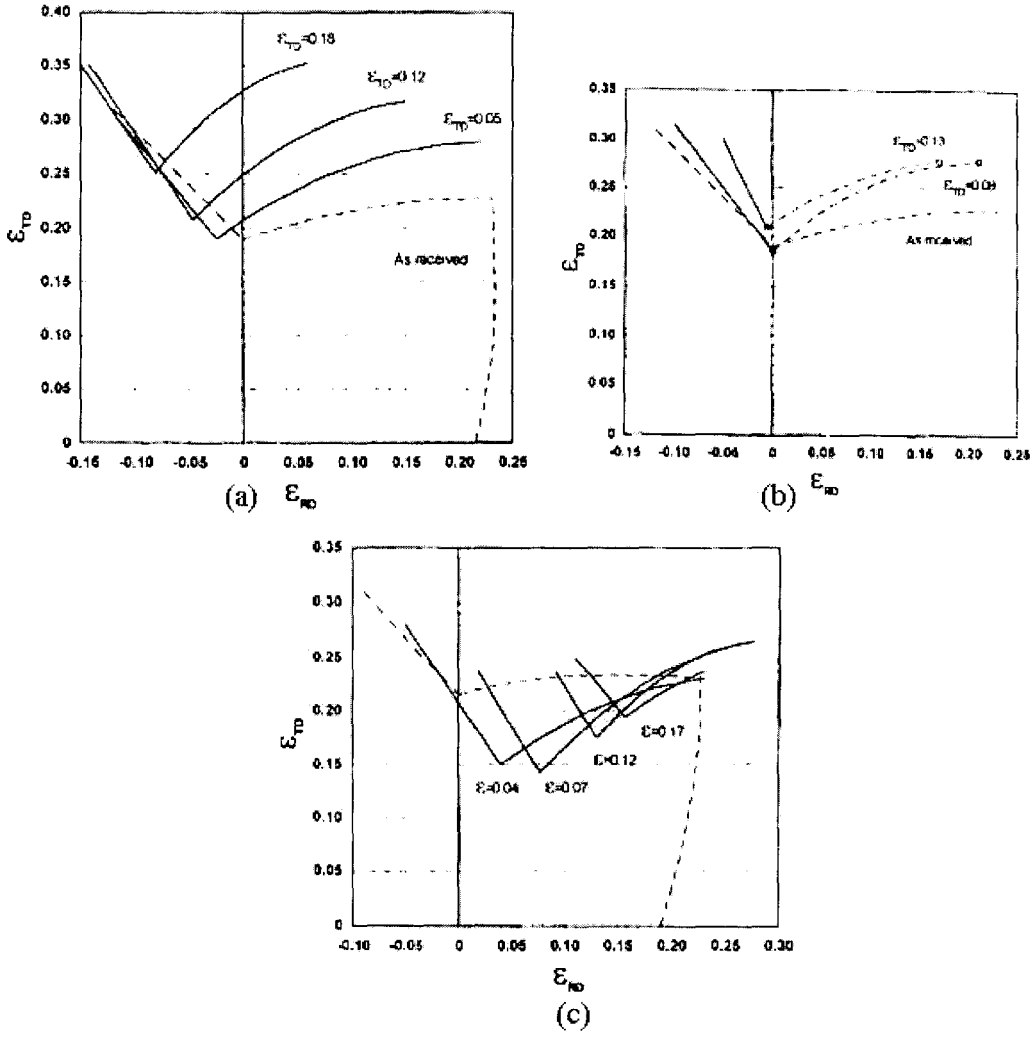

Figure 2.6: FLDs normal to RD (rolling direction) after pre-straining in (a) uniaxial tension, (b) in-plane plane strain tension and (c) equibiaxial tension of material Al 2008–T4 [Graf and Hosford, 1993].

histories. Subsequent linear deformation paths were imposed by varying the strain-rate ratio for the development of an FLD applicable to that given prestrain path and amount. They found that the predicted general trends of effects of strain path changes on forming limits are quite similar to those experimentally observed in steel and aluminum sheets [Laukonis and Ghosh, 1978; Graf and Hosford, 1994]. Recently, Tarigopula *et al* [2008] studied the elastic-plastic behavior of dual phase steel under non-proportional loading conditions by using a constitutive model of combined isotropic-kinematic hardening. They found the effect of strain path change quite reasonable with experimental evidence but failed to describe the transient deformation induced anisotropy in the plastic flow.

In this study the effect of changing strain path on damage evolution and formability is numerically studied using the Gurson model. To the best of knowledge, this is the first attempt to study the strain path change effect based on the Gurson type damage model.

2.8 Concept of Forming Limit Stress Diagram (FLSD)

From the experimental results of Graf and Hosford [1993 and 1994], it has been observed that a non-proportional loading history lowers/raises the forming limit curve from that observed under a monotonic loading path. There is no single curve in strain space that represents the forming limit, and this limits the use of conventional FLDs for assessing forming severity because the straining path of material elements in a real sheet metal forming process is usually not known with any certainty. Therefore, finding a single path-independent curve to characterize forming limits is of considerable practical interest. Knowing the drawback of conventional FLDs, Arrieux *et al.* (1982), among others, represented formability based on the state of stress rather than the state of strain. They constructed a Forming Limit Stress Diagram (FLSD) by plotting the

calculated principal stresses at necking. It was concluded that all FLSDs, based on phenomenological plasticity models such as Hill (1948) and Hosford (1979), were almost path-independent (Arrieux, 1995, Zhao *et al.,* 1996; Haddad *et al* , 2000; Stoughton, 2000; Zimniak, 2000, Stoughton and Zhu, 2004). Wu *et al.* [2005] carried out a detailed study to examine the path-dependency of FLSDs based on different non-proportional loading histories, which were combinations of two linear strain paths. All simulations were based on crystal plasticity theory in conjunction with the M-K approach. It was confirmed that the Forming Limit Diagram (FLD) and the FLSD are two mathematically equivalent representations of forming limits in strain-space and stress-space, respectively While the FLD was very sensitive to strain path changes, the FLSD was much less path-dependent. It was suggested by Wu *et al.* [2005] that the FLSD is much more favorable than the FLD in representing forming limits in the numerical simulation of sheet metal forming processes

However, there are two major drawbacks of an FLSD· obtaining experimental data for stress space compared to strain space is difficult, and a stress based criterion has poorer resolutions compared to a strain based criterion [Bai and Wierzbicki, 2008]

This study re-examines the path-dependency of the forming limit stress diagram based on the Gurson damage model, in conjunction with the M-K approach. The nature of the effect of a strain path change on forming limits is investigated in terms of the influence of pre-straining on the stress-strain curves for subsequent strain paths and the concept of the FLSD.

2.9 Application of FLD

The industrial applications of the sheet metal forming simulations have greatly impacted the automotive industry in many areas. product design, die developments, die construction, and

tryout and production stamping. The forming limit diagram has various ranges of use in the press shop: for failure analyses, material and process selection, die development and production control [Zhao, 1993]

2.9.1 Safety Judgment of Processes

With the help of an appropriate FLD, the safety region for certain processes can be determined. Figure 2.7 shows an experimentally determined FLD to make the assessment of how much the material can be formed before failure. Three regions of forming have been highlighted. the safety zone, marginal zone, and failure zone. Above, and near to the marginal region, material is anticipated to fail if changes in the process variables occur When the material's FLD remains below the safety region it can be assumed that more formability of material can possibly be attained.

2.9.2 Selection of Appropriate Material

The ability of materials to accomplish complex forming operations is a crucial matter for many industrial technologies. Formability of a material depends on material characteristics and the process variables of the forming operation. As a result, different materials have different formability curves, or FLDs, for different processes. For these reasons much analytical and experimental work has been done to predict many formability curves and a comparison was made so that appropriate materials would be selected for processes to which they were well suited.

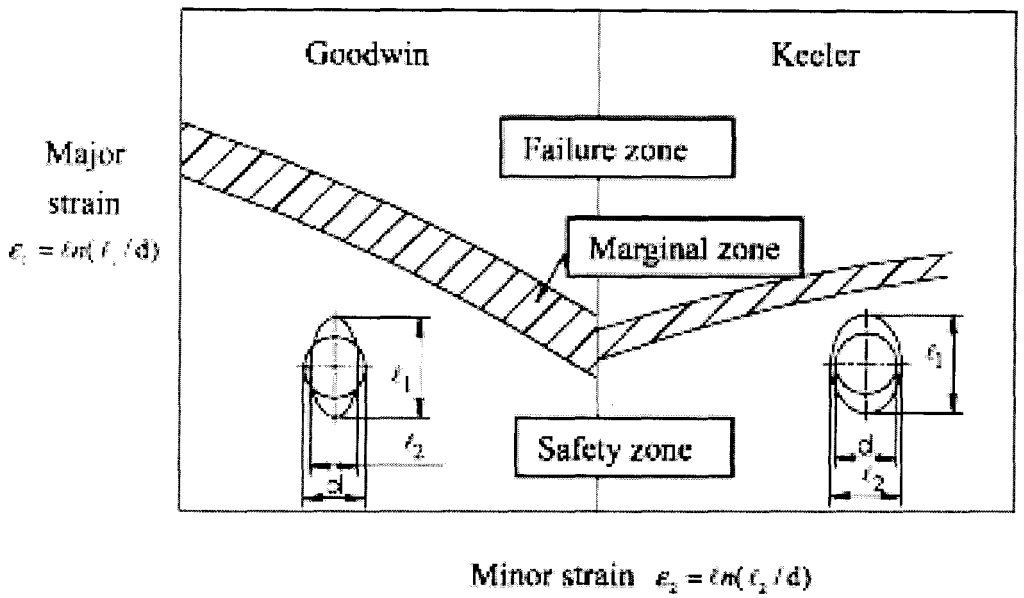

Figure 2.7: A typical forming limit diagram showing three important regions [Goodwin, 1968]

2.9.3 Design and Tryout of Dies

The simulation for die developments before production trials is a crucial design aspect from a business perspective which seeks to reduce lead-time, costs, and improve quality [Wang, 1999]. As a result, new challenges for forming (stamping) simulation and to production applications are developing rapidly. Thus, the demand for efficiency improvements in the automotive industry, both in process planning, and in die design, has driven the development and implementation of efficient simulation techniques from the initial stage of product development. Simulation based systems optimize the process by giving feedback to the following steps by making necessary corrections and improvements at minimum cost. This principle is illustrated in the schematic flow chart of simulation based process planning and die design shown in Fig. 2.8 [Tisza *et al.*,

2008]. Accurate dies reduce costs associated with processing because having an improper die can cause tearing and wrinkling in the sheet metal.

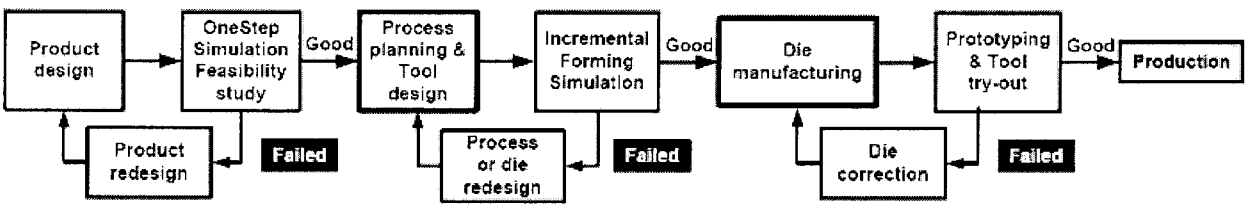

Figure 2.8: Workflow in simulation based process planning and die design [Tisza *et al.*, 2008].

2.9.4 Quality Control, Optimization, and Problem Solving in the Manufacturing Process

An FLD can be used for process quality control purposes, and for the forming of complex products. In different forming processes the final part which has to be acquired is defined by dimensional tolerances and mechanical properties of the material. Lowering manufacturing costs while still maintaining an acceptable accuracy is a trade-off commonly encountered in technological industries. In order to make the cost low, a detailed control of production systems is required [Gantar and Kuzman, 2002]. Elaborate knowledge of the parameters that affect the production process and the final product is needed. Because it is an involved undertaking to find all the parameters that might have an impact on the production process, the FLD obtained for a particular material can be very helpful for fail-safe analysis.

In real production systems the operating parameters and variables can be changed over a period of time. Some changes that may occur include: the location of the blank, wearing of dies, and the quality of stock and gauge material can degrade. Moreover, use of limit analysis on different processes can be used to determine the adjustments required for proper output.

CHAPTER 3

GURSON CONSTITUTIVE MODEL AND M-K ANALYSIS

3.1 Introduction

While the Gurson model has been the most widely known damage model for describing damage and fracture for ductile metals, most theoretical FLD analyses have been based on the M-K approach. This chapter gives a detailed formulation of the Gurson model and M-K approach.

3.2 Formulation of the Gurson Constitutive Model

Gurson (1977) developed his damage model based on averaging techniques. The characteristic volume element considered by Gurson is an aggregate of voids and rigid plastic matrix material. Approximate upper-bound solutions on the micro-level were used to derive a macroscopic yield condition for the material, which is given by

$$\phi(\sigma,\sigma_H,\bar{\sigma},f)=\frac{\sigma_e^2}{\bar{\sigma}^2}+2f\cosh\left(\frac{\sigma_H}{2\bar{\sigma}}\right)-\left(1+f^2\right)=0 \tag{3.1}$$

Here, σ_e is effective stress, and σ_H is the mean stress which can be defined in terms of the macroscopic Cauchy stress, σ, and deviatoric Cauchy stress, σ'.

$$\sigma_e{}^2=\frac{3}{2}\boldsymbol{\sigma}':\boldsymbol{\sigma}', \tag{3.2}$$

$$\sigma_H=I:\frac{1}{3}\sigma, \tag{3.3}$$

$$\sigma'=\sigma-\sigma_H I, \tag{3.4}$$

$$f=\frac{V_{void}}{V} \tag{3.5}$$

Here, I = second order identity tensor, (:) denotes dyadic product, f is the void volume fraction, V_{void} *and* V are the volume of the void and the total volume, respectively.

.Later, Tvergaard [1982] introduced additional constants q_1 , q_2 and q_3 to bring predictions of the Gurson constitutive relation into closer agreement with corresponding results of full numerical analyses for a periodic array of voids. His modified yield function is

$$\phi(\boldsymbol{\sigma}, \sigma_H, \bar{\sigma}, f) = \frac{\sigma_e^{\,2}}{\bar{\sigma}^2} + 2fq_1 \cosh\left(\frac{3q_2\sigma_H}{2\bar{\sigma}}\right) - \left(1 + q_3 f^2\right) = 0 \tag{3.6}$$

The description of Gurson constitutive model is completed by the description of visco-plastic strain rate and hardening law of solid:

$$\dot{\bar{\varepsilon}} = \dot{\varepsilon}_0 \left(\bar{\sigma} / g(\bar{\varepsilon})\right)^{\frac{1}{m}} \tag{3.7}$$

$$g(\bar{\varepsilon}) = \sigma_0 \left(\bar{\varepsilon} / \varepsilon_0 + 1\right)^N . \tag{3.8}$$

Here $g(\bar{\varepsilon})$ describes the hardening law, and $\dot{\bar{\varepsilon}}$ is the visco-plastic strain rate which depends on the accumulated plastic strain, $\bar{\varepsilon}$, and equivalent stress, $\bar{\sigma}$. N and m are the strain hardening, and strain rate hardening exponents, respectively. ε_0 and $\dot{\varepsilon}_0$ are respectively the reference strain and strain rate, and $\sigma_0 = E * \varepsilon_0$ where E refers to Young's modulus.

In the material, total rate of deformation, D, is the sum of elastic and plastic parts

$$D = D^e + D^P \tag{3.9}$$

The elastic deformation part is

$$D^e = L^{-1} : \overset{\nabla}{\sigma} \tag{3.10}$$

Here, $\overset{\nabla}{\sigma}$ is Jaumann derivative of Cauchy stress described as

$$\overset{\nabla}{\sigma} = \dot{\sigma} + \sigma W - W\sigma \tag{3.11}$$

Where, W is the spin tensor. L is the elastic compliance (tensor of elastic modulus).

$$L_{ijkl} = \frac{E}{1+\nu}\left[\frac{1}{2}\left(\delta_{ik}\delta_{jl} + \delta_{il}\delta_{jk}\right) + \frac{\nu}{1-2\nu}\delta_{ij}\delta_{kl}\right],$$

where, v is Poisson's ratio.

Then the plastic deformation part is

$$\mathbf{D}^p = \dot{\chi}\frac{\partial \phi}{\partial \underset{\sim}{\boldsymbol{\sigma}}} \tag{3.12}$$

$$\Rightarrow \mathbf{D}^p = \dot{\chi}\, \underset{\sim}{p} \tag{3.13}$$

Here, $\dot{\chi}$ is proportionality factor and $\frac{\partial \phi}{\partial \underset{\sim}{\sigma}} = \underset{\sim}{p}$ is visco-plastic strain rate direction. Substituting equation (3.10) and (3.13) into (3.9), we have

$$D = L^{-1} : \overset{\nabla}{\sigma} + \dot{\chi}\frac{\partial \phi}{\partial \sigma}$$

$$\overset{\nabla}{\sigma} = L : \left(D - D^P\right) = L : D - \dot{\chi}P \tag{3.14}$$

Here, $P = L : \underset{\sim}{p} = L : \frac{\partial \phi}{\partial \underset{\sim}{\sigma}}$

In the isotropic Gurson model the macroscopic strain increment and effective plastic strain increment are assumed to be related by the equivalent plastic work expression as

$$\sigma : D^P = (1-f)\overline{\sigma}\dot{\overline{\varepsilon}} \tag{3.15}$$

This is an exact relationship for $f = 0$ and a reasonable assumption for the porous solid. From equation (3.13) and (3.15) the proportionality factor is found as

$$\dot{\chi} = \frac{(1-f)\overline{\sigma}\dot{\overline{\varepsilon}}}{\boldsymbol{\sigma} : \mathbf{p}} \tag{3.16}$$

The consistency condition gives

$$\dot{\phi} = \frac{\partial \phi}{\partial \boldsymbol{\sigma}} : \overset{\nabla}{\boldsymbol{\sigma}} + \frac{\partial \phi}{\partial \bar{\sigma}} \dot{\bar{\sigma}} + \frac{\partial \phi}{\partial f} \dot{f} = 0 \tag{3.17}$$

In this above condition $\dot{f}$ is the increase of void volume fraction, $\dot{\bar{\sigma}}$ rate of change of matrix equivalent stress. $\dot{\bar{\sigma}}$ can be determined from equation (3.16) such that

$$\dot{\bar{\sigma}} = -\frac{\left(\frac{\partial \phi}{\partial \boldsymbol{\sigma}} : \overset{\nabla}{\boldsymbol{\sigma}} + \frac{\partial \phi}{\partial f} \dot{f}\right)}{\frac{\partial \phi}{\partial \bar{\sigma}}} = -\frac{\left(\boldsymbol{p} : \overset{\nabla}{\boldsymbol{\sigma}} + \frac{\partial \phi}{\partial f} \dot{f}\right)}{\frac{\partial \phi}{\partial \bar{\sigma}}} \tag{3.18}$$

The increase of void volume fraction $(\dot{f})$ results from the nucleation of new voids as well as the growth of existing voids, thus

$$\dot{f} = (\dot{f})_{growth} + (\dot{f})_{nucleation} \tag{3.19}$$

The growth of existing voids is based on the approach of plastic incompressibility which means deformation takes place without volume change.

$$(\dot{f})_{growth} = (1 - f)\boldsymbol{I} : \boldsymbol{D}^{p} \tag{3.20}$$

The nucleation of micro-voids occurs from the normal distribution model of Chu and Needleman [1980] as

$$(\dot{f}) = a\dot{\bar{\varepsilon}} + A\dot{\bar{\sigma}} + \frac{1}{3} B\mathbf{I} : \overset{\nabla}{\boldsymbol{\sigma}} \tag{3.21 }$$

For plastic strain controlled nucleation

$$a = \frac{f_n}{S_n \sqrt{2\pi}} \exp\left\{ -\frac{1}{2} \left(\frac{\varepsilon^{p} - \varepsilon_n}{S_n} \right)^2 \right\}. \tag{3.22}$$

Here, for an assumed normal distribution, s_n is the standard deviation, f_n is the volume fraction of voids which will nucleate if deformation continues indefinitely and high strain values are

reached, and finally ε_n is the strain at which void nucleation reaches its maximum value. ε^p is effective plastic strain which nucleates between two normal distribution model values respectively $\varepsilon_n + s_n$ and $\varepsilon_n - s_n$.

For stress controlled nucleation

$$A = B = \frac{f_n}{S_n\sqrt{2\pi}} \exp\left\{-\frac{1}{2}\left(\frac{\bar{\sigma} + \frac{1}{3}\sigma_H - \sigma_n}{S_n}\right)^2\right\}. \tag{3.23}$$

Again, for a normal distribution, s_n is the standard deviation, f_n is the volume fraction of voids which will nucleate if deformation continues indefinitely, and σ_n is the stress at which void nucleation reaches its maximum value. The nucleation criterion that is based on the maximum stress transmitted through the particle-matrix interface was suggested by Argon, *et al.* [1975] and an approximate measure of this maximum stress is considered to be $\bar{\sigma} + \frac{1}{3}\sigma_H$.

Substituting equation (3.19), and (3.20) into (3.21), one obtains

$$\dot{f} = (1-f)\boldsymbol{I} : \boldsymbol{D}^p + a\dot{\bar{\varepsilon}} + A\dot{\bar{\sigma}} + \frac{1}{3}B\boldsymbol{I} : \overset{\nabla}{\boldsymbol{\sigma}} \tag{3.24}$$

The effect of void coalescence and material failure can be expressed with the help of void volume fraction $f^*(f)$ [Needleman and Tvergaard; 1984]

If $f < f_c$ then $f^* = f$ (3.25)

If $f \geq f_c$ then $f^* = f_c + \frac{f_u^* - f_c}{f_f - f_c}(f - f_c)$ (3.26)

Here, f_c is the critical value of void volume fraction at which void coalescence occurs and stress carrying capacity of material sharply drops. f_u^* is the ultimate value of void volume fraction at

which ductile rapture occurs and the value is equal to $\frac{1}{q_1}$. f_f is the value of the void volume fraction at which final fracture occurs where the stress carrying capacity of material totally diminishes. If $q_3 = (q_1)^2$ the ultimate void volume fraction f_u^* equals to $(1/q_1)$.

One step time integration method widely known as tangent modulus method for analyzing solids characterized by elastic-plastic constitutive relations has been incorporated in this study. The development of rate dependent tangent modulus method for Gurson constitutive relation (3.14) has the expression as (See Appendix A for details)

$$\overset{\nabla}{\boldsymbol{\sigma}} = \boldsymbol{L} : \boldsymbol{D} - \dot{\bar{\sigma}}\,, \tag{3.27}$$

Where

$$\boldsymbol{L} = \boldsymbol{L}^e - \frac{\xi}{1+\xi}\frac{1}{H}\boldsymbol{P}\boldsymbol{Q}$$

and

$$\dot{\bar{\sigma}} = +\frac{\boldsymbol{P}}{1+\xi}\dot{\chi}_t$$

3.3 M-K analysis

The basic assumption of the M-K approach is the existence of initial material or geometric imperfections in the form of a groove or band as shown in Figure 3.1. Here, a region A which is homogenous (where proportional straining is maintained), and a region B (narrow band) which is inhomogeneous have been defined. The narrow band or groove is assumed to be at an angle ψ to

the x_2 direction as shown in figure 3.1. If ψ_0 is the initial orientation, then after deformation, the current groove orientation ψ is given by

$$\tan\psi = \exp(\varepsilon_{11} - \varepsilon_{22})\tan\psi_0 \tag{3.28}$$

Here, ε_{11} and ε_{22} are principal logarithmic (true) strains in x_1 and x_2 direction.

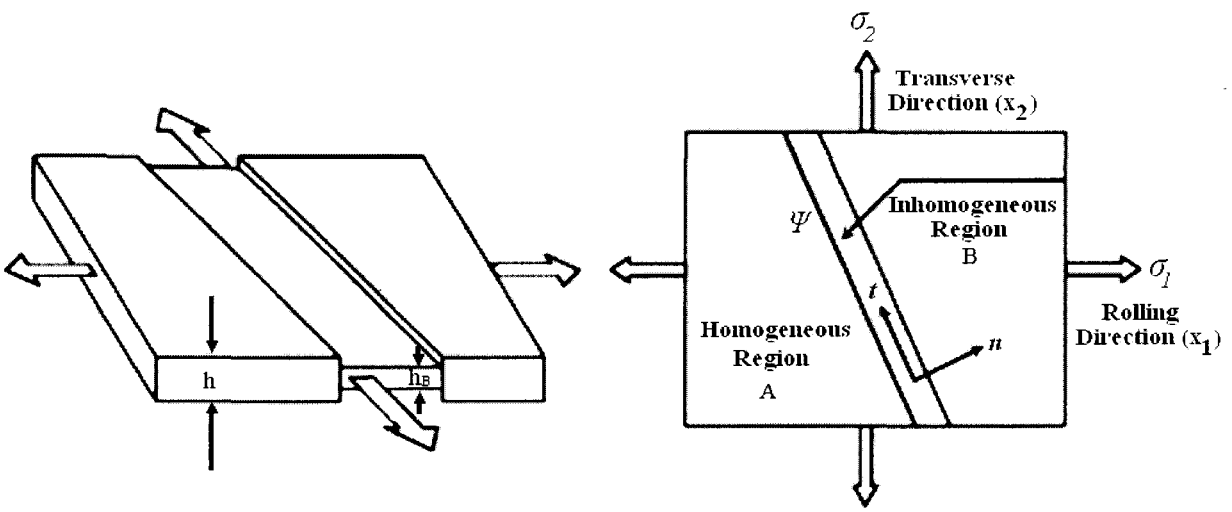

Figure 3.1: Geometry and convention used in M-K analysis

All the quantities inside the band are denoted by $(\,)^B$. The thicknesses of the groove and the parent sheet are h^B and h respectively. So the initial imperfection or non-uniformity of the sheet is defined by

$$\xi = \frac{h}{h_B} \tag{3.29}$$

In the region A (outside the band) the deformation can be controlled by either the strain or stress. If it is strain controlled, the loading can be described by the strain ratio ρ:

$$\frac{D_{22}}{D_{11}} = \frac{\dot{\varepsilon}_{22}}{\dot{\varepsilon}_{11}} = \rho, D_{12} = 0, W_{12} = 0 \tag{3.30}$$

Likewise, if the imposed deformation is stress controlled,

$$\frac{\dot{\sigma}_{22}}{\dot{\sigma}_{11}} = \alpha, \ \dot{\sigma}_{12} = 0 \tag{3.31}$$

Where, α is constant.

It is further assumed, in both cases, that D_{13}=D_{23}=W_{13}=W_{23}=0, while D_{33} is specified by the condition $\dot{\sigma}_{33}$=0. For the isotropic materials considered here, these boundary conditions imply that the stress components σ_{13}=σ_{23}=0. In equation (3.29) it is assumed that the principal logarithmic strain rates are equal to the deformation such that $\dot{\varepsilon}_{22} = D_{22}$ and $\dot{\varepsilon}_{11} = D_{11}$. Some of the important strain paths are defined as follows in terms of strain-rate and stress-rate ratios.

- Uniaxial tension: $\alpha = 0$
- Equibiaxial tension: $\alpha = 1$
- Uniaxial stretching: $\rho = -0.5$
- In-plane plane strain tension: $\rho = 0$
- Equi-biaxial stretching: $\rho = 1$

It is noted that for isotropic materials, the equibiaxial tension (α = 1) and equi-biaxial stretching (ρ = 1) are identical.

Apart from the necessary conditions at the band interface, equilibrium and compatibility inside and outside the band are automatically satisfied because uniform deformations are assumed both inside and outside the band. Following Hutchinson and Neale [1978], the compatibility condition at the band interface is given in terms of the differences in the velocity gradients inside and outside the band:

$$L^{B}_{\alpha\beta} = L_{\alpha\beta} + g_{\alpha} N_{\beta} \tag{3.32}$$

or

$$D^B_{\alpha\beta} = D_{\alpha\beta} + \frac{1}{2}\left(g_\alpha N_\beta + N_\alpha g_\beta\right) \tag{3.33}$$

$$W^B_{\alpha\beta} = W_{\alpha\beta} + \frac{1}{2}\left(g_\alpha N_\beta - N_\alpha g_\beta\right) \tag{3.34}$$

Here, the α and β subscripts range from 1 to 2, and g_α is the parameter to be determined. N_β are the current unit normals to the band which is given by $N_1 = \cos\psi$ and $N_2 = \sin\psi$.

The equilibrium condition at the band interface for the current configuration is given at time t by

$$N_\alpha \sigma^B_{\alpha\beta} h_B = N_\alpha \sigma_{\alpha\beta} h \tag{3.35}$$

A set of incremental equations for g_α is now obtained by substituting the incremental constitutive equations (3.27) into the incremental form of (3.35), using (3.33) to eliminate the strain increments $D^b_{\alpha\beta}$. Together with the condition $\dot{\sigma}^b_{33} = 0$, this furnishes three algebraic equations for solving g_1, g_2 and the unknown D^b_{33} [See appendix B for details]:

$$\begin{bmatrix} \overline{R}_{11} & \overline{R}_{12} & \overline{R}_{13} \\ \overline{R}_{21} & \overline{R}_{22} & \overline{R}_{23} \\ \overline{R}_{31} & \overline{R}_{32} & \overline{R}_{33} \end{bmatrix} \begin{bmatrix} g_1 \\ g_2 \\ D^B_{33} \end{bmatrix} = \begin{bmatrix} \dot{f}_1 \\ \dot{f}_2 \\ \dot{f}_3 \end{bmatrix} \tag{3.36}$$

The sheet thickness outside the band h and inside the band h^b are updated based on the relations

$$\dot{h} = D_{33} h, \qquad \dot{h}^b = D^b_{33} h^b \tag{3.37}$$

When the principal strain rates inside the band become much higher than that outside the band it is assumed that the onset of localization has occurred. This condition is described below

$$\frac{\dot{\varepsilon}^B}{D_{11}} \geq 10^5 \tag{3.38}$$

Here, $\dot{\varepsilon}^B$ is the maximum strain rate inside the band. When this condition is reached, the corresponding principal logarithmic strains ε_{11}^* and ε_{22}^*, and principal stresses σ_{11}^* and σ_{22}^* outside the band are the limit strains and limit stresses respectively. For a real sheet, numerous initial imperfections can exist with different orientations. A conservative estimate of the forming limit strain is that obtained from limit strain values for various values of the initial groove orientation ψ_0, and then selecting the minimum value as the actual forming limit strain. The entire FLD of a sheet is determined by repeating the procedure for different strain paths outside the band as prescribed by the strain-rate ratio ρ or stress-rate ratio α.

The non-proportional loading histories are developed using combinations of two linear strain paths. The first strain path, the pre-strain operation, is common to all loading histories. Subsequent linear deformation paths are imposed by varying the strain-rate ratio for the development of an FLD applicable to that given pre-strain path and amount.

CHAPTER 4

EFFECTS OF STRAIN PATH CHANGE ON HARDENING AND DAMAGE EVOLUTION USING THE GURSON MODEL

4.1 Introduction

Sheet metal forming processes are a combination of different forming modes. Different modes of forming give rise to various strain path changes. When the strain path is changed in a deformation process the work-hardening and the flow strength differ from the monotonic deformation characteristics [Hutchinson *et al,* 1976; Zandrahimi *et al*, 1989]. Therefore, it is important to understand the material plastic behavior under non-proportional loading conditions. In this chapter the Gurson constitutive model (formulated in Chapter 3) is used to study the work hardening behavior and damage evolution under strain path changes.

4.2 Mechanical Properties of Material

The material to be analyzed has an initial void volume fraction, $f_0 = 0.01$, and a volume fraction of void nucleating particles $f_n = 0.05$ which nucleates at a plastic strain of $\varepsilon_n = 0.3$ with a standard deviation of $S_n = 0.1$. The nucleation is considered to be plastic strain controlled. The Gurson model parameters (Equation 3.6) are considered to be q_1=1.5, q_2 =1 as suggested by Tvergaard [1982]. Material failure parameters i.e. void volume fraction of coalescence, and fracture are f_c= 0.2 and f_f = 0.25, respectively. Values of the other parameters ar$\sigma_0 = 1$, $\varepsilon_0 = \frac{\sigma_0}{E} = 0.02$, $\nu = 0.3$, n= 0.2 and m= 0.01.

4.3 Effect of Strain Path Changes

4.3.1 Monotonic Loading

The stress-strain responses of the material subjected to three different proportional loading (no strain path change) conditions: uniaxial stretching $(\rho = -0.5)$, in-plane plane strain tension $(\rho = 0)$, and equi-biaxial stretching $(\rho = 1)$ are shown in Figure 4.1. For the in-plane plane strain condition, the flow stress, σ_{11}, reaches the highest value compared to the other two conditions. For uniaxial stretching the material fails at a higher strain, ε_{11}, compared to the other two monotonic loading conditions.

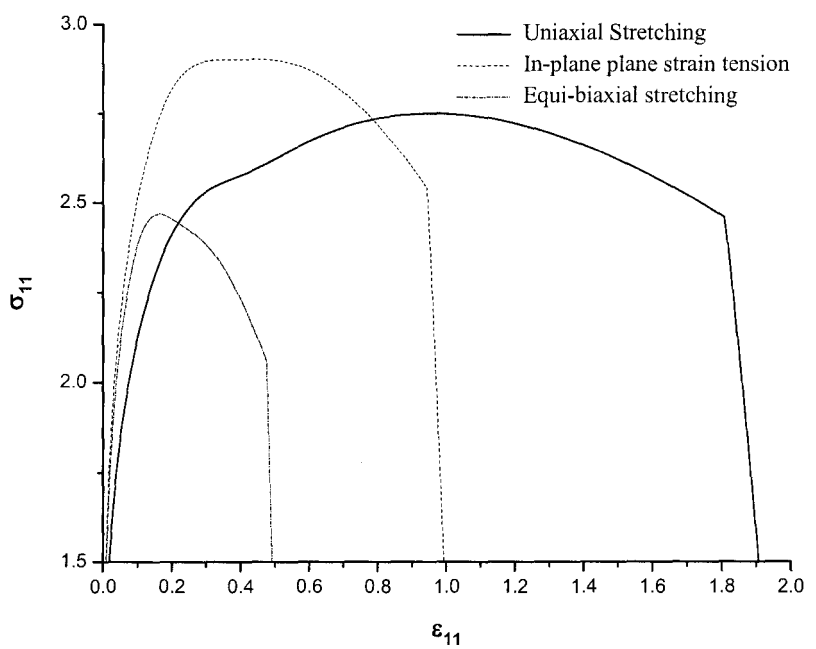

Figure 4.1a: Calculated σ_{11} vs. ε_{11} curves for various proportional loading conditions.

Usually, a true stress-strain curve for a material increases continuously up to fracture, but in this model after reaching the maximum value, the stress carrying capacity of the material starts to diminish because the void volume fraction increases, see Figure 4.1b.

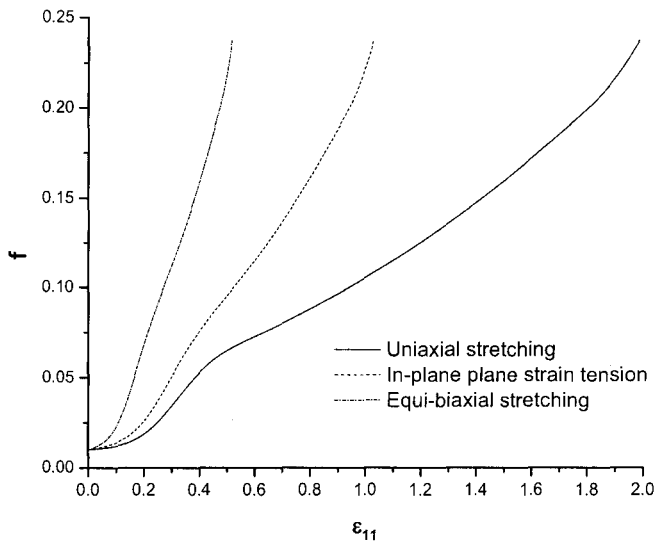

Figure 4.1b: Calculated f vs. ε_{11} curves for various proportional loading conditions.

Figure 4.1b shows the evolution of void volume fraction, f, with the imposed deformation. When f reaches a value equal to 95% of the final void volume fraction, the calculation is stopped. If the cutoff was not implemented the calculations would become unstable. For uniaxial stretching the failure occurs at a higher strain, ε_{11}, than the other two loading conditions. For the in-plane plane strain condition, f reaches its failure point at a higher strain than when the material is subjected to an equi-biaxial stretch.

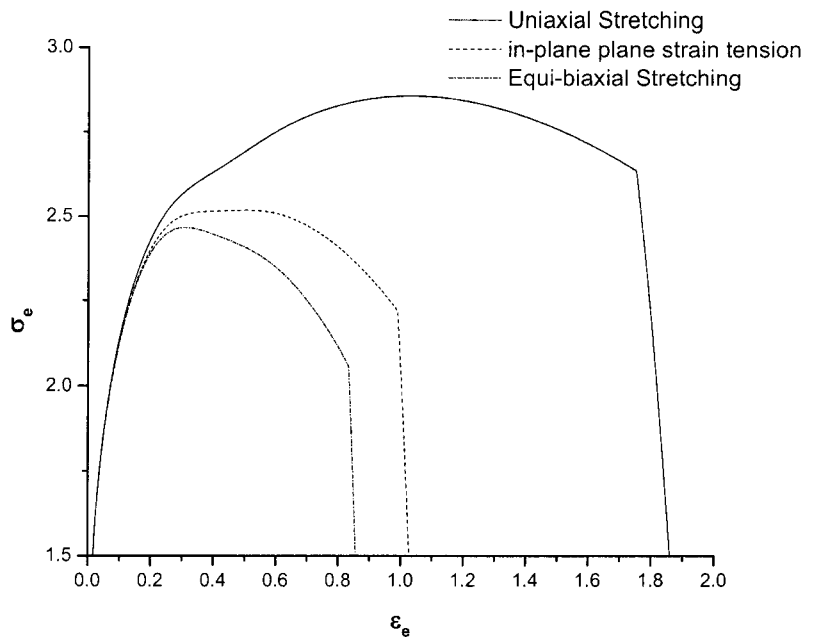

Figure 4.1c: Calculated σ_e vs. ε_e curves for various proportional loading conditions.

The data in Figures 4.1a and b can be expressed in terms of effective stress σ_e and effective strain ε_e. In Figure 4.1c the effective stress σ_e reaches a maximum point then decreases due to the increase of the void volume fraction *f*. The maximum values of σ_e and ε_e are attained in the uniaxial stretching condition compared to the other two monotonic loading conditions. This observation becomes clear in figure 4.1d which shows that the void growth is much slower in uniaxial stretching than in the other two deformation processes. In the following sections the material is first pre-strained in one deformation mode and then reloaded in another deformation mode [see Table 4.1].

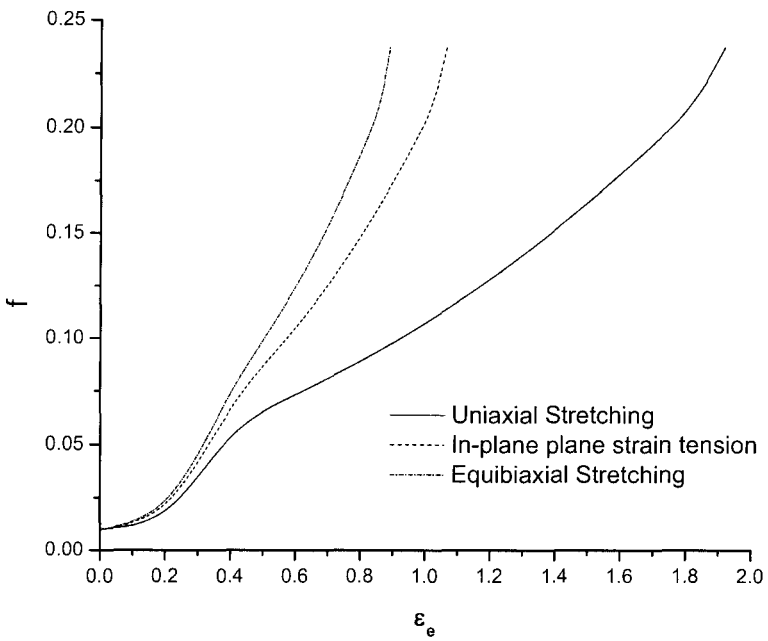

Figure 4.1d: Calculated f vs. ε_e curves for various proportional loading conditions.

Table 4.1: Combinations of non-proportional loadings.

Case	Pre-straining	Re-loading
1	Equi-biaxial stretching *(ρ=1)*	Uniaxial stretching*(ρ=-0.5)*
2	Uniaxial stretching*(ρ=-0.5)*	Equi-biaxial stretching *(ρ=1)*
3	In-plane plane strain tension $(\rho = 0)$	Uniaxial stretching*(ρ=-0.5)*
4	Uniaxial stretching*(ρ=-0.5)*	In-plane plane strain tension $(\rho = 0)$
5	In-plane plane strain tension $(\rho = 0)$	Equi-biaxial stretching *(ρ=1)*
6	Equi-biaxial stretching *(ρ=1)*	In-plane plane strain tension $(\rho = 0)$

4.3.2 Effect of Equi-biaxial Pre-straining on Uniaxial Stretching

Figure 4.2 shows the curves obtained under uniaxial stretching (ρ=-0.5) after being pre-strained in equi-biaxial stretching to different levels (ε_p=*0.05, 0.1*). The curves are compared to the monotonic uniaxial stretching curve (denoted: as received). Figure 4.2 (a) shows the stress-strain $(\sigma_{11} - \varepsilon_{11})$ response of the imposed deformation. The effect of equi-biaxial pre-straining on subsequent uniaxial stretching is a very quick falling behavior in the stress-strain curve. This behaviour can be explained from Figure 4.1a which shows that equi-biaxial stretching has a much higher hardening rate than uniaxial stretching when ε_{11} is relatively small $(\varepsilon_{11} < 0.12)$. At larger strains $(\varepsilon_{11} > 0.6)$ the pre-straining effect results in a lower flow stress when subjected to subsequent uniaxial stretching (Figure 4.2 (a)). This trend is observed by Kuroda and Tvergaard [2000] using Hill's anisotropic model [1990] and applying abrupt strain path changes from equi-biaxial stretching to uniaxial tension.

Figure 4.2a shows that the material fails at an earlier strain, ε_{11}, when pre-strained equi-biaxially than when subjected to a monotonic uniaxial loading condition. This phenomenon can be described with Figure 4.2b which shows the evolution of void volume fraction, *f*. with imposed deformation. In Figure 4.2b the evolution of *f* due to an equi-biaxial pre-strain followed by a re-loading uniaxially (CASE #1) is compared with a monotonic uniaxial stretch. Due to pre-straining the fracture point is reached at a smaller strain than that in the monotonic uniaxial loading condition.

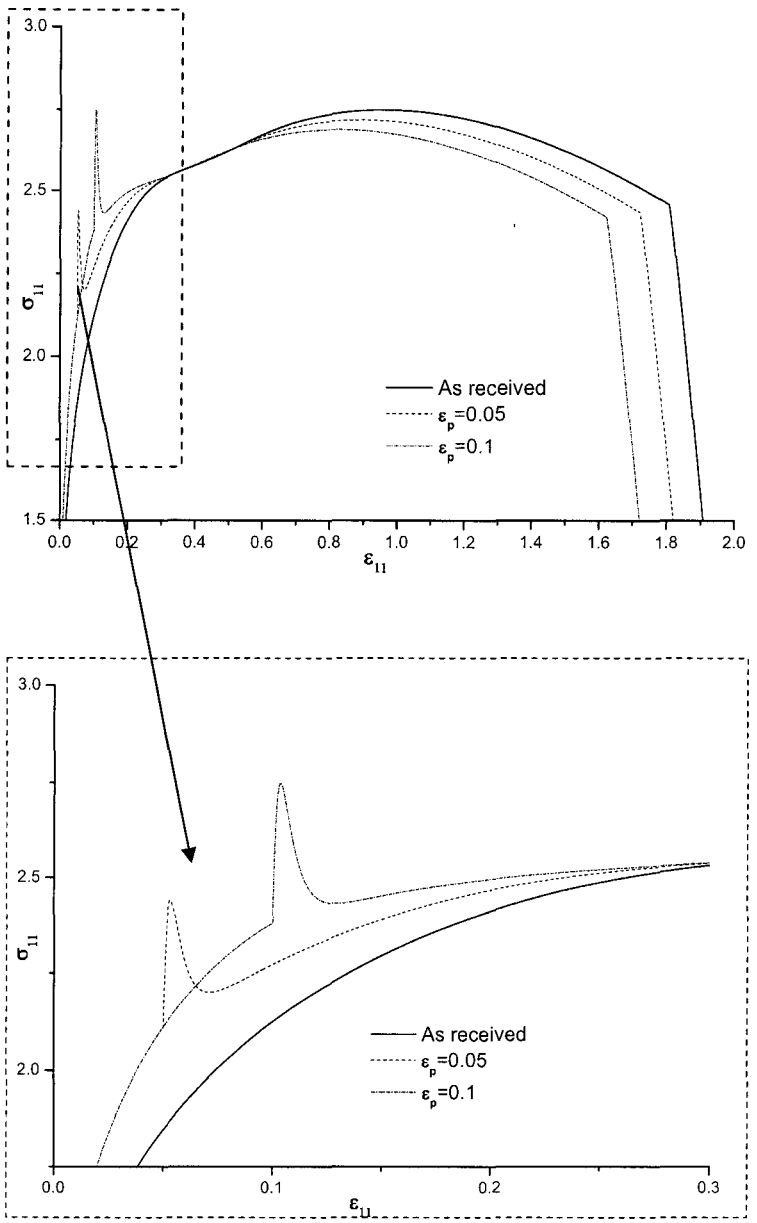

Figure 4.2a: Calculated σ_{11} vs. ε_{11} curves for uniaxial stretching after the sheet has been pre-strained to different levels of equi-biaxial stretching ($\rho=1$).

These results clearly indicate that if a sheet material is pre-strained equi-biaxially and then loaded uniaxially (CASE #1), the material suffers more damage and is weakened to a

greater extent than when subjected to a single uniaxial stretch. This is supported by the experiments carried out by Laukonis and Ghosh [1978] on AA 2036-T4.

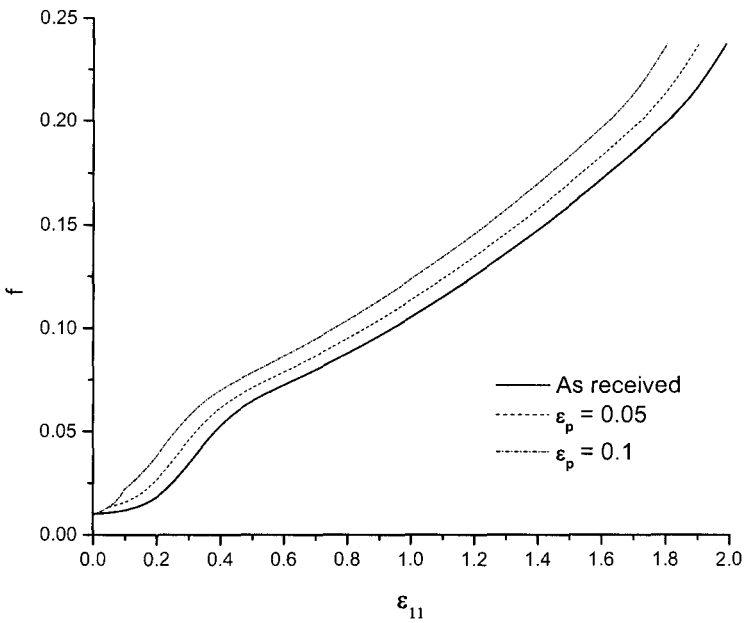

Figure 4.2b: Calculated *f vs.* ε_{11} curves for uniaxial stretching after the sheet has been pre-strained to different levels of equi-biaxial stretching ($\rho=1$).

4.3.3 Effect of Uniaxial Pre-strain on Equi-biaxial Stretching

The effect of uniaxial pre-straining ($\rho=-0.5$) to different levels ($\varepsilon_p=0.05,\ 0.1$) on equi-biaxial stretching is shown in Figure 4.3. The curves are compared with the monotonic equi-biaxial stretching curve (as received). In Figure 4.3a shows the stress-strain $(\sigma_{11}-\varepsilon_{11})$ response of the imposed deformation. From this figure it can be observed that at larger strains $(\varepsilon_{11} > 0.2)$ the pre-straining increases the flow stress in subsequent equi-biaxial stretching. However, when ε_{11}

is relatively small $(\varepsilon_{11} < 0.15)$, uniaxial stretching lowers the flow stress in subsequent equi-biaxial stretching. These observations are very similar to those reported by Kuroda and Tvergaard [2000].

The material fails at a higher strain ε_{11} when pre-strained uniaxially than when under a monotonic equi-biaxial stretching deformation. Figure 4.3b shows the evolution of void volume fraction, *f*, with the imposed deformation. It can be observed that an equi-biaxial stretch with a uniaxial pre-strain causes the material to fail at a greater strain than without the pre-strain. Thus, if a sheet material is pre-strained in uniaxially then reloaded equi-biaxially (Case#2) its strength increases due to the delay of damage (void volume fraction) compared to a monotonic equi-biaxial stretching.

This response can be expressed in terms of effective stresses and strains $(\sigma_e - \varepsilon_e)$ In Figure 4.3c the effective stress σ_e, reaches a maximum point then decreases due to the increase of *f*. Under a uniaxial pre-strain, σ_e attains a higher value and fails at a slightly lower value of effective strain ε_e, compared to the monotonic equi-biaxial stretching condition. This observation becomes clear in Figure 4.3d which shows that the void growth is slightly higher when pre-straining is applied than with just a monotonic deformation process.

The evolution of effective stress and strain (Figure 4.3c) and void volume fraction (Figure 4.3d) for the above mentioned condition (CASE #2) shows a weakening of sheet material and it fails earlier compared to the monotonic equi-biaxial loading response. This is due to the monotonic effective uniaxial stretching curve having a higher hardening rate and voids growth than the equi-biaxial stretching response, see Figures 4.1c and d.

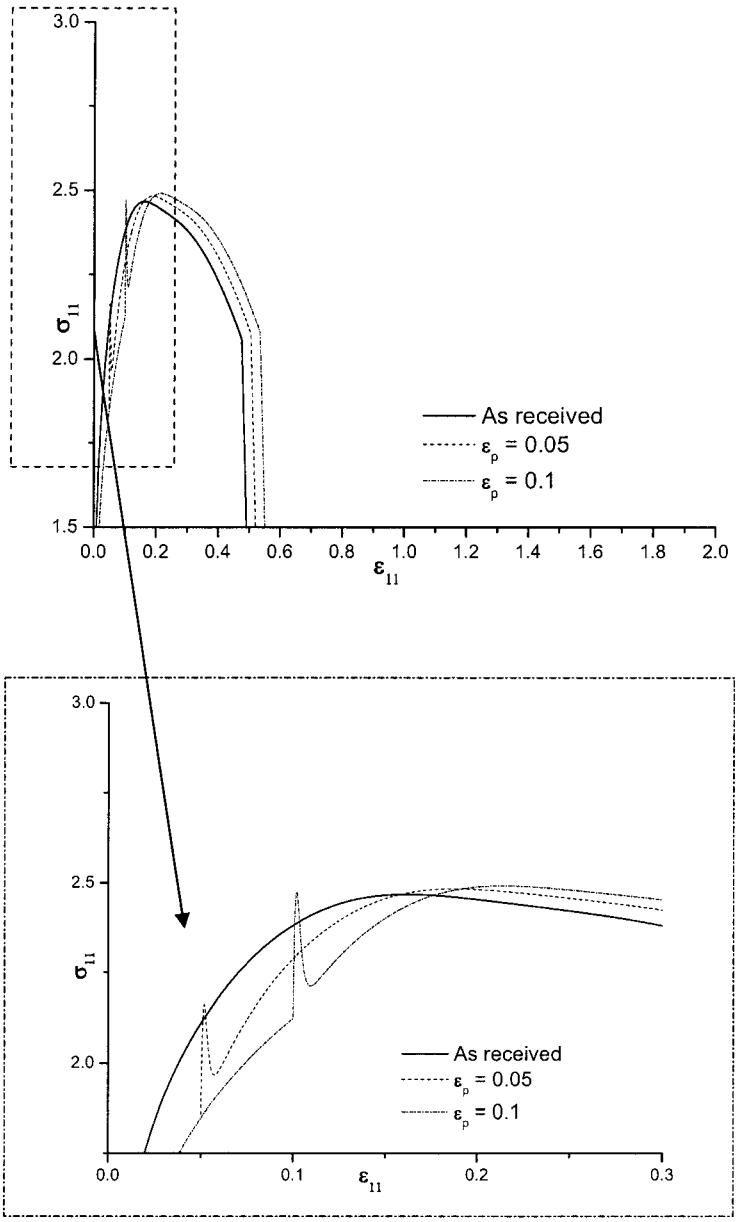

Figure 4.3a : Calculated σ_{11} vs. ε_{11} curves for equi-biaxial stretching after the sheet has been pre-strained to different levels of uniaxial stretching *(ρ=-0.5).*

4.3.4 Effect of an In-plane Plane Strain Pre-strain on Uniaxial Stretching

Figure 4.4 shows the curves obtained under an in-plane plane strain pre-strain $(\rho = 0)$ to different levels *(ε_p=0.05, 0.1)*, followed by uniaxial stretching $(\rho = -0.5)$. Figure 4.4a shows the stress-strain $(\sigma_{11} - \varepsilon_{11})$ response of the imposed deformation. As shown in figure 4.1a, the hardening rate in in-plane plane strain tension is much higher than that in uniaxial stretching. When the strain path is changed from uniaxial tension to in-plane plane strain tension, an abrupt drop in hardening rate is observed. At large strains $(\varepsilon_{11} > 0.2)$, the pre-strain results in a decrease of the flow stress. Figure 4.4b shows the evolution of the void volume fraction with deformation. Due to the in-plane plane strain pre-straining, f reaches its fracture limit at an earlier strain ε_{11}. All the figures show that in-plane plane strain pre-straining (CASE#3) weakens the material slightly due to an increase of the void volume fraction and fails earlier than the monotonic uniaxial stretching deformation. A similar observation can be found in [Ghosh and Backofen, 1972].

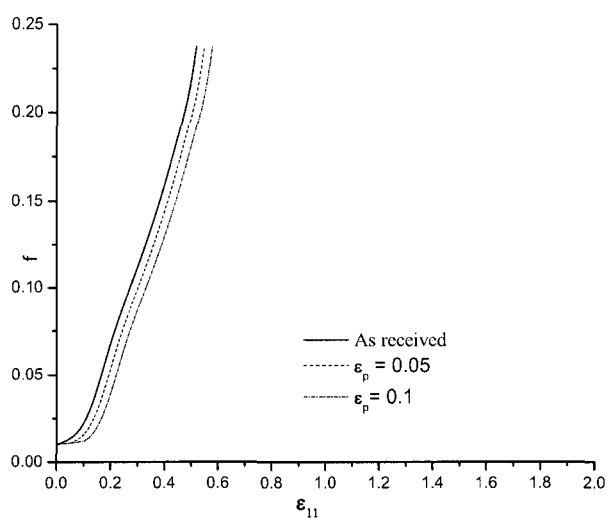

Figure 4.3b : Calculated f vs. ε_{11} curves for equi-biaxial stretching after the sheet has been pre-strained to different levels of uniaxial stretching *(ρ=-0.5)*.

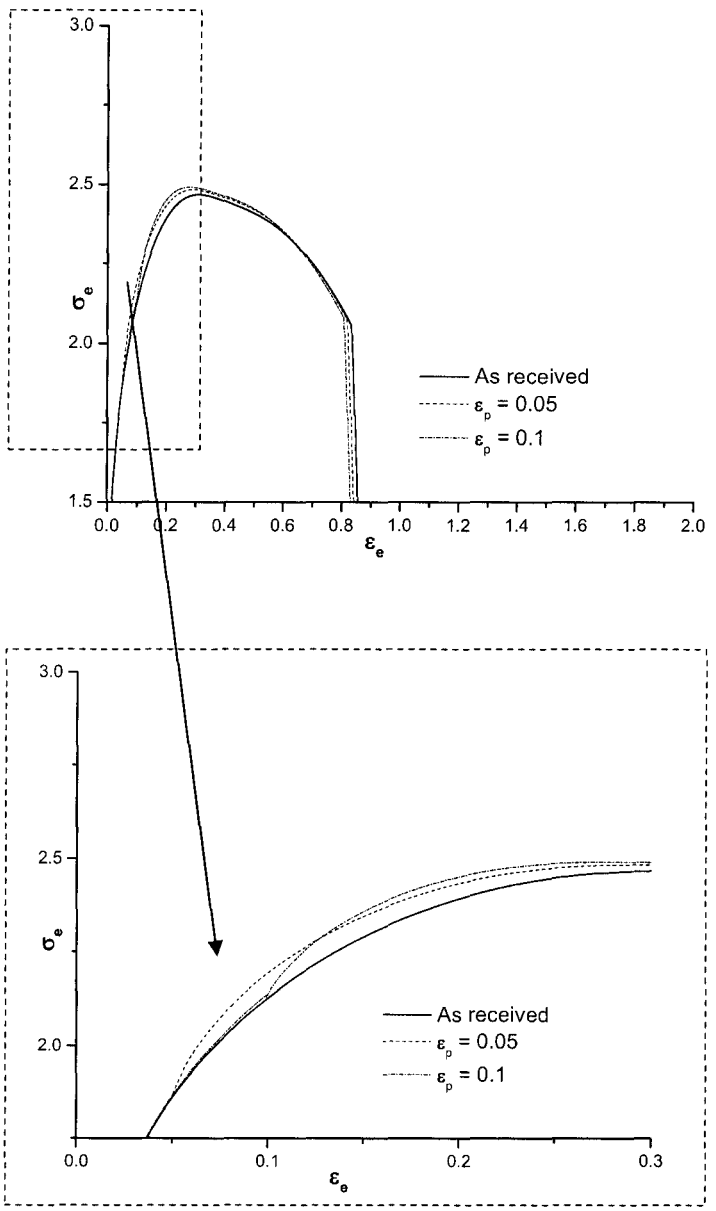

Figure 4.3c: Calculated effective stress vs. effective strain curves for equi-biaxial stretching after the sheet has been pre-strained to different levels of uniaxial stretching *(ρ=-0.5)*.

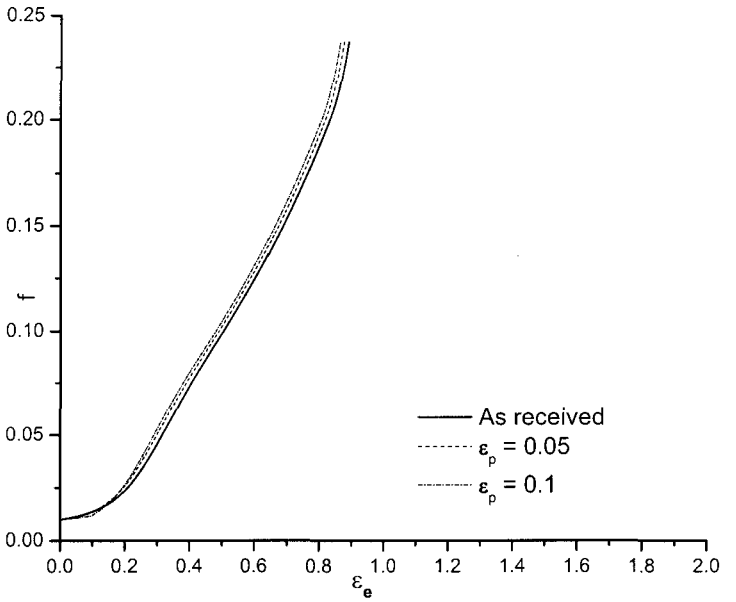

Figure 4.3d : Calculated f vs. ε_e curves for equi-biaxial stretching after the sheet has been pre-strained to different levels of uniaxial stretching *(ρ=-0.5)*.

4.3.5 Effect of Uniaxial Pre-strain on In-plane Plane Strain Tension

The effect of uniaxial pre-straining *(ρ=-0.5)* at different levels *(ε_p=0.05, 0.1)* on in-plane plane strain tension is observed in Figure 4.5. The curves are compared with the monotonic in-plane plane strain tension curve (as received). Figure 4.5a shows the stress-strain $(\sigma_{11} - \varepsilon_{11})$ response of the imposed deformation. From this figure it can be explained that uniaxial stretching has a much lower hardening rate than in-plane plane strain tension. At larger strains $(\varepsilon_{11} > 0.4)$ an increase in flow stress due to the pre-strain is observed. Figure 4.5b shows the evolution of void volume fraction f, with the imposed deformation. It is observed that due to a uniaxial pre-strain (CASE #4), f

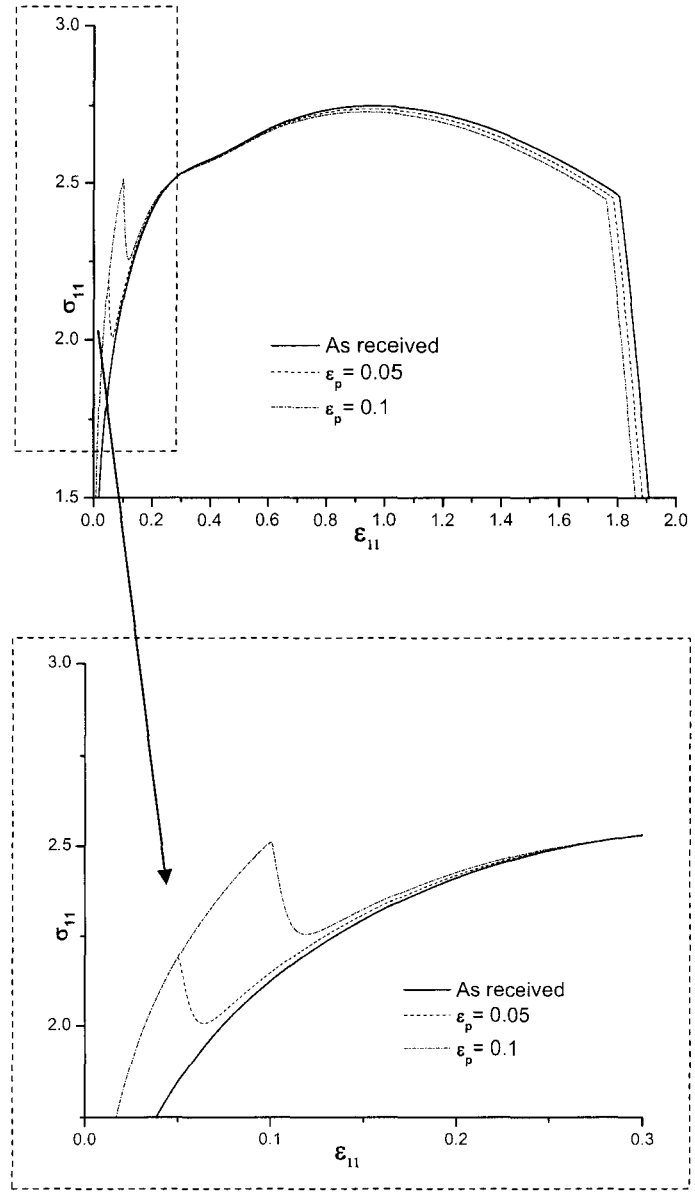

Figure 4.4a: Calculated σ_{11} vs. ε_{11} curves for uniaxial stretching after the sheet has been pre-strained to different levels of in-plane plane strain tension *(ρ=0)*.

reaches the fracture point at a slightly higher strain than the monotonic equi-biaxial loading. This implies that if a sheet material is pre-strained uniaxially (CASE#4) it increases the strength of the material due to the delay of damage than when compared to a single monotonic in-plane plane strain tension loading.

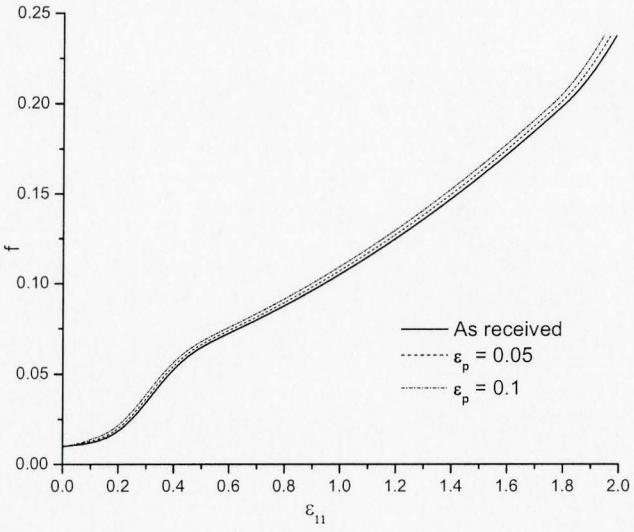

Figure 4.4b Calculated f vs. ε_{11} curves for uniaxial stretching after the sheet has been pre-strained to different levels of in-plane plane strain tension *(ρ=0)*

4.3.6 Effect of an In-plane Plane Strain Pre-strain on Equi-biaxial Stretching

Figure 4.6 shows the curves obtained under equi-biaxial stretching $(\rho = 1)$ after pre-strained under in-plane plane strain tension $(\rho = 0)$ to different levels *(ε_p=0.05 0.1)*. The curves are compared to the monotonic equi-biaxial stretching curve (as received). Figure 4.6a shows the stress-strain $(\sigma_{11} - \varepsilon_{11})$ response of the imposed deformation. As shown in figure 4.1a, the hardening rate in in-plane plane strain tension is much higher than that in equi-biaxial stretching. When the strain path is changed from in-plane plane strain tension to equi-biaxial tension, an abrupt drop in hardening rate is observed. With further deformation $(\varepsilon_{11} > 0.2)$, the pre-strain results in an increase of the flow stress.

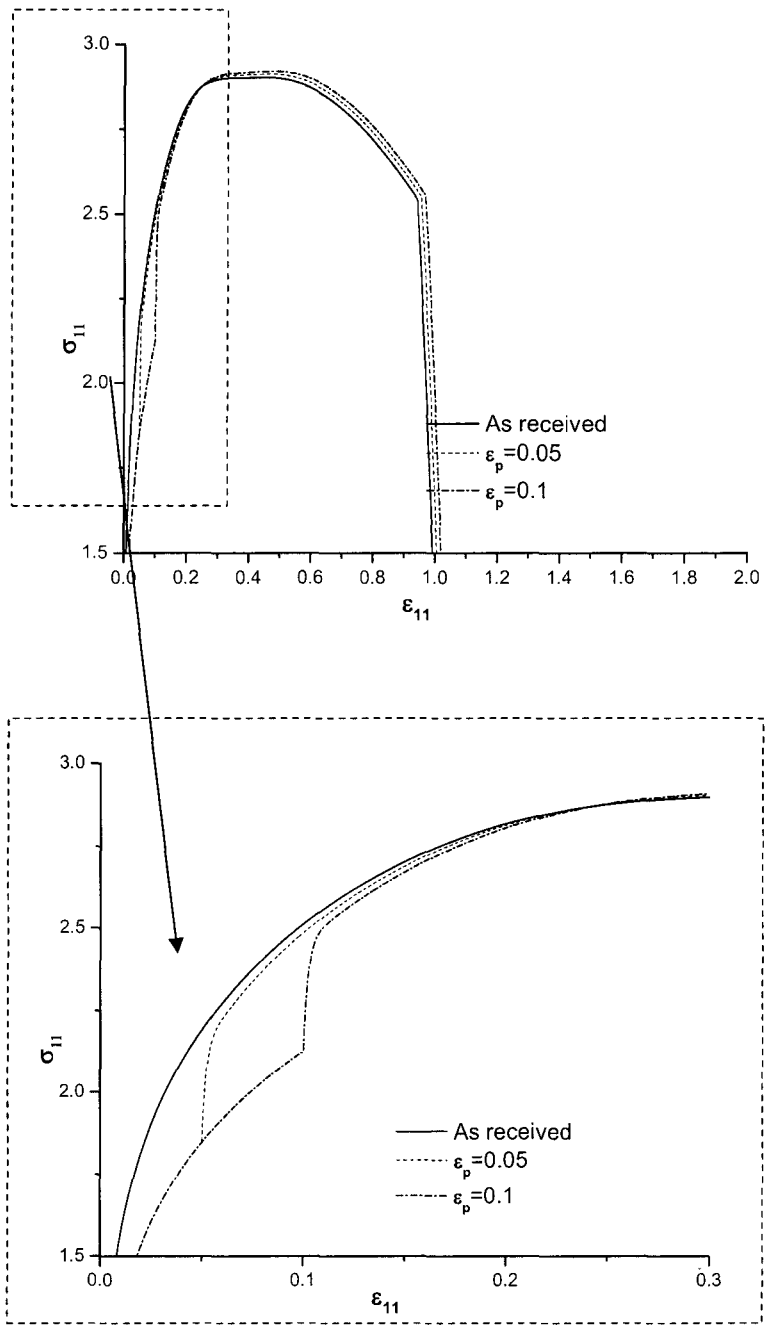

Figure 4.5a : Calculated σ_{11} vs. ε_{11} curves for in-plane plane strain tension after the sheet has been pre-strained to different levels of uniaxial stretching *(ρ=-0.5)*.

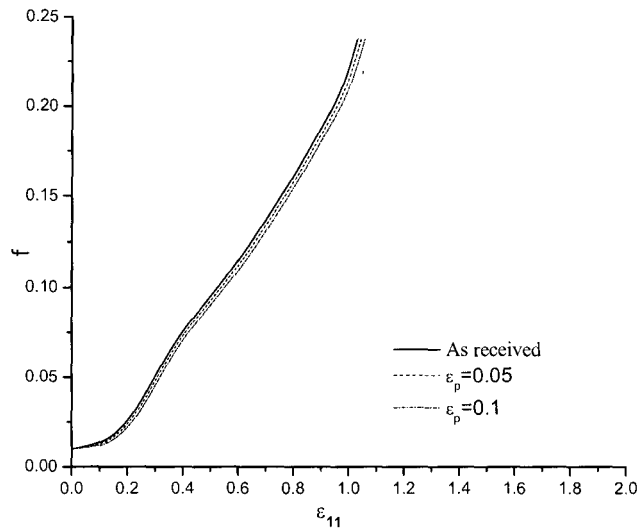

Figure 4.5b : Calculated f vs. ε_{11} curves for in-plane plane strain tension after the sheet has been pre-strained to different levels of uniaxial stretching *(ρ=-0.5)*.

Figure 4.6a shows that the material fails at a slightly higher strain ε_{11}, when pre-strained under in-plane plane strain tension when subjected solely to a monotonic equi-biaxial stretch. This phenomenon can be described with Figure 4.6b which shows the evolution of void volume fraction f, when the material is subjected to CASE #5. The curves are compared with the monotonic equi-biaxial stretching curve. Due to pre-straining, f reaches the fracture point at a slightly higher strain than that reported from the monotonic equi-biaxial stretching curve. These results indicate that if a sheet material is pre-strained under in-plane plane strain tension and then loaded in equi-biaxial stretching (CASE #5), the material is strengthened due to the slow rate of damage formation (void volume fraction) when compared to a monotonic equi-biaxial stretch.

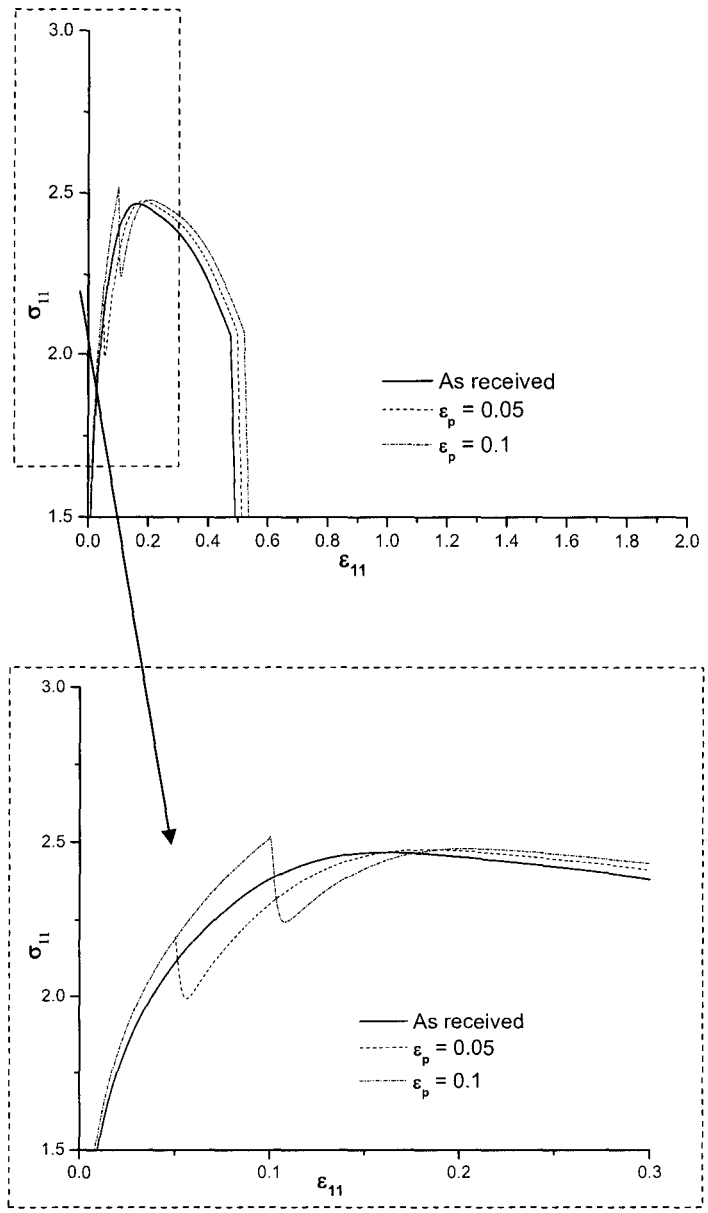

Figure 4.6a: Calculated σ_{11} vs. ε_{11} curves for equi-biaxial stretching after the sheet has been pre-strained to different levels of in-plane plane strain tension *(ρ=0)*.

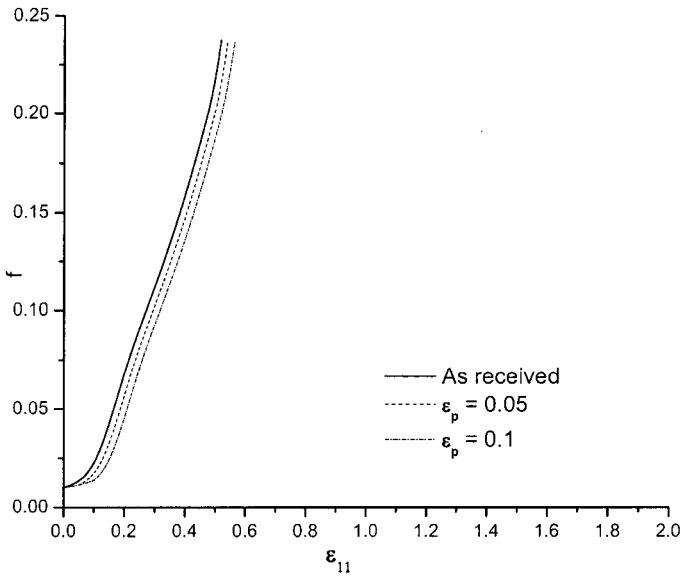

Figure 4.6b : Calculated f vs. ε_{11} curves for equi-biaxial stretching after the sheet has been pre-strained to different levels of in-plane plane strain tension *(ρ=0)*.

4.3.7 Effect of Equi-biaxial Pre-Strain on In-Plane Plane Strain Tension

Figure 4.7 shows the curves obtained under in-plane plane strain tension $(\rho = 0)$ after pre-straining equi-biaxially (CASE #6) $(\rho = 1)$ to different levels *(ε_p=0.05, 0.1)*. The curves are compared to the monotonic in-plane plane strain tension curve (as received). Under monotonic loadings, work-hardening rate under equi-biaxial stretching is lower than that under in-plane plane strain tension (see Figure 4.1a). When the strain path is changed from equi-biaxial tension to in-plane plane strain tension to equi-biaxial tension, an abrupt increase in hardening rate is observed. With further deformation $(\varepsilon_{11} > 0.3)$, the pre-strain results in a decrease of the flow stress (Figure 4.7a).

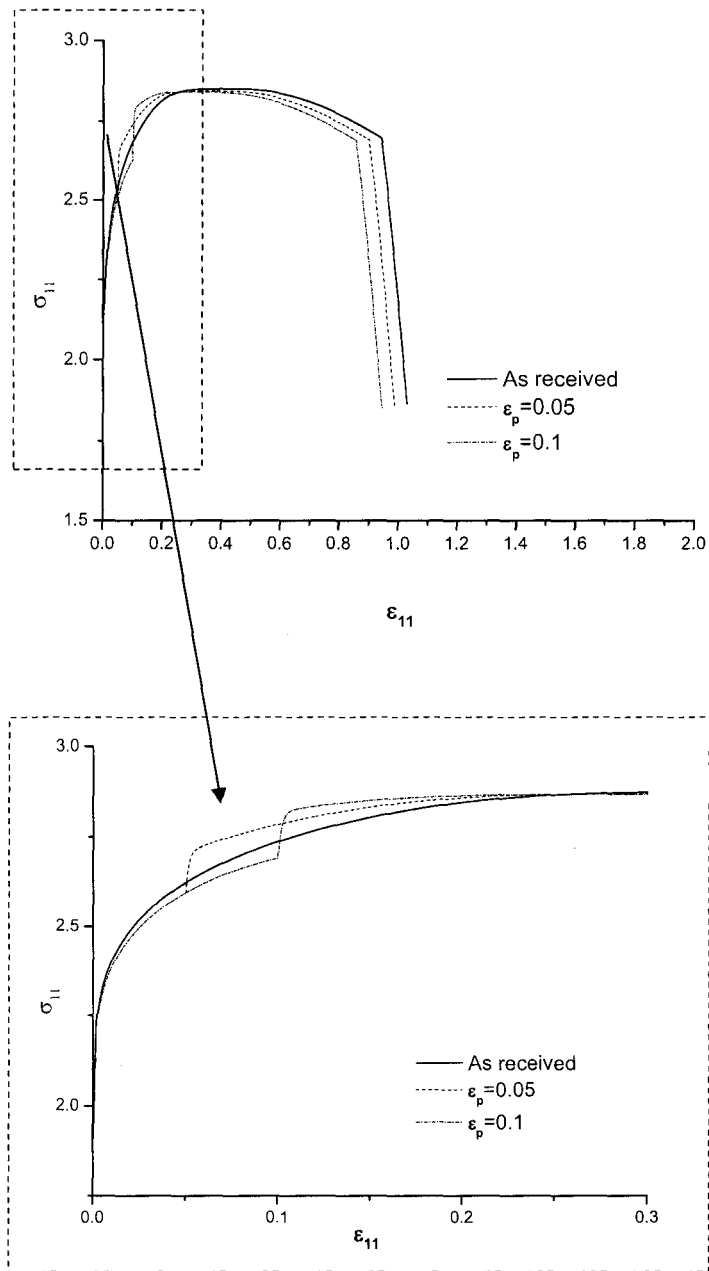

Figure 4.7a: Calculated σ_{11} vs. ε_{11} curves for in-plane plane strain tension after the sheet has been pre-strained to different levels of equi-biaxial stretching *(ρ=1)*.

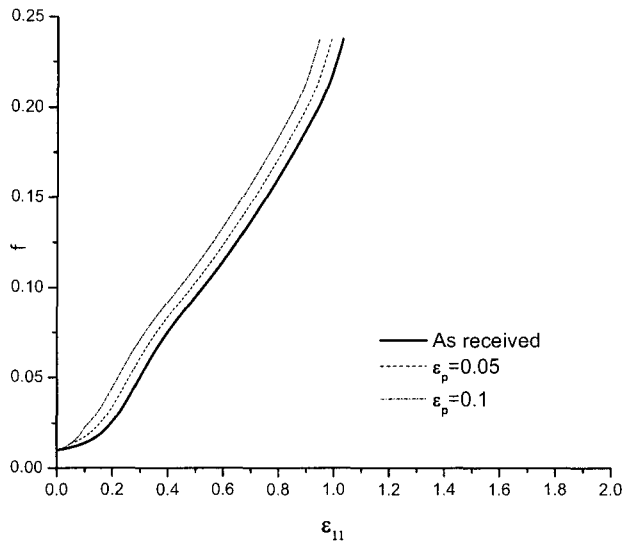

Figure 4.7b: Calculated f vs. ε_{11} curves for in-plane plane strain tension after the sheet has been pre-strained to different levels of equi-biaxial stretching *(ρ=1)*.

Figure 4.7a also shows that the material fails at an earlier strain ε_{11}, when pre-strained equi-biaxially than when solely subjected to a monotonic in-plane plane strain tension load. This phenomenon can be explained using Figure 4.7b which shows the evolution of void volume fraction f. with the imposed deformation. In this figure the evolution of f subjected to a CASE #6 loading is compared with a monotonic in-plane plane strain tension load. Due to the pre-straining, f reaches the fracture point at a smaller strain than that observed in the monotonic in-plane plane strain tension condition.

These results imply that if a sheet material is pre-strained equi-biaxially and then loaded under in-plane plane strain tension (CASE #6), it is weakened when compared to in-plane plane strain tension. This weakening is attributed to the increase of damage formation (void volume fraction).

CHAPTER 5

EFFECTS OF MATERIAL PROPERTIES AND STRAIN PATH CHANGE ON FORMING LIMIT DIAGRAMS

5.1 Introduction

The purpose of a forming limit diagram (FLD) is to define a safe forming region such that when operating in this region, small changes in material and forming process conditions will not cause failure. The main objective of processing sheet metal is to ensure that the strain does not reach the limits of the safe forming region. Therefore, it is important to develop a numerical tool that can accurately predict the changes in a forming limit curve in response to the changes in material and process properties.

In this Chapter, the dependence of mechanical properties and strain path change on sheet metal formability is investigated. All the simulations are based on the Gurson damage model and the M-K approach described in Chapter 3.

5.2 Typical Material

The present simulations were carried out for a typical material matrix specified by: H_b/H_a=1.0, q_1=1.5, q_2 =1.0, σ_0 =1, $\varepsilon_0 = \sigma_0/E$= 0.002, ν = 0.3, f_0 = 0.01, n= 0.2 and m= 0.01. Void nucleation is assumed to be strain controlled with f_n = 0.04, nucleating around a plastic strain of ε_n = 0.3 with a standard deviation of S_n = 0.1 at outside the band (homogeneous material). For inside the band (inside the groove), f_n = 0.05 thus, Δf_n = 0.01, and all other parameters are the same as in the material outside the band. The void coalescence effect is included using f_c= 0.2 and f_f = 0.25. Unless otherwise mentioned, these values of the geometrical and mechanical parameters will be

used in all the simulations in Chapter 5. It should be also noted that in the simulations we have scanned every 5 degrees of a range of ψ and then determined the critical groove angle that gives the minimum localization strain, i.e. the limit strain.

5.3 Effect of Geometric Imperfection *(H_b/Ha)*

The geometric imperfection has been expressed in terms of a reduction in thickness, but there are other imperfections possible such as inclusions, texture variations, and surface roughness [Needleman and Trintafyllidis, 1978]. Figure 5.1(a) shows the effects of initial imperfection on the predicted FLDs for the material described in Section 5.2. As expected, the smaller the initial imperfection ($1\text{-}H_b/H_a$), the larger the critical strain for sheet necking. The effect of the initial geometric imperfection on the void volume fraction is shown in Figure 5.1(b). Here, only equi-biaxial tension (ρ= 1.0) is considered since the highest imperfection sensitivity is observed under this strain path [Needleman and Tvergaard; 1984]. It is found that the void volume fraction increases more rapidly in cases with larger imperfections.

5.4 Effect of Material Properties

5.4.1 Effect of Strain Rate Sensitivity *(m)*

The effect of the strain rate sensitivity on localized necking has been studied by various researchers [Hutchinson and Neale, 1978; Needleman and Tvergaard, 1984; Wu *et al.,* 1997]. It has been generally accepted that Strain rate sensitivity has a significant effect on localized necking. Figure 5.2 shows the change in the predicted FLD when the value of the material rate sensitivity m is increased by a factor 10 to m = 0.01 and by a factor 20 to m=0.02. Increasing the rate sensitivity in (3.7) tends to enhance the hardening at large strains. Consistent with this, we

see from figure 5.2 that necking retardation is observed for the whole range of ρ as the rate sensitivity m is increased.

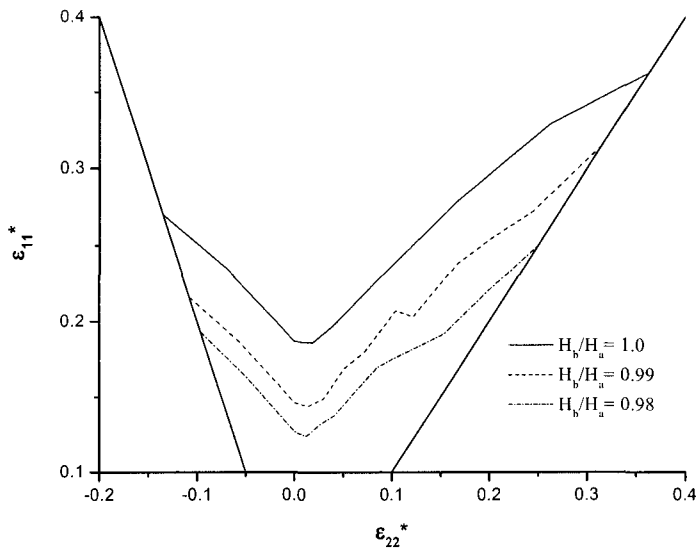

(a)

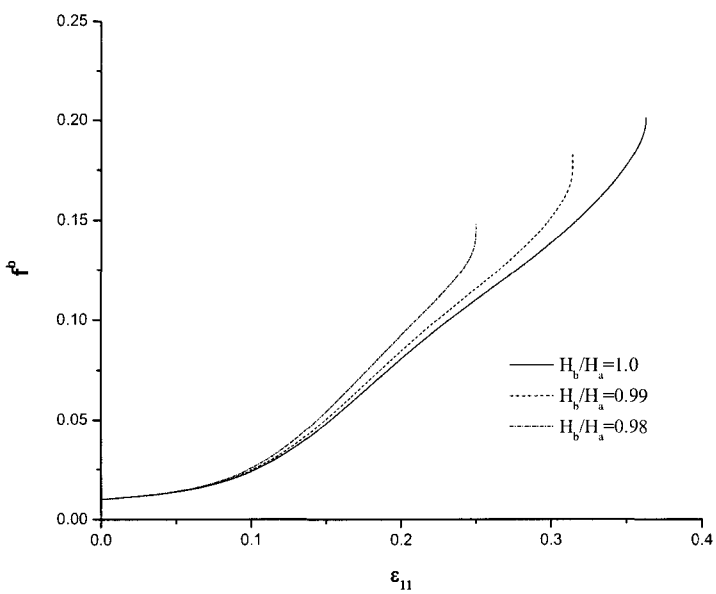

(b)

Figure 5.1: Effect of initial geometric imperfection on (a) the predicted FLDs, and (b) void volume fraction inside the band (f^B) at ρ=1.

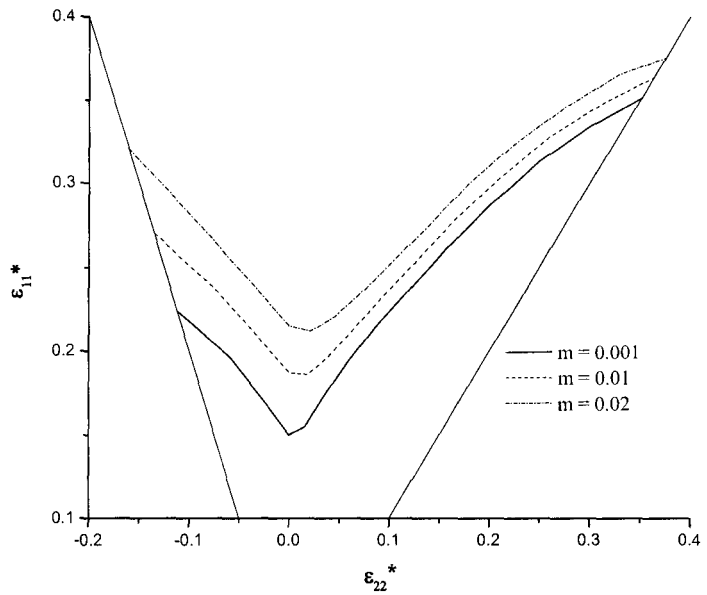

Figure 5.2: Effect of strain rate sensitivity on the predicted FLDs.

5.4.2 Effect of Strain Hardening Exponent *(n)*

The effect of the strain hardening exponent on the FLD has been studied extensively [see e.g. Hutchinson and Neale, 1978; Needleman and Triantafyllidis, 1978; Wu *et al.*, 1997]. The parameters n govern the strain hardening through the power-law expression $g(\bar{\varepsilon}) = \sigma_0\left(\bar{\varepsilon}/\varepsilon_0 + 1\right)^n$ (3.8). Figure 5.3(a) shows the predicted FLDs for various hardening values n=0.2, 0.3, and 0.4. It is clearly seen that a larger value of n increases the limit strain, which can be attributed simply to the fact that hardening increases with increasing n. The effect of hardening on the void volume fraction inside the band for equi-biaxial tension (ρ=*1*) is observed in Figure 5.3(b). For the material with the highest hardening material (n=0.4), the void volume fraction reaches f_f before localized necking occurs.

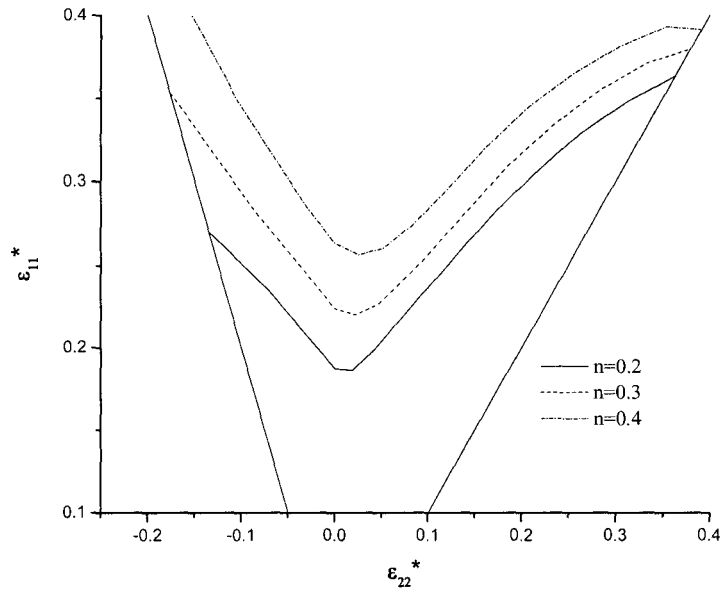

(a)

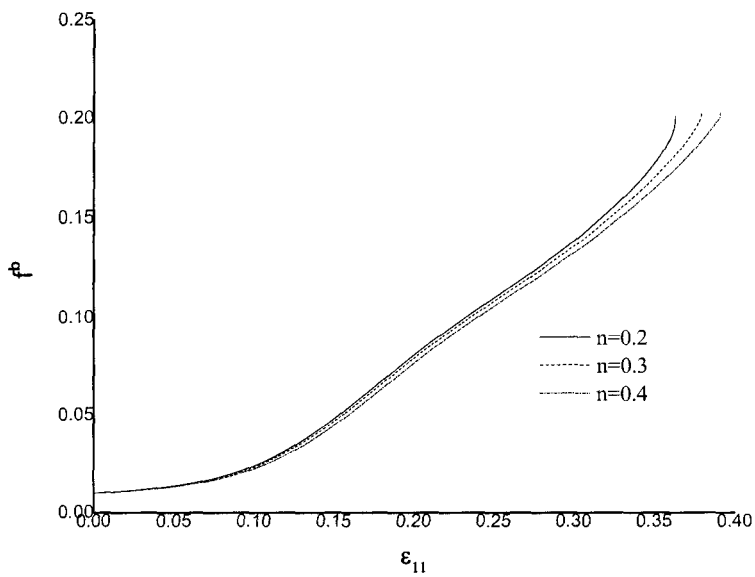

(b)

Figure 5.3: Effect of hardening on (a) the predicted FLDs, and (b) void volume fraction inside the band (f^B) at ρ=1.

5.4.3 Effect of Groove Angle *(ψ)*

As mentioned previously, in the simulations we have scanned every 5 of a range of ψ and then determined the critical groove angle that gives the minimum localization strain, i.e. the limit strain. For the materials considered in this study, It is found that a groove oriented at $\psi = 0$ is favorable for necking when $0 \leq \rho \leq 1$, while the critical groove orientation increases from 0 at $\rho = 0$ to 25^0 at uniaxial tension ($\rho = -0.5$). This effect of groove orientation can be also observed in Figure 5.4, where cases with groove orientations restricted to $\psi = 0$ are also included. It is noted that the effect of groove orientation on FLDs was carried out in Figure 5.4 for materials with different strain rate sensitivities (m=0.001, 0.01 and 0.02).

5.4.4 Effect of Elastic Modulus (*E*)

The effect of the modulus of elasticity has been considered in the crystal plasticity based FLD analysis carried out by Wu *et al.*, [1997]. They found that elasticity has a significant effect on the limit strains near the in-plane plane strains condition $(\rho \approx 0)$. In the present study, however, there was no significant effect of the modulus of elasticity on the prediction of the forming limit diagram.

5.5 Effect of Initial Void Volume Fraction

Initial void volume fraction has a significant effect on formability for the strain paths near equi-biaxial tension ($\rho \approx 1$). This effect is shown in figure 5.5(a) where the initial void volume fraction is varied as 0.01, 0.03, and 0.05. Limit strain is highest near the equi-biaxial tension condition for lower void volume fractions (f_0=*0.01*) and decreased as the void volume fraction

increased. In Figure 5.5(b) the effect of initial void volume fractions (f_0) on the development of the void volume fraction for the equi-biaxial tension condition ($\rho=1$) is observed. When a high initial void volume fraction is considered the FLD attains the maximum void volume fraction at a lower strain (ε_{11}= 0.25) compared to the other two conditions. Because the initial void volume fraction is higher it reaches void coalescence (f_c=0.15) earlier than the other two conditions. As a result, necking occurs at an earlier stage than other two conditions for a strain ratio near unity.

5.6 Effect of Void Nucleation

To study the effect of void nucleation the material imperfection is selected as a thickness imperfection such that $H_b/Ha=0.99$, rather than the difference in void nucleation as described in Section 5.2. This is to avoid the scenario of not being able to reach necking for the no nucleation condition. In Figure 5.6(a) the effect of void nucleation on the forming limit curve is observed. Obviously, for strain controlled void nucleation necking occurs earlier in the case with void nucleation than in the case of without void nucleation. In the no nucleation condition, the void volume fraction is increased solely by void growth, whereas for strain controlled nucleation, both nucleation and void growth contribute to increase of the void volume faction. The void volume fraction reaches its maximum for strain controlled nucleation at a much early strain. This acceleration of void growth is observed in Figure 5.6(b), where the effect of void nucleation on the void volume fraction inside the band for $\rho=1$ is shown. With a void nucleation, the void volume fraction reaches its maximum at a lower strain value (ε_{11}= 0.32) compared to the no nucleation condition (ε_{11}= 0.55).

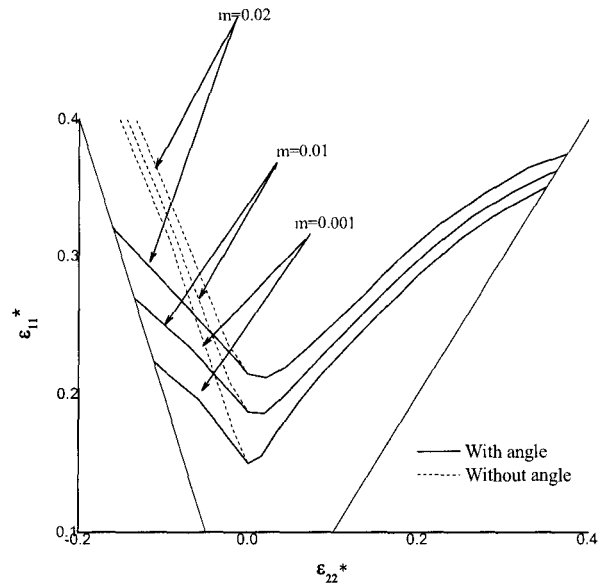

Figure 5.4: Effect of initial groove angle (ψ) on the predicted FLDs.

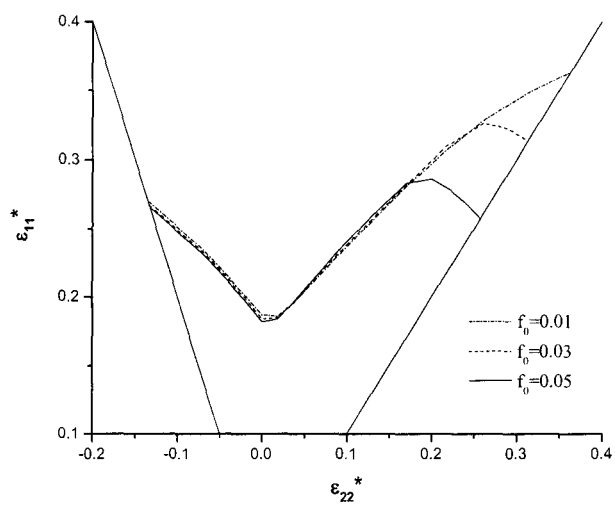

(a)

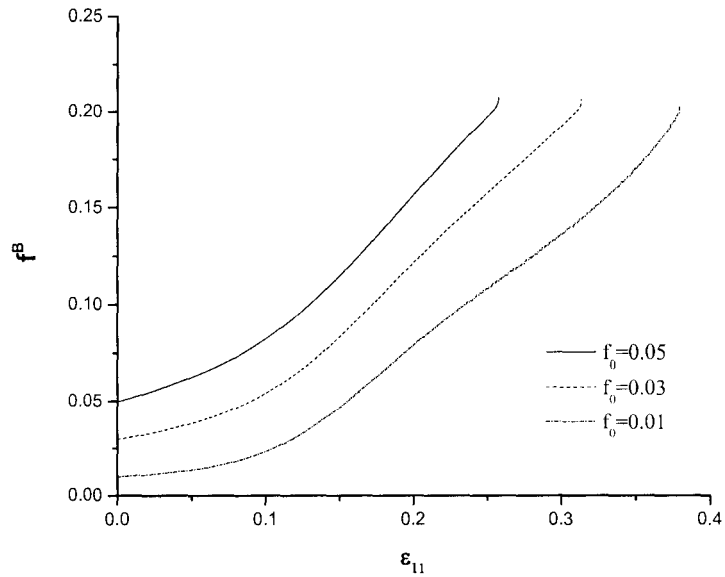

(b)

Figure 5.5: Effect of initial void volume fraction on (a) the predicted FLDs, and (b) void volume fraction inside the band (f^B) at ρ=1.

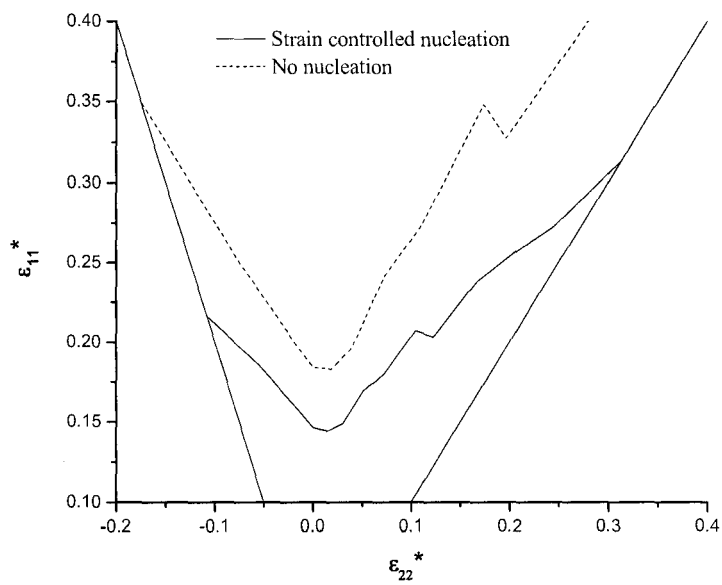

(a)

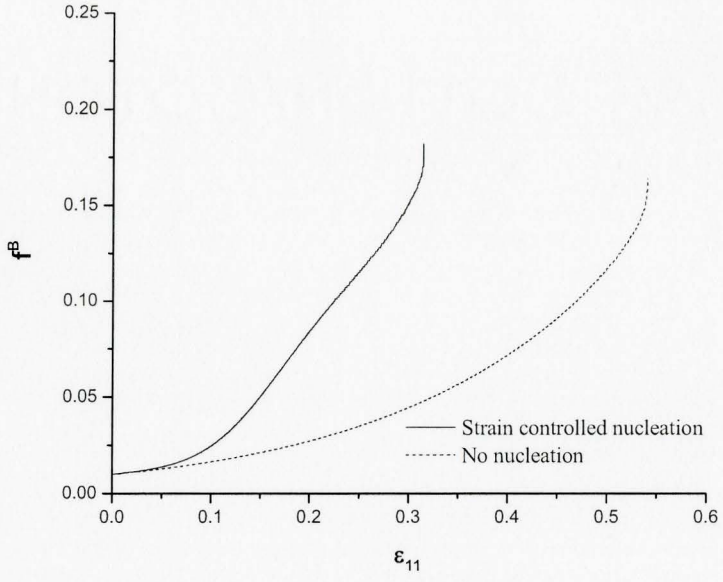

(b)

Figure 5.6: Effect of void nucleation on (a) the predicted FLDs, and (b) void volume fraction inside the band (f^B) at ρ=1, with an initial geometric in-homogeneity, $H_b/Ha=0.99$

5.6.1 Effect of Void Volume Fraction of Nucleating Particles (f_n)

Figure 5 7(a) displays the effect of additional volume fraction of void nucleating particles inside the band (Δf_n)on the forming limit diagram. This effect has been studied previously in the literature [Needleman and Tvergaard, 1984] Here, the material is the same material described in Section 5.2, and Δf_n takes on various values: 0.0001, 0.001, 0.01, and 0.05 In all cases the void coalescence effect is included. It is observed that the shape of the FLD is sensitive to Δf_n As expected, the smaller the Δf_n, the larger the critical strain for sheet necking. It is important to note that in the cases with Δf_n=0.001 and 0.0001, ductile fracture occurs before localized necking is detected for the strain paths near the equi-biaxial tension ($\rho \approx 1$).

5.6.2 Effect of Void Nucleation Strain (ε_n)

In the typical material (Section 5.2) void nucleation is controlled by strain. Nucleation strain ε_n is defined as the strain at which void nucleation starts to occur. In Figure 5.8 (a) the effect of the nucleation strain on the forming limit diagram is displayed.

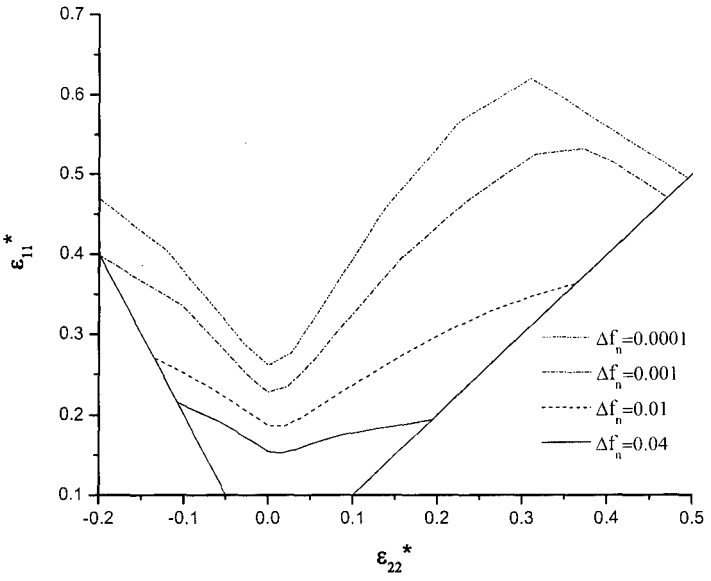

Figure 5.7: Effect of void volume fraction of nucleating particles (Δf_n) on the predicted FLDs.

It is found that the predicted forming limit curve moves upward with increasing the nucleation strain. When the nucleation strain is lower ($\varepsilon_n=0.1$) void nucleation starts at an earlier stage compared to the other two nucleation strain values. As void nucleation quickens it causes the necking to occur earlier. Similar observations were made by Chu and Needleman [1979] and Saje *et al.* [1980]. In Figure 5.8 (b) the effect of the void nucleation strain on the void volume fraction inside the band for $\rho=1$ is observed. As expected, the void volume fraction increases much faster in a material with a lower nucleation strain than in a material with a higher nucleation strain.

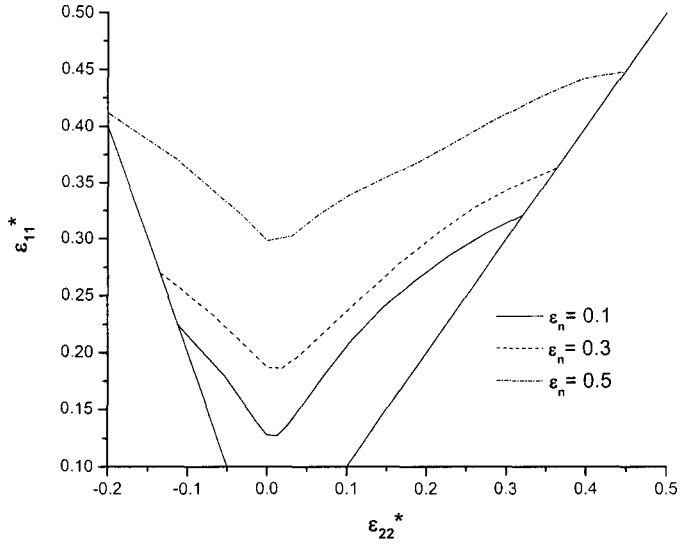

(a)

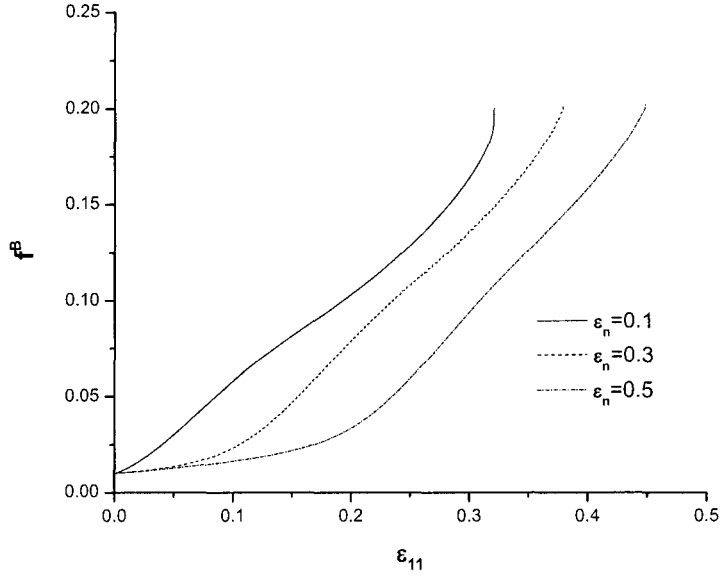

(b)

Figure 5.8: Effect of void nucleation strain on (a) the predicted forming limit, and (b) void volume fraction inside the band (f^B) at ρ=1.

5.6.3 Effect of Standard Deviation (S_n)

In this study nucleation is assumed to be strain controlled, and S_n is the standard deviation of the normal distribution curve of void nucleation. In figure 5.9 the effect of standard deviation on the forming limit curve is displayed. All the other material properties are same as in Section 5.2, and values assumed for the standard deviation are: 0.09, 0.1, and 0.2. From Figure 5.9 it can be observed that the standard deviation has an insignificant effect on the limit strains except for the strain paths near the equi-biaxial stretching ($\rho \approx 1$), where the predicted limit strain is found to be very sensitive to mechanical properties of the material.

5.7 Effect of Void Coalescence (f_c)

The void coalescence, proposed by Tvergaard [1982], is described in (3.25) and (3.26). The effect of void coalescence on FLDs is studied in Figure 5.10(a), where different coalescence strains $f_c = 0.1, 0.15$ and 0.2 are considered. It is observed that the smaller the void coalescence strain f_c, the smaller the critical strain for sheet necking. It is also found that the effect of coalescence is most effective near $\rho \approx 1$. In Figure 5.10(b) the effect of void coalescence on the void volume fraction inside the band for $\rho=1$ is observed. For a higher void coalescence strain, the void volume fraction reaches its maximum at a higher strain. This phenomenon was also observed by other researchers [see e.g. Needleman and Tvergaard, 1984].

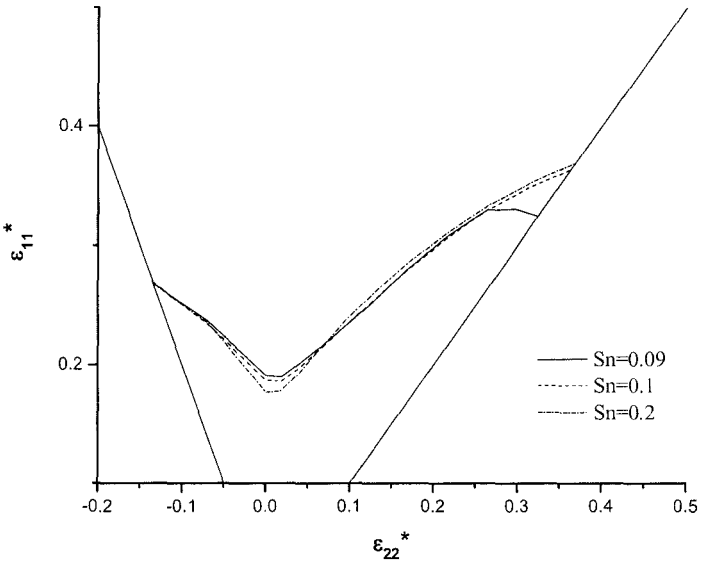

Figure 5.9: Effect of standard deviation (S_n) on the predicted FLDs.

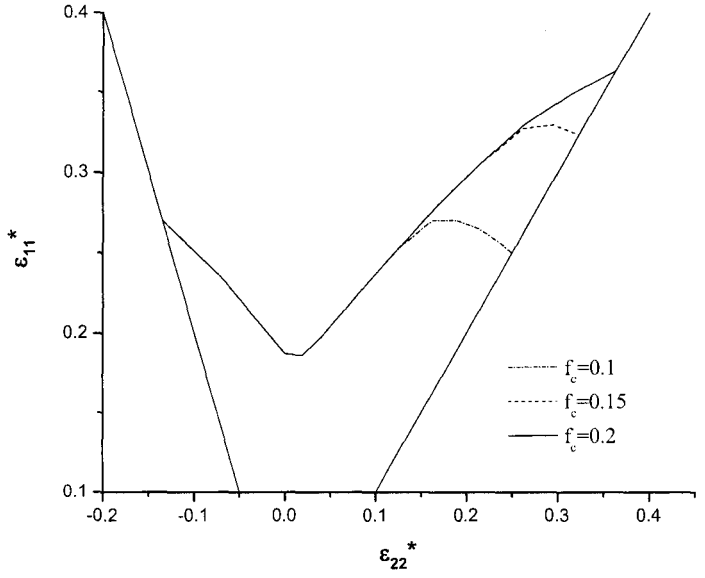

(a)

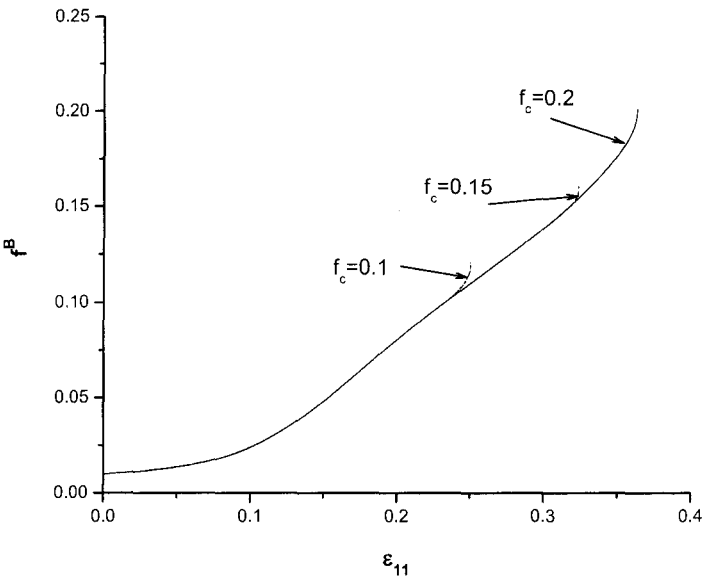

(b)

Figure 5.10: Effect of void coalescence on (a) the predicted FLDs, and (b) void volume fraction inside the band (f^B) at ρ=1.

5.8 Effect of Strain Path Changes On Forming limit Diagram

From literatures, changes in deformation modes have been observed in parts of a material undergoing a forming operation [see e.g. Graf and Hosford, 1993; Brunet and Morestin, 1998]. In a single process such changes may be gradual but for multiple processes abrupt changes are often expected. It has been observed from various studies that changing the strain path can increase or decrease the limit strain [see e.g. Nakazima *et al.*, 1968; Laukonis and Ghosh, 1978; Needleman and Tvergaard, 1984; Graf and Hosford, 1993].

In this chapter, the effect of strain path change on FLDs is numerically studied, based on different non-proportional loading histories, which are combinations of two linear strain paths. The first strain path, the pre-strain operation, is common to all loading histories. Subsequent

linear deformation paths are imposed by varying the strain-rate ratio for the development of an FLD applicable to that given pre-strain path and amount. In the present study we consider three pre-strain conditions, namely uniaxial tension (ρ=-0.5), in-plane plane strain tension (ρ=0), and equi-biaxial tension (ρ=1.0).

5.8.1 Predicted Forming Limit Diagram Pre-strained with Uniaxial Stretching *(ρ= -0.5)*

For studying the effect of uniaxial tension on the limit strain, the material is first strained to a level of ε_p and then another linear strain path is applied (ρ=constant) until the necking criterion is reached. In this way the whole FLD is determined by taking all the limit strain points for all strain ratios ($-0.5 \geq \rho \leq 1$).

Figure 5.11 describes the predicted FLDs when the sheet is pre-strained to different levels *(ε_p =0.05* and *0.01)* in uniaxial stretching. From the figure it is observed that the forming limit diagram is moved left and upward compared to the as received sheet. More specifically, pre-straining slightly increases the major limit strain ε_{11} for in-plane plane strain tension, but significantly enhances the limit strain ε_{11} for equi-biaxial stretching. This observation is in good agreement with other researchers [Graf and Hosford, 1993; Wu *et al.,* 1998].

5.8.2 Predicted Forming Limit Diagram After an In-plane Plane Strain Tensile Pre-strain *(ρ= 0)*

The effect in-plane plane strain tension *(ρ=0)* on the predicted limit strains of sheet metal is studied by first pre-strain to different levels (ε_p=*0.05* and *0.1)* in in-plane plane strain tension and then apply another linear strain path *(ρ=constant)* until the necking criterion is reached. In this way the whole FLD is determined by taking all the limit strain points for all strain ratios (-

$0.5 \geq \rho \leq 1$). Figure 5.12 describes the predicted forming limit diagram when the sheet is pre-strained to different levels (ε_p =0.05 and 0.01) in in-plane plane strain tension. As expected, the limit strain for in-plane plane strain tension is not affected by the pre-straining. The FLD shape changes from U towards V due to the pre-straining. For uniaxial stretching, it is found that the pre-straining has almost no effect on the limit strain ε_{11}, but it dramatically decreases the limit

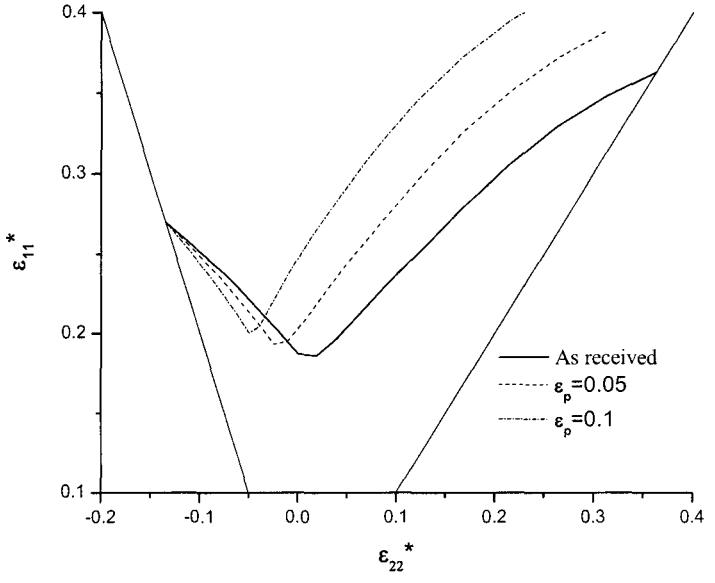

Figure 5.11: Predicted FLDs when the sheet is pre-strained to different levels *(ε_p =0.05* and *0.01)* in uniaxial stretching (ρ=-0.5).

strain ε_{22}. For equi-biaxial tension, the pre-straining significantly increases the limit strain ε_{11} but decreases the limit strain ε_{22}. This observation is also in a good agreement with other researchers [Graf and Hosford, 1993; Wu *et al.,* 1998].

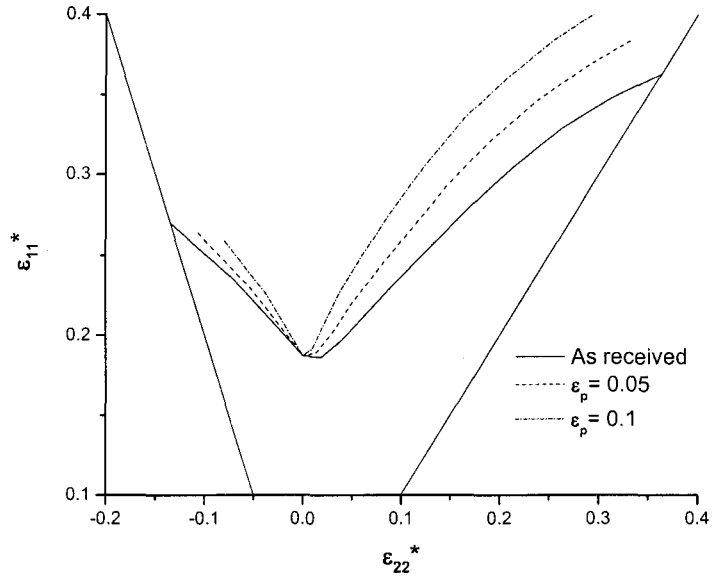

Figure 5.12: Predicted FLDs when the sheet is pre-strained to different levels *(ε_p =0.05* and *0.01)* along the in-plane plane strain tension (ρ=0).

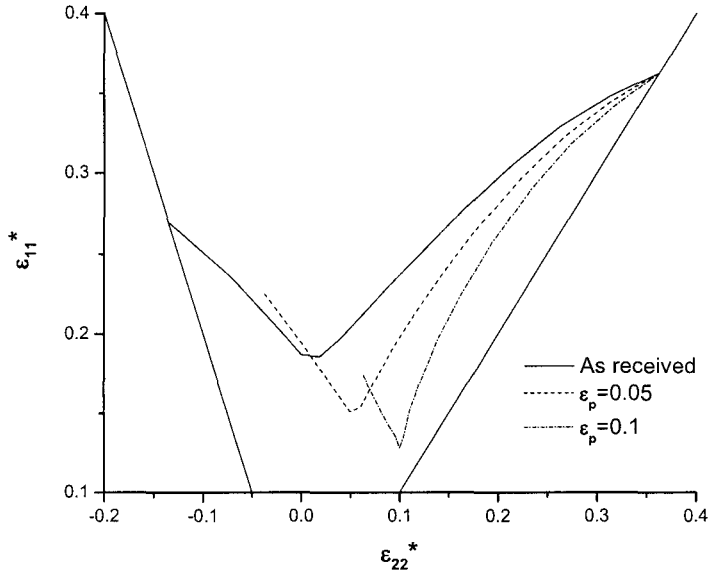

Figure 5.13: Predicted FLDs when the sheet is pre-strained to different levels *(ε_p =0.05* and *0.01)* in equi-biaxial stretching *(ρ=1)*.

5.8.3 Predicted Forming Limit Diagram After an Equi-biaxial Tensile Pre-strain*(ρ= 1)*

For studying the effect of equi-biaxial stretching on the limit strains, the sheet is first strained to ε_p=0.05 and 0.1, respectively, and then another linear strain path is applied *(ρ=constant)* and taken up to the necking criterion. In this way, the whole FLD is determined by taking all the limit strain points for all strain ratios $(-0.5 \geq \rho \leq 1)$.

Figure 5.13 gives the predicted FLDs when the sheet is pre-strained to different levels $(\varepsilon_p = 0.05$ and $0.01)$ in equi-biaxial stretching. It is clearly observed that the forming limit diagram shifts right and downward in relation to the as received sheet. The limit strain is reduced for both the in-plane plane strain and equi-biaxial strain conditions. It can be said that equi-biaxial pre-straining decreases the formability of sheet metal with respect to subsequent proportional loading conditions. Similar conclusions have been made by Graf and Hosford [1993], Wu *et al.* [1998] and Alsos *et al.* [2008].

5.9 Effect of Strain Path Change on the Forming Limit Stress Diagram (FLSD)

As demonstrated previously, FLDs are very sensitive to strain path changes. There is no single curve in strain space that represents the forming limit, and this limits the use of conventional FLDs for assessing forming severity because the straining path of material elements in a real sheet metal forming process is usually not known with any certainty. Therefore, finding a single path-independent curve to characterize forming limits is of considerable practical interest. It has been confirmed that the Forming Limit Stress Diagram (FLSD), developed by Arrieux et al. [1982] and others, is almost independent of strain path. Its utility has been promoted as the solution to the analysis of multi-stage forming processes.

In this section, the stress-based forming limit diagram under linear and complex strain paths is constructed. The simulations are carried out based on the M-K and Gurson model. A comparison between the concept of strain-based forming limits and stress-based forming limits is presented. Up to this point, all the FLDs were constructed in strain space with ε_{11}^{*} and ε_{22}^{*} representing the major and minor limit principal strains, respectively. In using FLSDs, the major and minor principal stresses σ_{11}^{*} and σ_{22}^{*} outside the band at necking are used to represent the forming limits.

Similar to the analysis of FLDs earlier, a two stage strain path is used to construct FLSDs. The first stage is the pre-strain, followed by the second stage, a reloading in another strain path. This is done for all the strain ratios from -0.5 to 1 (i.e. from uniaxial tension through in-plane plane strain tension to equi-biaxial stretching).

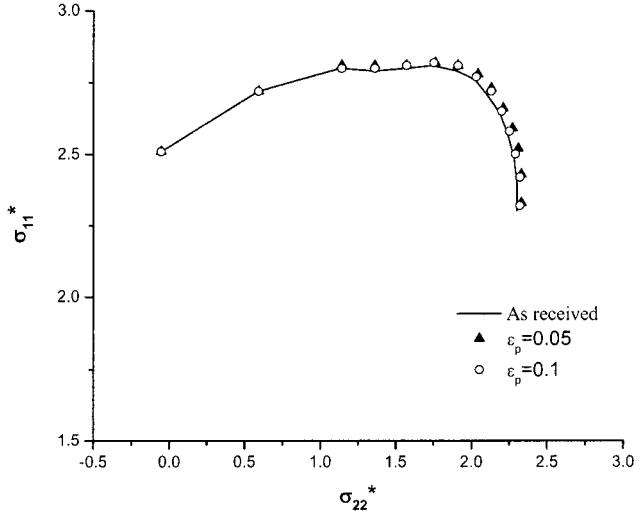

Figure 5.14: Predicted FLSDs when the sheet is pre-strained to different levels *(ε_p =0.05* and *0.01)* in uniaxial stretching (ρ=-0.5).

The effect of uniaxial stretching on the FLSD is studied in Figure 5.14 which corresponds to the strain based FLD in Figure 5.11. In both figures, the as received material properties and the necking condition are the same. It can be seen that pre-straining in uniaxial stretching (ε_p=0.05, 1.0) does not affect the FLSD diagram much.

The effect of in-plane plane strain tension on the FLSD is shown in Figure 5.15 which corresponds to the strain based FLD in Figure 5.12. Again, it is observed that the in-plane plane strain tension pre-straining has no significant effect on FLSDs.

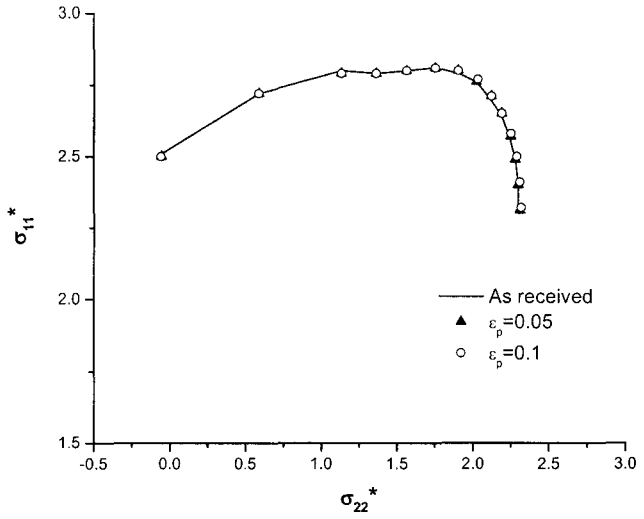

Figure 5.15: Predicted forming limit stress diagram when the sheet is pre-strained to different levels *(ε_p =0.05* and *0.01)* of in-plane plane strain tension (ρ=0).

Finally, the effect of equi-biaxial stretching pre-strain on FLSDs is shown in Figure 5.16, which corresponds to Figure 4.13 if results are presented in the strain space. Similar to the previous two pre-straining conditions, equi-biaxial pre-straining does not affect the FLSD. It can be concluded numerically that, at least in comparison to the FLD, the FLSD is *not* sensitive to strain path changes.

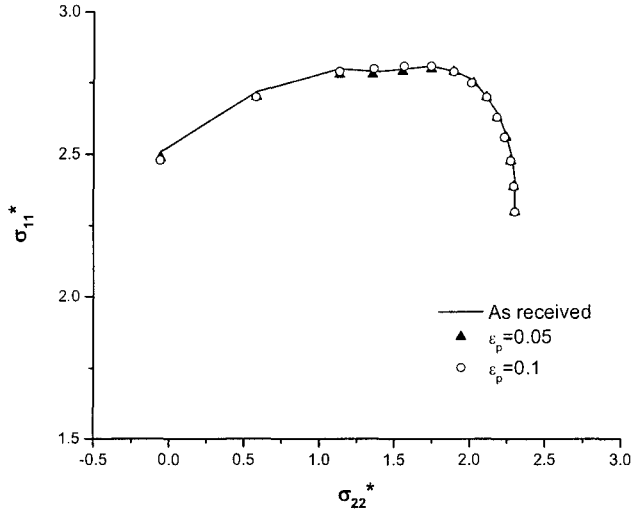

Figure 5.16: Predicted FLSDs when the sheet is pre-strained to different levels (ε_p =*0.05* and *0.01)* in equi-biaxial stretching (ρ=*1)*.

Therefore, the calculated limit stresses under proportional loading paths could be used as the Forming Limit Stress curve (FLSc or simply FLSD) for the sheet. Our numerical results also suggest that the FLSD is much more favourable than the FLD in representing forming limits in the numerical simulation of sheet metal forming processes.

CHAPTER 6

CONCLUSIONS AND FUTURE WORK

6.1 Conclusions

In the present study, the Gurson damage model has been first applied to investigate the effect of strain path change on damage evolution and work hardening of sheet metals. The Gurson model, in conjunction with the M-K approach, has been also used to predict the Forming Limit Diagram (FLD) for sheet metals. The effects of geometrical and mechanical properties of the sheet metal, as well as the strain path change on the predicted FLDs have been assessed in detail. Furthermore, the strain path dependency of the Forming Limit Stress Diagram (FLSD) has been investigated. In light of the study the following conclusions can be drawn:

1. The geometrical imperfection, H_b/Ha, has a significant influence on the FLD. The smaller the initial imperfection (1- H_b/Ha), the larger the limit strain for sheet necking.
2. A groove oriented at $\psi = 0$ is favorable for necking when $0 \le \rho \le 1$, while the critical groove orientation increases from 0 at $\rho = 0$ to 25^0 at uniaxial tension ($\rho = -0.5$).
3. Strain rate sensitivity, *m,* has a significant effect on the development of forming limit diagrams. Necking retardation is observed for whole range of strain ratios as the rate sensitivity is increased.
4. A larger value of *n* increases the limit strain, which can be attributed simply to the fact that hardening increases with increasing *n*.
5. The modulus of elasticity, *E, h*as no noticeable influence on the limit strain. This contradicts previously reported results in the literature [Wu *et al.,* 1997].

6. Initial void volume fraction, f_0, has a significant effect on the forming limit curve for strain ratios near unity, $\rho \approx 1$. Limit strain is found highest near the equi-biaxial tension condition and varies inversely with the amount of initial damage, as expected.
7. Void nucleation factors have a significant effect on forming limit diagrams. For strain controlled nucleation, necking occurs earlier than when the nucleation condition is not included. Also, the forming limit curve changes its shape for smaller difference in void volume fraction of nucleating particles, Δf_n, and the limit strain attains a higher value for all strain ratios [when it is smaller]. When nucleation strain, ε_n, is increased, the FLD moves upward. The standard deviation has an insignificant effect on the limit strains except for the strain paths near the equi-biaxial stretching ($\rho \approx 1$), where the predicted limit strain is found to be very sensitive to mechanical properties of the material.
8. The smaller the void coalescence strain f_c, the smaller the critical strain for sheet necking. The effect of f_c is most effective near the equi-biaxial stretching.
9. Changing the strain path can increase or decrease the limit strain. The predicted effects of the strain path changes on the calculated FLDs are found to be similar to the experimental observations.
10. Under the uniaxial tension pre-straining, the forming limit diagram is moved left and upward compared to the as received sheet. More specifically, pre-straining slightly increases the major limit strain ε_{11} for in-plane plane strain tension, but significantly enhances the limit strain ε_{11} for equi-biaxial stretching.
11. The FLD shape changes from U towards V due to the in-plane plane strain tension pre-straining. For uniaxial stretching, the pre-straining has almost no effect on the limit

ε , but it dramatically decreases the limit strain ε_{22}. For equi-biaxial tension, the pre-straining significantly increases the limit strain ε_{11} but decreases the limit strain ε_{22}.

12. Under the equi-biaxial tension pre-straining, the forming limit diagram shifts right and downward in relation to the as received sheet. The limit strain is reduced for both the in-plane plane strain and equi-biaxial strain conditions.

13. While FLDs are very sensitive to strain path changes, the FLSD is *not* sensitive to strain path changes. Therefore, the calculated limit stresses under proportional loading paths could be used as the Forming Limit Stress curve (FLSc or simply FLSD) for the sheet. Our numerical results also suggest that the FLSD is much more favourable than the FLD in representing forming limits in the numerical simulation of sheet metal forming processes.

6.2 Future Work

The work can be extended by studying the following:

- Effect of anisotropy on strain path deformation
- Effect of superimposed hydrostatic pressure on the developed model incorporating Gurson's damage criterion.

REFERENCES

Alsos H. S., Hopperstad O. S., Törnqvist R. and Amdahl J.; Analytical and numerical analysis of sheet metal instability using a stress based criterion; International Journal of Solids and Structures; 2008, Vol.45, pp.2042–2055.

Argon A. S., Im J. and Safoglu R.; Cavity formation from inclusions in ductile fracture; Metallurgical transactions A; 1975, Vol.6A, pp.825-837.

Arrieux R., Bedrin C. and Boivin M.; Determination of an intrinsic forming limit stress diagram for isotropic metal sheets; In:Proceedings of the 12th Biennial Congress IDDRG; 1982, pp. 61–71.

Arrieux R.; Determination and use of the forming limit stress diagrams in sheet metal forming; Journal of Materials Processing Technology; 1995, Vol.53, pp. 47–56.

Avitzur B.; Metal forming: the application of limit analysis; Published by Dekker, New York; 1980.

Azrin M. and Backofen W. A.; The deformation and failure of a biaxial stretched sheet; Metallurgical transactions; 1970, Vol.1, pp.2857

Bai Y. and Wierzbicki T.; Forming severity concept for predicting sheet necking under complex loading histories; International Journal of Mechanical Sciences; 2008, Vol.50, pp.1012-1022.

Barata Da Rocha A., Barlat F. and Jalinier J. M.; Prediction of the forming limit diagram of anisotropic sheets in linear and nonlinear loading; Materials Science and Engineering; 1984, Vol.68, Issue.2, pp.151-164.

Benseddiq N. and Imad A.; A ductile fracture analysis using a local damage model; International Journal of Pressure Vessels and Piping; 2008, Vol.85, Issue.4, pp.219-227.

Brocks W. and G. Bernauer G.; Determination of the Gurson parameters by numerical simulations, in: 2nd Griffith Conference Sheffield, 13th–15th September; 1995.

Brunet M. and Morestin F.; Experimental and analytical necking studies of anisotropic sheet metals; Journal of Materials Processing Technology; 2001, Vol.112, pp.214-226.

Chan H. –L., Spence A. D. and Sklad M. P.; Laser digitizer-based sheet metal strain and surface analysis; International Journal of Machine Tools & Manufacture; 2007, Vol.47, pp.191-203.

Chu C.C. and Needleman A.; Void nucleation effects in biaxially stretched sheets; Journal of Engineering Materials and Technology; 1980, Vol.102, pp.249-256.

Coffin L. and Rogers, H.C., 1967. Influence of pressure on the structural damage in metal forming processes; ASM TRANS QUART; 1967, Vol.60, pp.672–686.

Gantar G. and Kuzman K.; Sensitivity and stability evaluation of the deep drawing process; Journal of Materials Processing Technology; 2002, Vol.125–126, pp. 302–308.

Ghosh A. K. and Backofen W. A.; Strain hardening and instability in biaxially stretched sheet; Metallurgical transactions; 1973, Vol.4, pp.1113-1123.

GOM; Determination of forming limit diagrams using ARAMIS; 2001, Braunschweig, Germany.

Gronostajski J. Z.; Sheet metal forming limits for complex paths; Journal of Materials Processing Technology; 1984, Vol.10, pp.349-362.

Goods S.H. and Brown L.M.; The nucleation of cavities by plastic deformation, Acta Metallurgica; 1979, Vol.27, pp.1-15.

Goodwin G. M.; Application of strain analysis to sheet metal forming in the press shop; La Metallurgica; 1968, Vol. 60, pp.767-774.

Graf A. and Hosford W.; Effect of Changing Strain Paths on Forming Limit Diagrams of Al 2008-T4; Metallurgical Transactions; 1993, Vol.24A, pp.2503-2512.

Graf A. and Hosford W.; The Influence of Strain-Path Changes on Forming Limit Diagrams of Al 6111 T4; International Journal of Mechanical Sciences; 1994, Vol.36, Issue.10, pp.897-910.

Gurson A. L.; Continuum theory of ductile rupture by void nucleation and growth—part I: yield criteria and flow rules for porous ductile media; ASME Journal of Engineering Materials and Technology; 1977, Vol.**99**, pp. 2–15.

Haddad A., Arrieux R. and Vacher P.; Use of two behavior laws for the determination of the forming limit stress diagram of a thin steel sheet: results and comparisons; Journal of Materials processing Technology; 2001, Vol.106, pp.49-53.

Harvey D.N.; Optimizing patterns and computational algorithms for automatic, optical strain measurement in sheet metal, efficiency in sheet metal forming; In proceedings of the 13th Biennial Congress; Melbourne, Australia; International Deep Drawing Research Group, 1984, pp. 403–414.

Hill R.; A theory of yielding and plastic flow of anisotropic metals; Proc. R. Soc. London; 1948, Vol.193A, pp.197–281.

Hill R.; On discontinuous plastic states, with special reference to localized necking in thin sheets; Journal of the Mechanics and Physics of Solids; 1952, Vol.1, pp.19-30.

Hill R. and Hutchinson J. W.; Bifurcation Phenomena in the Plane Tension Test; Journal of the Mechanics and Physics of Solids; 1975, Vol.23, pp.239-264.

Hill R.; Constitutive modeling of orthotropic plasticity in sheet metals; Journal of the Mechanics and Physics of Solids; 1990, Vol.38, pp.405-417.

Hiwatashi S., Bael A.V., Houtte P. V. and Teodosiu C.; Prediction of forming limit strains under strain path changes: application of an anisotropic model based on texture and dislocation structure; International Journal of Plasticity; 1998, Vol.14, pp.647-669.

Hosford W. A.; On yield loci of anisotropic cubic metals; In: proceedings of the North American Metalworking conference, SME, Dearborn, MI; 1979, pp.191-197.

Hsu Q.-C.; Comparison of different analysis models to measure plastic strains on sheet metal forming parts by digital image processing; International Journal of Machine Tools & Manufacture; 2002, Vol.43, Issue.5, pp.515–521.

Huang H. M., Pan J. and Tang S. C.; Failure prediction in anisotropic sheet metals under forming operations with consideration of rotating principal stretch directions; International Journal of Plasticity; 2000, Vol.16, Issue.6, pp.611-633.

Hutchinson J.W. and Neale K.W.; Sheet Necking – III. Strain-Rate Effects; Mechanics of Sheet Metal Forming, edited by D. P. Koistinen and Wang N. M.; Plenum Publishing Corporation; 1978, pp.269-285.

Hutchinson W. B., Arthey R. and Malmstrom P.; On anomalously low work-hardening in pre-strained metals; Scripta Metallurgica et Materialia; 1976, Vol.10, pp.673-675.

Jalinier J. M.; Calculation of the forming limit curve at fracture; Journal of Materials Science; 1983, Vol.18, pp.1794-1802.

Janssens K., Lambert F., Vanrostenberghe S. and Vermeulen M.; Statistical evaluation of the uncertainty of experimentally characterized forming limits of sheet steel; Journal of Materials processing Technology; 2001, Vol.112, Issue:2-3, pp.174-184.

Keeler S. P. and Backhofen W. A.; Plastic instability and fracture in sheet stretched over rigid punches; ASM TRANS QUART; 1964, Vol.56, pp.25–48.

Keeler S. P.; Circular Grid System – A Valuable Aid for Evaluating Sheet-Metal Formability; Sheet Metal Industries; 1969, Vol.45, pp.633-641.

Keeler S. P.; Determination of forming limits in automotive stamping; Sheet metal ind.; 1965, Vol.42, pp.683-691.

Kim K. H. and Kim D. W.; The effect of void growth on the limit strains of steel sheets; International Journal of Mechanical Science; 1983, Vol.25, Issue.4, pp.293-300.

Kuroda M. and Tvergaard V.; Forming limit diagrams for anisotropic metal sheets with different yield criteria; International Journal of Solids and Structures; 2000, Vol.37, pp.5037–5059.

Laukonis J. V. and Ghosh A. K.; Effects of Strain Path Changes on the Formability of Sheet Metals; Metallurgical Transactions A; 1978, Vol.9A, pp.1849-1856.

Lee J. Y.; An orientation-invariant method for automated circular grid analysis in sheet metal forming; Master thesis, National Cheng Kung University, Taiwan; 1996.

Lee R. S. and Hsu Q. C.; Image-Processing System for Circular-Grid Analysis in Sheet-Metal Forming; Experimental Mechanics; 1994, Vol.34, Issue.2, pp.108-115.

Lee S. H. and Kobayashi S.; The Effects of Strain Paths on the Stretching Limit Strains of Sheet Metal with Planar Anisotropy; Society of Manufacturing Engineers; 1975, pp.591-596.

Lewison D. J. and Lee D.; Determination of Forming Limits by Digital Image Processing Methods; SAE Technical Paper, (1999-01-3168); 1999.

Marciniak Z. and Kuczynski K.; Limit strains in the processes of stretch forming sheet steel; International Journal of Mechanical Sciences; 1967, Vol.9, pp.609–620.

Marciniak Z.; Aspects of material formability; Hamilton, McMaster University; 1974. From Formability of Metallic Materials By Bunge H. J., D. Banabic D., Pöhlandt K. and Tekkaya A. K.

Marciniak Z., Duncan J. L. and Hu S. J.; Mechanics of sheet metal forming; Butterworth-Heinemann, London; 1992.

Nakazima K., Kikuma T. and Hasuka K.; Study on the formability of steel sheets; Vawata Technical Report No. 264; 1968, pp.141–154.

Needleman, A. and Triantafyllidis N.; Void growth and local necking in biaxial stretched sheets; ASME Journal of Engineering Materials and Technology; 1978, Vol.100, pp. 164-168.

Needleman A. and Tvergaard V.; Limits to Formability in Rate-Sensitive Metal Sheets; Mechanical Behavior of Materials - IV, edited by Carlson J. and Ohlson N. G., Pergamon Press; 1984, pp.51-65.

Peirce D., Shih C. F. and Needleman A.; A Tangent Modulus Method for Rate Dependent Solids; Computers and Structures; 1984, Vol.18, pp.875-887.

Puttick K. E.; Ductile fracture in metals; Philosophical magazine; 1959, Vol.4, pp.964-969.

Rao U. S. and Chaturvedi, R. C.; 1986. Sheet metal forming limits under complex strain paths using void growth and coalescence model; Journal of Engineering Materials and Technology, ASME; 1986, Vol.108, pp.240.
Sachs, G.; Fundamentals of the working of metals; 1954, Interscience, New York, U.S.A.

Saje M, Pan J. and Needleman A.; Void Nucleation Effects on Shear Localization in Porous Plastic Solids; International Journal of Fracture; 1982, Vol.19, pp.163-182.

Schedin E. and Melander A.; The evaluation of large strain from industrial sheet metal stamping with a square grid; Journal of Applied Metalworking; 1986, Vol.4, Issue.2, pp.143–151.

Sklad M. P.; Aspects of automated measurement of proportional and non-proportional deformation in sheet metal forming; Journal of Material Processing Technology; 2004, Vol.145, pp.377-384.

Springmann M.and Kuna M.; Identification of material parameters of the Gurson–Tvergaard–Needleman model by combined experimental and numerical techniques; Computational Materials Science;2005,Vol.33, Issue.4, pp.501-509.

Storen S. and Rice J. R.; Localized necking in thin sheets; Journal of the Mechanics and Physics of Solids; 1975, Vol.23, pp.421-441.

Stoughton T. B.; General forming limit criterion for sheet metal forming; International Journal of Mechanical Sciences; 2000, Vol.42, Issue.1, pp.1-27.

Stoughton T. B. and Zhu X.; Review of theoretical models of the strain-based FLD and their relevance to the stress-based FLD; International Journal of Plasticity; 2004, Vol.20, pp.1463–1486.

Tarigopula V., Hopperstad O. S., Langseth M. and Clausen A. H; Elastic-plastic behavior of dual-phase, high-strength steel under strain-path changes; European Journal of Mechanics - A/Solids; 2008, Vol.27, pp.764-782.

Tisza M., Lukacs Z. and Gal G.; Integrated Process Simulation and Die-Design in Sheet Metal; International Journal of Material Forming; 2008, DOI.10.1007/s12289-008-0022-3.

Tjotta S. T.; Formability and the growth of damage; Numerical Methods in Industrial Forming Processes edited by Chenot J. L., Wood R. and Zienkiewicz O. C.; Balkema, Amsterdam; 1992, pp.187-192.

Tvergaard V.; On localization in ductile materials containing spherical voids; International Journal of Fracture; 1982, Vol.18, pp. 237-251.

Tvergaard V. and Needleman A.; Analysis of the Cup-Cone Fracture in a Round Tensile Bar; Acta Metallurgica; 1984, Vol.32, pp.157-169.

Tvergaard V.; Material failure by void growth to coalescence; Advances in Applied Mechanics; 1990, Vol.27, pp.83-151.

Verma N. S. P., Narasimhan R., Luo A. A. and Sachdev A. K.; An analysis of localized necking in aluminum alloy tubes during hydroforming using a continuum damage model; International Journal of Mechanical Sciences; 2007, Vol.49, pp.200-209.

Wagoner R. H. and Laukonis J. V.; Plastic Behavior of Aluminum-Killed Steel Following Plane-Strain Deformation; Metallurgical Transactions A; 1983, vol.14A, pp.1487-1495.

Wang C. C., Lee J., Chen L. W. and Lai H. Y.; A New Method for Circular Grid Analysis in the Sheet Metal Forming Test; Experimental Mechanics; 2000, Vol.40, Issue.2, pp.190-196.

Wang C. T.; Advanced Stamping Simulation Technology – State of Business and Industrial Prospect; Numisheet Conference, Besancon; 1999, Vol.13-17, pp. 250-256.

Wick C., Benedict J. T. and Veillux R. F (Editors); Tool and Manufacturing Engineers Handbook, Forming 2, 4th edition; Society of Manufacturing Engineers; Dearborn, Michigan, 1984, Chapter 1.

Wu P.D., Neale, K. W. and Van Der Giessen E.; On crystal plasticity FLD analysis; Proceedings of the Royal Society of London A; 1997, Vol.453, pp.1831-1848.

Wu P. D., Neale K. W. and Van Der Giessen E.; Effects of strain paths on sheet Metal Limit Strains; In: R. de Borst and E. van der Giessen, Editors; Materials Instabilities in Solids; John Wiley & Sons Ltd., Chichester;1998, pp. 243–253.

Wu P.D., Jain M., MacEwwn S. R. , Tugcu P. and Neale K. W.; Evaluation of anisotropic yield function for aluminum sheets; International Journal of Plasticity; 2003, Vol.19, pp.121-138.

Wu P. D., MacEwen S. R., Graf A., Jain M. and Neale K. W.; On forming limit stress diagram analysis; International Journal of Solids and Structures; 2005, Vol.42, Issue.8, pp.2225-2241.

Yamamoto H.; Conditions for shear localization in the ductile fracture of void-containing materials; International Journal of Fracture; 1978, Vol.14, pp. 347-365.

Zandrahimi M., Wilson D. V. and Roberts W. T.; Effects of changes in strain path on work-hardening in CP Aluminum and an Al-Cu-Mg Alloy; Acta Metallurgica et Materialia; 1989, Vol.38, No.2, pp.215-226.

Zhou Y. and Neale K. W.; Predictions of forming limit diagrams using a rate-sensitive crystal plasticity model; International Journal of Mechanical Sciences; 1995, Vol.37, pp.1-20.

Zhao L., Sowerby R. and Sklad M. P.; A theoretical and experimental investigation of limit strains in sheet metal forming; International Journal of Mechanical Sciences; 1996, Vol.38, pp.1307-1317.

Zhao L.; Limit strains in sheet metal forming: A theoretical and experimental investigation; A thesis submitted to McMaster University; 1993.

Zimniak Z.; Implementation of the forming limit stress diagram in FEM simulations; Journal of Material Processing Technology; 2000, Vol.106, Issue.1-3, pp.261-266.

APPENDIX A

In order to increase the time step size, we use the tangent modulus method for a rate-sensitive elastic-plastic constitutive model developed by Peirce et al. [1984]. We define the increment of effective viscoplastic strain by

$$\Delta\bar{\varepsilon} = \Delta t\left[\theta \times \dot{\bar{\varepsilon}}_{t+\Delta t} + (1-\theta)\times \dot{\bar{\varepsilon}}_{t}\right] \tag{A-1}$$

with

$$\dot{\bar{\varepsilon}}_{t+\Delta t} = \dot{\bar{\varepsilon}}_{t} + \left[\frac{\partial \dot{\bar{\varepsilon}}}{\partial \bar{\sigma}}\dot{\bar{\sigma}} + \frac{\partial \dot{\bar{\varepsilon}}}{\partial \bar{\varepsilon}}\dot{\bar{\varepsilon}}\right]\Delta t \tag{A-2}$$

Differentiating equation (3.6) we get

$$\frac{\partial \phi}{\partial \boldsymbol{\sigma}} = p = \frac{3\boldsymbol{\sigma}'}{\bar{\sigma}^2} + \frac{f q_1 q_2}{\bar{\sigma}}\sinh\left(\frac{q_2\sigma_m}{2\bar{\sigma}}\right)\mathbf{1}, \tag{A-3a}$$

$$\frac{\partial \phi}{\partial \bar{\sigma}} = -\frac{2\sigma_e^{\,2}}{\bar{\sigma}^3} - \frac{f q_1 q_2 \sigma_m}{\bar{\sigma}^2}\sinh\left(\frac{q_2\sigma_m}{2\bar{\sigma}}\right) \tag{A-3b}$$

$$\frac{\partial \phi}{\partial f} = 2q_1\cosh\left(\frac{q_2\sigma_m}{2\bar{\sigma}}\right) - 2q_3 f \tag{A-3c}$$

From the consistency condition (3.17) and (3.24) we have

$$\dot{\bar{\sigma}} = -\frac{\left(\boldsymbol{p} : \overset{\nabla}{\boldsymbol{\sigma}} + \dfrac{\partial \phi}{\partial f}\dot{f}\right)}{\dfrac{\partial \phi}{\partial \bar{\sigma}}} = -\frac{\boldsymbol{p} : \overset{\nabla}{\boldsymbol{\sigma}} + (1-f)\dfrac{\partial \phi}{\partial f}\boldsymbol{I} : \boldsymbol{D}^p + a\dfrac{\partial \phi}{\partial f}\dot{\bar{\varepsilon}} + A\dfrac{\partial \phi}{\partial f}\dot{\bar{\sigma}} + \dfrac{1}{3}B\dfrac{\partial \phi}{\partial f}\boldsymbol{I} : \overset{\nabla}{\boldsymbol{\sigma}}}{\dfrac{\partial \phi}{\partial \bar{\sigma}}}$$

$$\Rightarrow \left(\frac{\partial \phi}{\partial \bar{\sigma}} + A\frac{\partial \phi}{\partial f}\right)\dot{\bar{\sigma}} = -\mathbf{p} : \overset{\nabla}{\boldsymbol{\sigma}} - (1-f)\frac{\partial \phi}{\partial f}\mathbf{I} : \mathbf{D}^p - a\frac{\partial \phi}{\partial f}\dot{\bar{\varepsilon}} - \frac{1}{3}B\frac{\partial \phi}{\partial f}\mathbf{I} : \overset{\nabla}{\boldsymbol{\sigma}} \tag{A-4}$$

$$\Rightarrow \dot{\bar{\sigma}} = -\frac{\mathbf{p}:\overset{\nabla}{\boldsymbol{\sigma}} + (1-f)\dfrac{\partial \phi}{\partial f}\mathbf{I}:\mathbf{D}^p + a\dfrac{\partial \phi}{\partial f}\dot{\bar{\varepsilon}} + \dfrac{1}{3}B\dfrac{\partial \phi}{\partial f}\mathbf{I}:\overset{\nabla}{\boldsymbol{\sigma}}}{\dfrac{\partial \phi}{\partial \bar{\sigma}} + A\dfrac{\partial \phi}{\partial f}}$$

Now from equation (A-3) and (A-4) all the variables are determined separately such that

$$\mathbf{p}:\overset{\nabla}{\boldsymbol{\sigma}} + + \frac{1}{3}B\frac{\partial \phi}{\partial f}\mathbf{I}:\overset{\nabla}{\boldsymbol{\sigma}} = \left(\mathbf{p} + \frac{1}{3}B\frac{\partial \phi}{\partial f}\mathbf{I}\right):\left(\dot{\boldsymbol{\sigma}} + \boldsymbol{\sigma}\cdot\mathbf{W} - \mathbf{W}\cdot\boldsymbol{\sigma}\right)$$

$$= \left(\frac{3\sigma'_{ij}}{\bar{\sigma}^2} + \left(\frac{fq_1q_2}{\bar{\sigma}}\sinh\left(\frac{q_2\sigma_m}{2\bar{\sigma}}\right) + \frac{1}{3}B\frac{\partial \phi}{\partial f}\right)g_{ij}\right)\left(\dot{\sigma}_{ij} + \sigma_{ik}\cdot W_{kj} - W_{ik}\cdot\sigma_{kj}\right) \qquad \text{(A-5a)}$$

$$= \frac{2\sigma_e\dot{\sigma}_e}{\bar{\sigma}^2} + \frac{6\sigma'_{ij}}{\bar{\sigma}^2}\sigma_{ik}W_{kj} + \left(\frac{fq_1q_2}{\bar{\sigma}}\sinh\left(\frac{q_2\sigma_m}{2\bar{\sigma}}\right) + \frac{1}{3}B\frac{\partial \phi}{\partial f}\mathbf{I}\right)\dot{\sigma}_{kk}$$

$$\boldsymbol{I}:\boldsymbol{D}^p = \dot{E}\boldsymbol{I}:\boldsymbol{p} = 3\dot{E}\frac{fq_1q_2}{\bar{\sigma}}\sinh\left(\frac{q_2\sigma_m}{2\bar{\sigma}}\right)$$

$$(1-f)\frac{\partial \phi}{\partial f}\boldsymbol{I}:\boldsymbol{D}^p = \left(2q_1\cosh\left(\frac{q_2\sigma_m}{2\bar{\sigma}}\right) - 2q_3f\right)\left((1-f)\left(D_{11}^p + D_{22}^p + D_{33}^p\right) + a\dot{\bar{\varepsilon}} + A\dot{\bar{\sigma}}\right) \qquad \text{(A-5b)}$$

$$-\left(\frac{\partial \phi}{\partial \bar{\sigma}} + A\frac{\partial \phi}{\partial f}\right)\dot{\bar{\sigma}} = \left(\mathbf{p} + \frac{1}{3}B\frac{\partial \phi}{\partial f}\mathbf{I}\right):\overset{\nabla}{\boldsymbol{\sigma}} + (1-f)\frac{\partial \phi}{\partial f}\dot{E}(\mathbf{I}:\mathbf{P}) + a\frac{\partial \phi}{\partial f}\dot{\bar{\varepsilon}}$$

$$= \mathbf{q}:\overset{\nabla}{\boldsymbol{\sigma}} + (1-f)\frac{\partial \phi}{\partial f}\dot{E}(\mathbf{I}:\mathbf{P}) + a\frac{\partial \phi}{\partial f}\dot{\bar{\varepsilon}} \qquad \text{(A-5c)}$$

In equation (A-5c) **q** is determined as

$$\boldsymbol{q} = \boldsymbol{p} + \frac{1}{3}B\frac{\partial \phi}{\partial f}\boldsymbol{I}$$

Substituting equation (A-2) into equation (3.16) it can be found that

$$\dot{\chi} = \frac{(1-f)\overline{\sigma}\dot{\bar{\varepsilon}}}{\boldsymbol{\sigma}:\mathbf{p}} = \frac{(1-f)\overline{\sigma}}{\boldsymbol{\sigma}:\mathbf{p}}\dot{\bar{\varepsilon}}_t + \frac{(1-f)\overline{\sigma}}{\boldsymbol{\sigma}:\mathbf{p}}\theta\Delta t\frac{\partial\dot{\bar{\varepsilon}}}{\partial\overline{\sigma}}\dot{\overline{\sigma}} + \frac{(1-f)\overline{\sigma}}{\boldsymbol{\sigma}:\mathbf{p}}\theta\Delta t\frac{\partial\dot{\bar{\varepsilon}}}{\partial\overline{\varepsilon}}\dot{\bar{\varepsilon}}$$

$$\Rightarrow \dot{\chi} = \dot{\chi}_t + \frac{(1-f)\overline{\sigma}}{\boldsymbol{\sigma}:\mathbf{p}}\theta\Delta t\frac{\partial\dot{\bar{\varepsilon}}}{\partial\overline{\sigma}}\dot{\overline{\sigma}} + \frac{(1-f)\overline{\sigma}}{\boldsymbol{\sigma}:\mathbf{p}}\theta\Delta t\frac{\partial\dot{\bar{\varepsilon}}}{\partial\overline{\varepsilon}}\dot{\bar{\varepsilon}}$$

$$\Rightarrow \dot{\chi} = \dot{\chi}_t + \frac{\partial\dot{\bar{\varepsilon}}}{\partial\overline{\varepsilon}}\dot{\chi}\theta\Delta t - \frac{(1-f)\overline{\sigma}}{\boldsymbol{\sigma}:\mathbf{p}}\theta\Delta t\frac{\partial\dot{\bar{\varepsilon}}}{\partial\overline{\sigma}}\frac{\left(\mathbf{q}:\mathbf{L}:(\mathbf{D}-\dot{\chi}\mathbf{p}) + (1-f)\frac{\partial\phi}{\partial f}\dot{\chi}(\mathbf{I}:\mathbf{P}) + a\frac{\partial\phi}{\partial f}\dot{\bar{\varepsilon}}\right)}{\left(\frac{\partial\phi}{\partial\overline{\sigma}} + A\frac{\partial\phi}{\partial f}\right)}$$

$$\Rightarrow \dot{\chi} = \dot{\chi}_t + \frac{\partial\dot{\bar{\varepsilon}}}{\partial\overline{\varepsilon}}\dot{\chi}\theta\Delta t + \frac{(1-f)\overline{\sigma}}{\boldsymbol{\sigma}:\mathbf{p}}\theta\Delta t\frac{\partial\dot{\bar{\varepsilon}}}{\partial\overline{\sigma}}\frac{\mathbf{q}:\mathbf{L}:\mathbf{p}}{\left(\frac{\partial\phi}{\partial\overline{\sigma}} + A\frac{\partial\phi}{\partial f}\right)}\dot{\chi} - \theta\Delta t\frac{\partial\dot{\bar{\varepsilon}}}{\partial\overline{\sigma}}\frac{a\frac{\partial\phi}{\partial f}}{\left(\frac{\partial\phi}{\partial\overline{\sigma}} + A\frac{\partial\phi}{\partial f}\right)}\dot{\chi}$$

$$-\frac{(1-f)^2\overline{\sigma}}{\boldsymbol{\sigma}:\mathbf{p}\left(\frac{\partial\phi}{\partial\overline{\sigma}} + A\frac{\partial\phi}{\partial f}\right)}\theta\Delta t\frac{\partial\dot{\bar{\varepsilon}}}{\partial\overline{\sigma}}\frac{\partial\phi}{\partial f}(\mathbf{I}:\mathbf{P})\dot{\chi} - \frac{(1-f)\overline{\sigma}}{\boldsymbol{\sigma}:\mathbf{p}}\theta\Delta t\frac{\partial\dot{\bar{\varepsilon}}}{\partial\overline{\sigma}}\frac{(\mathbf{q}:\mathbf{L}:\mathbf{D})}{\left(\frac{\partial\phi}{\partial\overline{\sigma}} + A\frac{\partial\phi}{\partial f}\right)}$$

$$\Rightarrow \dot{\chi} = \dot{\chi}_t + \dot{\chi}\theta\Delta t\frac{(1-f)\overline{\sigma}}{\boldsymbol{\sigma}:\mathbf{p}}\frac{\partial\dot{\bar{\varepsilon}}}{\partial\overline{\sigma}}\frac{1}{\frac{\partial\phi}{\partial\overline{\sigma}} + A\frac{\partial\phi}{\partial f}}$$

$$\left\{\mathbf{q}:\mathbf{L}:\mathbf{p} - (1-f)\frac{\partial\phi}{\partial f}(\mathbf{I}:\mathbf{P}) - a\frac{\partial\phi}{\partial f}\frac{\boldsymbol{\sigma}:\mathbf{p}}{(1-f)\overline{\sigma}} + \frac{\boldsymbol{\sigma}:\mathbf{p}}{(1-f)\overline{\sigma}}\frac{\partial\dot{\bar{\varepsilon}}}{\partial\overline{\varepsilon}}\left(\frac{\partial\dot{\bar{\varepsilon}}}{\partial\overline{\sigma}}\right)^{-1}\left(\frac{\partial\phi}{\partial\overline{\sigma}} + A\frac{\partial\phi}{\partial f}\right)\right\} \qquad \text{(A-6)}$$

$$-\frac{(1-f)\overline{\sigma}}{\boldsymbol{\sigma}:\mathbf{p}}\theta\Delta t\frac{\partial\dot{\bar{\varepsilon}}}{\partial\overline{\sigma}}\frac{(\mathbf{q}:\mathbf{L}:\mathbf{D})}{\left(\frac{\partial\phi}{\partial\overline{\sigma}} + A\frac{\partial\phi}{\partial f}\right)}$$

Let,

$$\xi = -\theta\Delta t\frac{(1-f)\overline{\sigma}}{\boldsymbol{\sigma}:\mathbf{p}}\frac{\partial\dot{\bar{\varepsilon}}}{\partial\overline{\sigma}}\frac{1}{\frac{\partial\phi}{\partial\overline{\sigma}} + A\frac{\partial\phi}{\partial f}};$$

$$H = \left(\mathbf{q}:\mathbf{L}:\mathbf{p} - (1-f)\frac{\partial\phi}{\partial f}(\mathbf{I}:\mathbf{P}) - a\frac{\partial\phi}{\partial f}\frac{\boldsymbol{\sigma}:\mathbf{p}}{(1-f)\overline{\sigma}} + \frac{\boldsymbol{\sigma}:\mathbf{p}}{(1-f)\overline{\sigma}}\frac{\partial\dot{\bar{\varepsilon}}}{\partial\overline{\varepsilon}}\left(\frac{\partial\dot{\bar{\varepsilon}}}{\partial\overline{\sigma}}\right)^{-1}\left(\frac{\partial\phi}{\partial\overline{\sigma}} + A\frac{\partial\phi}{\partial f}\right)\right)$$

So, Finally $\dot{\chi} = \frac{1}{1+\xi}\dot{\chi}_t + \frac{\xi}{1+\xi}\frac{1}{H}\mathbf{Q}:\mathbf{D}$ (A-7)

Here, here $\boldsymbol{Q} = \boldsymbol{q} : \boldsymbol{L}$

Putting the value of $\dot{\chi}$ into equation (3.14)

$$\begin{aligned}
\overset{\nabla}{\boldsymbol{\sigma}} &= \mathbf{L} : \left(\mathbf{D} - \mathbf{D}^{p}\right) = \mathbf{L} : \mathbf{D} - \dot{\chi}\mathbf{P} \\
&= \mathbf{L} : \mathbf{D} - \left(\frac{1}{1+\xi}\dot{\chi}_{t} + \frac{\xi}{1+\xi}\frac{1}{H}\mathbf{Q} : \mathbf{D}\right)\mathbf{P} \\
&= \left(\mathbf{L} - \frac{\xi}{1+\xi}\frac{1}{H}\mathbf{PQ}\right) : \mathbf{D} - \frac{\mathbf{P}}{1+\xi}\dot{\chi}_{t}
\end{aligned} \tag{A-8}$$

APPENDIX B

From equations (3.27), (3.33) and (3.34), for the material inside the band:

$$\begin{aligned}\dot{\sigma}^B_{\alpha\beta} &= L^B_{\alpha\beta\kappa\gamma} : D^B_{\kappa\gamma} + L^B_{\alpha\beta 33} : D^B_{33} - L^B_{\alpha\beta\kappa\gamma} : D^{pB}_{\kappa\gamma} - L^B_{\alpha\beta 33} : D^{pB}_{33} \\ &\quad - \sigma^B_{\alpha\kappa}\cdot W^B_{\kappa\beta} + W^B_{\alpha\kappa}\cdot\sigma^B_{\kappa\beta} - \sigma^B_{\alpha\beta}\left(D^B_{\kappa\kappa} + D^B_{33}\right) - \dot{\bar{\sigma}}^B_{\alpha\beta} \\ &= L^B_{\alpha\beta\kappa\gamma}\left(D^B_{\kappa\gamma} + \frac{1}{2}\left(g_\kappa N_\gamma + g_\gamma N_\kappa\right)\right) + L^B_{\alpha\beta 33}D^B_{33} - L^B_{\alpha\beta\kappa\gamma}D^{pB}_{\kappa\gamma} - L^B_{\alpha\beta 33}D^{pB}_{33} \\ &\quad - \frac{1}{2}\sigma^B_{\alpha\kappa}\left(g_\kappa N_\beta - N_\kappa g_\beta\right) + \frac{1}{2}\left(g_\alpha N_\kappa - N_\alpha g_\kappa\right)\sigma^B_{\kappa\beta} - \sigma^B_{\alpha\beta}\left(D^A_{\kappa\kappa} + g_\kappa N_\kappa + D^B_{33}\right) - \dot{\bar{\sigma}}^B_{\alpha\beta}\end{aligned} \tag{B-1}$$

While for the material outside the band:

$$\dot{\sigma}_{\alpha\beta} = L_{\alpha\beta\kappa\gamma}D^A_{\kappa\gamma} + L_{\alpha\beta 33}D_{33} - L_{\alpha\beta\kappa\gamma}D^{pA}_{\kappa\gamma} - L_{\alpha\beta 33}D^{pA}_{33} - \sigma^A_{\alpha\beta}\left(D^A_{\kappa\kappa} + D^A_{33}\right) - \dot{\bar{\sigma}}_{\alpha\beta} \tag{B-2}$$

Note the range of Greek tensor indices $\alpha,\beta = 1,2$, while italic indices run from 1 to 3.

The equilibrium condition at the band interface for the current configuration is given at time t by

$$N_\alpha \sigma^B_{\alpha\beta} h_B = N_\alpha \sigma_{\alpha\beta} h \tag{B-3}$$

At time $(t+dt)$ we have

$$\left(N_\alpha + \dot{N}_\alpha dt\right)\left(\sigma_{\alpha\beta} + \dot{\sigma}_{\alpha\beta}dt\right)\left(h + \dot{h}dt\right) = N_{\alpha\sigma}\dot{\sigma}_{\alpha\beta}hdt + N_\alpha\sigma_{\alpha\beta}h + \sigma_{\alpha\beta}\left(\dot{N}_\alpha h + N_\alpha\dot{h}\right)dt$$

Dividing equation (B-3) by $h_B dt$ and let $\xi = \dfrac{h}{h_B}$ we find

$$N_\alpha \dot{\sigma}^B_{\alpha\beta} = \xi N_\alpha \dot{\sigma}_{\alpha\beta} + \frac{N}{dt}\left(\xi\sigma_{\alpha\beta} - \sigma^B_{\alpha\beta}\right) - \left(N_\alpha\frac{\dot{h}_B}{h_B} + N_\alpha\right)\sigma^B_{\alpha\beta} + \xi\left(N_\alpha\frac{\dot{h}}{h} + N_\alpha\right)\sigma_{\alpha\beta}$$

Let $\dfrac{\dot{h}}{h} = D_{33}$, $\dfrac{\dot{h}_B}{h_B} = D^B_{33}$ and apply (B-1) and (B-2), the above equation becomes

$$\begin{aligned}\bar{R}_{\beta\kappa}g_\kappa + N_\alpha \mathrm{L}^B_{\alpha\beta 33}D^B_{33} &= N_\alpha(\xi\,\mathrm{L}_{\alpha\beta\kappa\gamma} - \mathrm{L}^B_{\alpha\beta\kappa\gamma})D_{\kappa\gamma} + \xi N_\alpha \mathrm{L}_{\alpha\beta 33}D_{33} - N_\alpha\left(\xi\dot{\bar{\sigma}}_{\alpha\beta} - \dot{\bar{\sigma}}^B_{\alpha\beta}\right) \\ &\quad + \left(\frac{N_\alpha}{dt} + \dot{N}_\alpha - N_\alpha D_{\kappa\kappa}\right)\left(\xi\sigma_{\alpha\beta} - \sigma^B_{\alpha\beta}\right)\end{aligned} \tag{B-4}$$

Where

$$\overline{R}_{\beta\kappa} = R_{\beta\kappa} - \frac{1}{2} N_\alpha N_\beta \sigma^B_{\alpha\kappa} + \left(\frac{1}{2} N_\alpha \sigma^B_{\alpha\gamma} N_\gamma \right) \delta_{\beta\kappa} + \frac{1}{2} N_\alpha N_\kappa \sigma^B_{\alpha\beta} - \frac{1}{2} \sigma^B_{\beta\kappa} - N_\alpha N_\kappa \sigma^B_{\alpha\beta}$$

And

$$R_{\beta\kappa} = N_\alpha \mathrm{L}^B_{\alpha\beta\kappa\gamma} N_\gamma$$

From the plane stress condition outside the band ($\dot{\sigma}_{33} = 0$)

$$\dot{\sigma}_{33} = \mathrm{L}_{3311} D_{11} + \mathrm{L}_{3322} \rho D_{11} + \mathrm{L}_{3333} D_{33} - \dot{\bar{\sigma}}_{33} - \sigma_{33} D_{11} - \sigma_{33} D_{22} - \sigma_{33} D_{33} = 0$$

We have

$$D_{33} = \frac{\dot{\bar{\sigma}}_{33} + \left[(1+\rho) \cancel{\sigma_{33}} - (\mathrm{L}_{3311} + \rho \mathrm{L}_{3322}) \right] D_{11}}{\mathrm{L}_{3333} - \cancel{\sigma_{33}}}$$

From the plane stress condition inside the band ($\dot{\sigma}^B_{33} = 0$):

$$L^B_{33\kappa\gamma} \left(D^A_{\kappa\gamma} + \frac{1}{2} \left(g_\kappa N_\gamma + g_\gamma N_\kappa \right) \right) + L^B_{3333} D^B_{33} - L^B_{33\kappa\gamma} D^{pB}_{\kappa\gamma} - L^B_{3333} D^{pB}_{33} = 0$$

We get

$$L^B_{33\alpha\beta} N_\alpha g_\beta + N_\alpha L^B_{3333} D^B_{33} = \dot{\bar{\sigma}}_{33} - L^B_{33\alpha\beta} D_{\alpha\beta} \qquad \text{(B-5)}$$

Finally, equations (B-4) and (B-5) can be written in the matrix form:

$$\begin{bmatrix} \overline{R}_{11} & \overline{R}_{12} & \overline{R}_{13} \\ \overline{R}_{21} & \overline{R}_{22} & \overline{R}_{23} \\ \overline{R}_{31} & \overline{R}_{32} & \overline{R}_{33} \end{bmatrix} \begin{bmatrix} g_1 \\ g_2 \\ D^B_{33} \end{bmatrix} = \begin{bmatrix} \dot{f}_1 \\ \dot{f}_2 \\ \dot{f}_3 \end{bmatrix} \qquad (3.36)$$

with

$$\overline{R}_{\beta\kappa} = R_{\beta\kappa} - \frac{1}{2} N_\alpha N_\beta \sigma^B_{\alpha\kappa} + \left(\frac{1}{2} N_\alpha \sigma^B_{\alpha\gamma} N_\gamma \right) \delta_{\beta\kappa} + \frac{1}{2} N_\alpha N_\kappa \sigma^B_{\alpha\beta} - \frac{1}{2} \sigma^B_{\beta\kappa} - N_\alpha N_\kappa \sigma^B_{\alpha\beta}$$

And

$$R_{\beta\kappa} = N_\alpha \mathrm{L}^{B}_{\alpha\beta\kappa\gamma} N_\gamma$$

More specifically,

$$R_{11} = N_1^2 \mathrm{L}^{B}_{1111} + N_1 N_2 \mathrm{L}^{B}_{1121} + N_1 N_2 \mathrm{L}^{B}_{2111} + N_2^2 \mathrm{L}^{B}_{2121}$$

$$= N_1^2 \mathrm{L}^{B}_{1111} + 2N_1 N_2 \mathrm{L}^{B}_{1112} + N_2^2 \mathrm{L}^{B}_{1212}$$

$$R_{12} = N_l \mathrm{L}_{l1k2} N_k = N_1 \mathrm{L}^{B}_{11k2} N_k + N_2 \mathrm{L}^{B}_{21k2} N_k$$

$$= N_1^2 \mathrm{L}^{B}_{1112} + N_1 N_2 \mathrm{L}^{B}_{1122} + N_1 N_2 \mathrm{L}^{B}_{2112} + N_2^2 \mathrm{L}^{B}_{2122}$$

$$= N_1^2 \mathrm{L}^{B}_{1112} + N_1 N_2 (\mathrm{L}^{B}_{1122} + \mathrm{L}^{B}_{2112}) + N_2^2 \mathrm{L}^{B}_{2122}$$

$$R_{21} = N_l \mathrm{L}_{l2k1} N_k = N_1 \mathrm{L}^{B}_{12k1} N_k + N_2 \mathrm{L}^{B}_{22k1} N_k$$

$$= N_1^2 \mathrm{L}^{B}_{1211} + N_1 N_2 \mathrm{L}^{B}_{1221} + N_1 N_2 \mathrm{L}^{B}_{2211} + N_2^2 \mathrm{L}^{B}_{2221}$$

$$= N_1^2 \mathrm{L}^{B}_{1211} + N_1 N_2 (\mathrm{L}^{B}_{1221} + \mathrm{L}^{B}_{2211}) + N_2^2 \mathrm{L}^{B}_{2221}$$

$$R_{21} = R_{12}$$

$$R_{22} = N_l \mathrm{L}^{B}_{l2k2} N_k = N_1 \mathrm{L}^{B}_{12k2} N_k + N_2 \mathrm{L}^{B}_{22k2} N_k$$

$$= N_1^2 \mathrm{L}^{B}_{1212} + N_1 N_2 \mathrm{L}^{B}_{1222} + N_1 N_2 \mathrm{L}^{B}_{2212} + N_2^2 \mathrm{L}^{B}_{2222}$$

$$= N_1^2 \mathrm{L}^{B}_{1212} + 2N_1 N_2 \mathrm{L}^{B}_{1222} + N_2^2 \mathrm{L}^{B}_{2222}$$

$$\overline{R}_{11} = R_{11} - \cancel{\frac{1}{2} N_\alpha N_1 \sigma^{B}_{\alpha 1}} + \frac{1}{2}\eta + \cancel{\frac{1}{2} N_\alpha N_1 \sigma^{B}_{\alpha 1}} - \frac{1}{2}\sigma^{B}_{11} - N_1 N_\alpha \sigma^{B}_{\alpha 1}$$

$$= R_{11} - N_1^2 \sigma^{B}_{11} - N_2^2 \frac{\sigma^{B}_{11} - \sigma^{B}_{22}}{2}$$

$$= (\mathrm{L}^{B}_{1111} - \sigma^{B}_{11}) N_1^2 + (2\mathrm{L}_{1112}) N_1 N_2 + (\mathrm{L}^{B}_{1212} - \frac{\sigma^{B}_{11} - \sigma^{B}_{22}}{2}) N_2^2$$

$$\overline{R}_{12} = R_{12} - \frac{1}{2} N_\alpha N_1 \sigma^{B}_{\alpha 2} - \frac{1}{2}\sigma^{B}_{12} - \frac{1}{2} N_\alpha N_2 \sigma^{B}_{\alpha 1}$$

$$= R_{12} - \sigma_{12}^{B} - N_1 N_2 \frac{\sigma_{11}^{B} + \sigma_{22}^{B}}{2}$$

$$= R_{12} - N_1^2 \sigma_{12}^{B} - N_2^2 \sigma_{12}^{B} - N_1 N_2 \frac{\sigma_{11}^{B} + \sigma_{22}^{B}}{2}$$

$$= (\mathrm{L}_{1112}^{B} - \sigma_{12}^{B}) N_1^2 + [\mathrm{L}_{1122}^{B} + \mathrm{L}_{1212}^{B} - \frac{\sigma_{11}^{B} + \sigma_{22}^{B}}{2}] N_1 N_2 + (\mathrm{L}_{1222}^{B} - \sigma_{12}^{B}) N_2^2$$

$$\overline{R}_{21} = \overline{R}_{12}$$

$$\overline{R}_{22} = R_{22} - \frac{1}{2} N_\alpha N_2 \sigma_{\alpha 2}^{B} + \frac{1}{2} \eta - \frac{1}{2} \sigma_{22}^{B} - \frac{1}{2} N_\alpha N_2 \sigma_{\alpha 2}^{B}$$

$$= R_{22} - N_2^2 \sigma_{22}^{B} + N_1^2 \frac{\sigma_{11}^{B} - \sigma_{22}^{B}}{2}$$

$$= (\mathrm{L}_{1212}^{B} - \frac{\sigma_{11}^{B} - \sigma_{22}^{B}}{2}) N_1^2 + (2\,\mathrm{L}_{2212}) N_1 N_2 + (\mathrm{L}_{2222}^{B} - \sigma_{22}^{B}) N_2^2$$

$$\overline{R}_{13} = N_\alpha \mathrm{L}_{\alpha 133}^{B} = N_1 \mathrm{L}_{1133}^{B} + N_2 \mathrm{L}_{1233}^{B}$$

$$\overline{R}_{23} = N_\alpha \mathrm{L}_{\alpha 233}^{B} = N_1 \mathrm{L}_{1233}^{B} + N_2 \mathrm{L}_{2233}^{B}$$

$$\overline{R}_{31} = \overline{R}_{13}, \quad \overline{R}_{32} = \overline{R}_{23}$$

$$\overline{R}_{33} = \mathrm{L}_{3333}^{B}$$

The right hand side of (3.36) is

$$\dot{f}_\beta = \dot{W}_\beta + \dot{X}_\beta + \dot{Y}_\beta + \dot{Z}_\beta \quad (\beta = 1,2)$$

$$\dot{f}_3 = \dot{\bar{\sigma}}_{33}^{B} - (\mathrm{L}_{3311}^{B} + \rho\, \mathrm{L}_{3322}^{B}) D_{11}$$

with

$$\dot{W}_\beta = N_\alpha (\xi\, \mathrm{L}_{\alpha\beta\kappa\gamma} - \mathrm{L}_{\alpha\beta\kappa\gamma}^{B}) D_{\kappa\gamma}$$

$$\dot{X}_\beta = N_\alpha (\xi \dot{\bar{\sigma}}_{\alpha\beta} - \dot{\bar{\sigma}}_{\alpha\beta}^{B})$$

$$\dot{Y}_{\beta} = \left(\frac{N_{\alpha}}{dt} + \dot{N}_{\alpha} - N_{\alpha} D_{\kappa\kappa} \right) \left(\xi \sigma_{\alpha\beta} - \sigma^{B}_{\alpha\beta} \right)$$

$$\dot{Z}_{\beta} = \xi D_{33} N_{\alpha} \mathrm{L}_{\alpha\beta 33}$$

APPENDIX C

Flow Chart for Calculating One Point (Strain or Stress Ratio) in Forming Limit Diagram (FLD)